공학박사학위논문

산소발생기를 활용한 고분자전해질막 연료전지시스템의 성능 향상에 관한 연구

A study on the performance improvement of PEM fuel cell system using an oxygen concentrator

2023 년 8 월

서울대학교 대학원

기계공학부

이 유 일

산소발생기를 활용한 고분자전해질막 연료전지시스템의 성능 향상에 관한 연구

A study on the performance improvement of PEM fuel cell system using an oxygen concentrator

지도교수 김 민 수

이 논문을 공학박사 학위논문으로 제출함

2023 년 4 월

서울대학교 대학원

기계공학부

이 유 일

이유일의 공학박사 학위논문을 인준함

2023 년 6 월

위 원 장 : _____ (인)

부위원장 : _____ (인)

위   원 : _____ (인)

위   원 : _____ (인)

위   원 : _____ (인)

A Study on the Performance Improvement of the PEM fuel cell system using an oxygen concentrator

산소발생기를 활용한 고분자전해질막
연료전지시스템의 성능 향상에 관한 연구

August 2023

Graduate School of Mechanical Engineering
Seoul National University

Yoo Il Lee

Abstract

A Study on the
Performance Improvement of the
PEM fuel cell system
using an oxygen concentrator

Yoo IL Lee

Department of Mechanical Engineering

The Graduate School

Seoul National University

This study investigates the performance enhancement of proton exchange membrane (PEM) fuel cells by implementing an oxygen concentrator that uses pressure swing adsorption (PSA) and anode gradient flow fields. The oxygen enrichment strategy proactively addresses the inherently slow kinetics of oxygen reduction reaction and the challenges related to mass transport. Concurrently, the strategic implementation of an anode gradient flow field ameliorates water management within the membrane, thereby enhancing overall fuel cell performance.

The study begins by developing and evaluating a PSA oxygen concentrator,

assessed under various operating conditions. A PEM fuel cell comprised of five parallel serpentine channel bipolar plates is subjected to a range of oxygen concentrations to gauge its compatibility with the concentrator. An oxygen concentrator operating at 2 bar pressure and delivering 40% oxygen purity improves net power by 7.5W at peak power, a 42% compared to the air baseline.

Mathematic models for the oxygen concentrator and the PEM fuel cell are developed using the Matlab® platform. The oxygen concentrator model simulates the pressure swing adsorption cycle and provides performance metrics such as oxygen purity and recovery. The PEM fuel cell model accommodates different gas compositions, enabling integration with the concentrator's output. The synergy between these models enables predictive simulation of PEM fuel cell performance, offering insights into optimal system configuration, operating parameters, scalability, and customization for real-world applications.

In addition, this study also examines the influence of anode gradient flow fields on PEM fuel cell performance. Oxygen enrichment increases the operating current, intensifying the water imbalance in the membrane, primarily attributed to increased electro-osmotic drag. An analysis of various anode gradient flow fields proposes potential solutions to ameliorate the heterogeneous gas composition along the channel and boost membrane hydration. Metal foam flow fields, characterized by increasing porosity and thickness from gas inlet to outlet, enhance cell performance by improving membrane humidification on the anode side. This research emphasizes the often-overlooked optimal design of the anode side.

In conclusion, this study demonstrates that combining PSA oxygen concentrators with PEM fuel cells can increase net power, despite higher

maintenance and capital costs. The use of anode gradient metal foams improves membrane hydration. The findings have significant implications for developing more efficient and cost-effective PEM fuel cell systems in various applications, from transportation to stationary power generation.

Contents

List of Figures

ix

List of Tables

Chapter 1. Introduction

1.1. Background

Climate change presents a considerable threat to both humans and wildlife as it is likely to increase the frequency and severity of extreme weather events such as drought, storms, and heat waves. Recognizing climate change as a global emergency [1], the Glasgow Climate Pact at the 2021 United Nations Climate Change Conference (COP26) called upon countries to revise and strengthen their previous 2030 emission targets. This emphasis on reducing emissions has created a favorable environment for developing and adopting eco-friendly technologies.

The transportation sector remains a significant source of air pollution and greenhouse gas emissions. In response, governments have established and continually reinforced legislation and regulations to reduce automotive vehicle emissions. Consequently, automotive manufacturers have sought to develop and refine advanced combustion engine technologies to comply with current and future regulations. Meeting fuel and emission standards with conventional engines alone have become increasingly complex, if possible, leading to the development of hybrid vehicles and replacing energy conversion devices with batteries or fuel cells in pursuit of zero-emission vehicles.

The sale of electric vehicles (EVs) is prospering, with approximately 10% of total global car sales in 2021 being electric. This increase in EV sales has led to the number of electric vehicles on the road tripling compared to 2018 [2].

Government incentives have supported the transition towards electric vehicles, including fuel cell electric vehicles (FCEVs). Tax reductions and subsidies have been implemented to make zero-emission vehicles more financially attractive to consumers [2].

Furthermore, government initiatives and public-private partnerships have been instrumental in driving the implementation of EV charging stations, including FCEVs [3]. Transportation plans from state and local governments include strategically establishing EV charging stations and collaborating with private companies. Despite the advancements made, establishing a more comprehensive network of charging stations remains critical for widespread EVs. The success of this endeavor hinges on the collaboration between federal, state, and local governments, as well as private industry, to optimize the utilization of allocated funds and hence the charging network.

Currently, the electric vehicle market is booming, driven mainly by battery electric vehicles. However, FCEVs, which utilize polymer electrolyte membrane fuel cells (PEMFCs), offer an alternative zero-emission technology. Operating at PEM fuel cells operate at low temperatures (~80°C), and produce water and heat as byproducts. Hydrogen, a universally abundant resource, can be quickly produced without any geographical restriction, and it can be an eco-friendly and self-sustainable energy source when obtained using renewable energy.

Despite FCEVs' advantages in faster refueling times (ca. 3–5 min) and longer driving ranges [4], BEVs remain more popular due to their low capital costs and more extensive infrastructure. **Table 1** presents a comparative analysis of the key characteristics of various electric vehicle types, including battery electric

vehicles (BEVs), hybrid electric vehicles (HEVs), and fuel cell electric vehicles (FCEVs). This table highlights the propulsion systems, energy systems, infrastructure requirements, and notable characteristics of each vehicle type, as well as the major challenges associated with their adoption and implementation. Enhancing the market competitiveness of FCEVs relies on the cost reduction, particularly the noble platinum materials for the catalysts. To achieve this, research endeavors have focused on synthesis of non—precious metal catalysts as substitute [5] or reduced platinum loading catalyst [6]. Moreover, efforts have been directed towards improving the individual cell performance, reducing the required number of cells in the stack and decreasing material costs. Continuous advancements in fuel cell technologies are bringing the commercialization of fuel cells one step closer.

Transitioning to the subsequent chapter, this study delves into the rudimentary aspects of PEM fuel cells, including their core components, operating principles, and cell overvoltage phenomena. A thorough comprehension of these fundamentals facilitates the identification of operational impediments and potential pathways for performance augmentation. A significant challenge encountered within the system is the concentration loss at the cathode, predominantly attributable to the low oxygen concentration in the air, mass transport complications arising from water flooding, and inherent material resistance. In subsequent sections of this study, an innovative approach to mitigate these losses is explored – the enrichment of oxygen via an oxygen concentrator that supplies the PEM fuel cell, thus diminishing both cathode concentration loss and activation loss. Concurrently, anode bipolar plates are subjected to gradient design alterations, an approach anticipated to curtail ohmic resistance by improving membrane hydration levels.

This exploration illuminates the latent potential of PEM fuel cells when oxygen concentration is optimized, demonstrating its applicability for FCEVs in the transportation sector and for stationary power generation within the industrial sector.

Table 1 Major characteristics of BEVs, HEVs, and FCEVs, modified from Chan et al. [7]

Types of EVs	BEVs	Hybrid EVs	FCEVs
Propulsion	• Electric motor drives	• Electric motor drives • Internal combustion engine	• Electric motor drives
Energy system	• Battery • Ultracapacitor	• Battery • Ultracapacitor	• Fuel cells • Battery for starting
Infrastructure	• Electric grid charging facilities	• Gasoline stations • Electric grid charging facilities (for plug-in hybrid)	• Hydrogen charging stations
Characteristics	• Zero-emission • High energy efficiency • Independence on crude oils • Relatively short range • High initial cost	• Very low emission • Higher fuel economy as compared with ICE vehicles • Long drive range • Higher cost as compared with ICE vehicles	• Zero-emission • High energy efficiency • Independence on crude oil • Satisfied driving range • High cost
Major issues	• Battery management • Charging facilities • Cost	• Multiple energy sources control, optimization, and management • Battery sizing and management	• Expensive fuel cell • Durability • Hydrogen infrastructure

1.2. Polymer electrolyte membrane fuel cells

1.2.1. Basics of PEMFC

PEMFCs represent a category of fuel cells characterized by the utilization of a polymer-based membrane as the electrolyte medium. Nafion®, a specific perfluorosulfonic acid polymer, is the predominant choice for PEM membranes due to its exceptional proton conductivity. The solid-state nature of the PEM membrane provides a stable and efficient platform for electrochemical reactions, contrasting with liquid electrolyte systems that are prone to leakage and often exhibit diminished efficiency. A notable advantage of PEMFCs is their capacity to operate at low temperatures (~80°C) while delivering high power density. As a result, PEMFCs have garnered recognition as promising alternative portable power sources in the automotive and stationary sectors.

The essential principle underlying fuel cells stem from the reverse reaction of water electrolysis, as exemplified by the following equation:

$$H_2 + \frac{1}{2}O_2 \rightarrow H_2O \tag{1.1}$$

Membranes play a pivotal role in efficiently extracting electrical energy from this electrochemical reaction by facilitating selective proton transport across the membrane while impeding electron flow. This controlled diversion of protons and electrons enables the establishment of an external load circuit, as depicted in **Figure 1(a)**. At the anode, hydrogen oxidation occurs while protons traverse the membrane, and electrons follow the external path, ultimately reacting with oxygen at the cathode. This orchestrated movement of electrons permits harnessing the electrical energy generated by the electrochemical reaction.

The cell voltage exhibits a high degree of sensitivity to the catalyst's

condition. The Nernst and Butler-Volmer equations highlight the critical role played by the reactant gas concentration at the catalyst surface, which significantly impacts the underlying electrochemical reactions. To ensure a high concentration of reactant gas, it is essential for the cell to effectively transport the reactant gas and efficiently remove any excess liquid water. Notably, the emphasis on optimizing reactant transport is primarily on the cathode due to several vital factors. Firstly, the cathode catalyst produces water as a byproduct, which hampers gas transport by obstructing the pores and limiting the movement of reactant gases. Secondly, the reactant gas for the cathode is oxygen, which is supplied through air that contains only 21% oxygen. Consequently, the availability of oxygen at the cathode is inherently limited. Lastly, the oxygen reduction reaction rate occurring at the cathode is notably slower than that of hydrogen oxidation reactions. This imbalance in reaction rates necessitates special attention to improving oxygen delivery to the catalyst to enhance overall cell performance. Extensive research efforts have thus been dedicated to addressing these challenges and optimizing oxygen transport to the cathode catalyst.

Figure 1(b) illustrates the path of oxygen molecules reaching the cathode catalyst from the flow fields, highlighting the distinct transport mechanisms involved in oxygen transport across the flow fields, gas diffusion layer (GDL), microporous layer (MPL), catalyst layer, and agglomerate. The primary mechanism of oxygen transport varies across each layer due to differences in their physical properties.

Due to the convective force, the reactant gas is transported rapidly along the flow fields. The momentum of the gas facilitates the product water expulsion from the outlet. As the reactant gas enters the GDL substrate, the mode of transport transitions from convection to diffusion. The average pore diameter of the substrates

is significantly larger than the mean free path of gas molecules, making molecular diffusion the dominant driving force for transport.

While traversing the GDL substrate, oxygen encounters smaller pores within the MPL and catalyst. As the pore diameter becomes the order of the mean free path of gas molecules, collisions between molecules and the diffusion medium become more frequent, resulting in Knudsen diffusion. Consequently, the diffusion process within the MPL and catalyst layer involves a combination of molecular and Knudsen diffusion.

Upon reaching the catalyst agglomerate, a portion of oxygen must dissolve to permeate the ionomer that partially covers the agglomerate. This process exemplifies the oxygen transport mechanism within the catalyst layer. The foregoing provides a concise overview of the oxygen transport resistance encountered by each component. The porous GDL, MPL, and catalyst layer enable several vital functions. These components facilitate efficient gas transport through the pores, remove water through capillary pressure gradients, and contribute to the system's overall functionality. Additionally, they play a crucial role in supporting heat transfer and ensuring effective electrical conductivity throughout the fuel cell.

Two strategies have been considered to boost oxygen transport. The first method focuses on improving each component's transport resistance, including the flow fields, GDL, MPL, and the catalyst layer, by improving their design and material properties. The second method entails elevating the oxygen concentration of the feed gas, thereby facilitating a more excellent supply of oxygen to the catalyst layer.
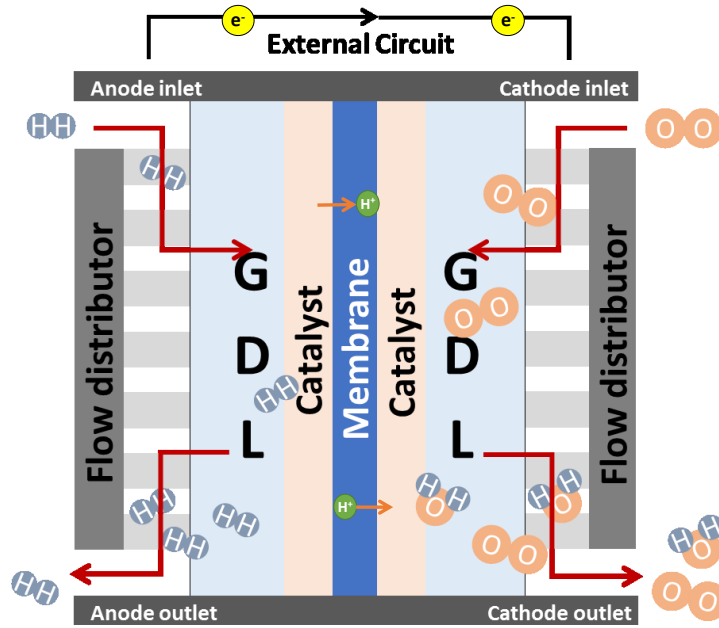
(a)
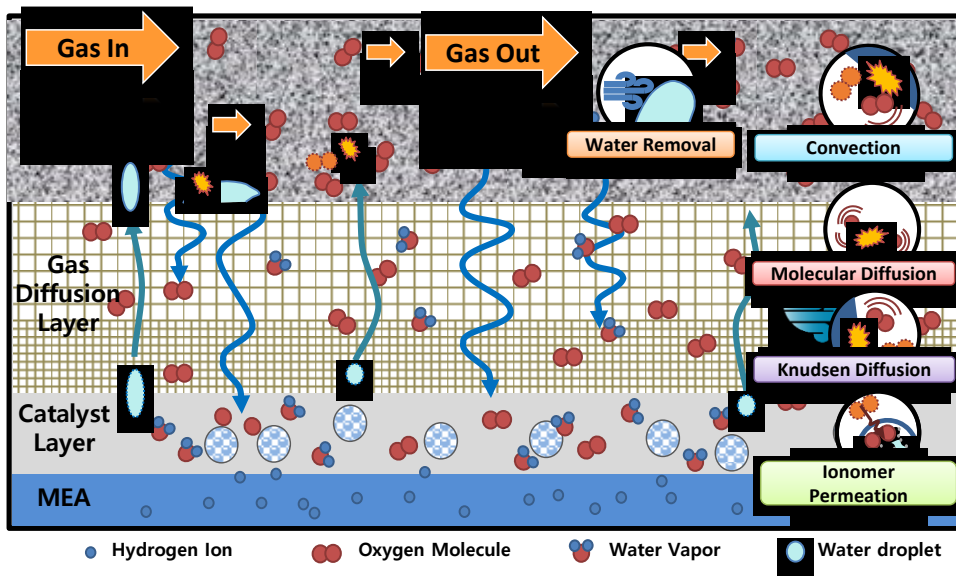
(b)

Figure 1   Schematics diagram of (a) PEM fuel cell [8] and (b) oxygen transports in

cathodes

1.2.2. Oxygen enrichment for enhanced performance

The strategy of oxygen enrichment ostensibly presents itself as a straightforward way to augment the performance of PEM fuel cells. Oxygen enrichment, in principle, reduces overvoltage primarily by amplifying the exchange current densities attributable to increased oxygen concentrations. However, it is crucial to note that oxygen enrichment research concerning PEM fuel cell performance is relatively nascent and warrants more comprehensive exploration.

In a recent investigation, Kumar and Subramanian [9] endeavored to clarify the influence of oxygen enrichment on PEMFC. It is important to acknowledge several significant limitations of their study, including an exceptionally restrictive current range of up to 0.6 A and a lower operating temperature of 55℃. They postulated an optimal oxygen concentration threshold – oxygen-enriched air – beyond which PEM fuel cell efficiency purportedly declines due to increased water production. Furthermore, they reported a discernible drop in PEM fuel cell performance within the 25% to 35% oxygen concentration range. However, these claims warrant cautious interpretation as they appear to contradict experimental data presented in subsequent chapters of this study. Given a specific current, the amount of water the electrochemical reaction generates remains invariant, regardless of the oxygen concentration. Consequently, there is no immediately apparent rationale for the alleged performance decline with increased oxygen concentration.

This discrepancy underscores the necessity for comprehensive research on PEM fuel cells operating under a range of oxygen concentrations, particularly when developing PEM fuel cells equipped with an oxygen concentrator, as undertaken in this study. Deepening our understanding in this area yields invaluable insights,

enabling the determination of optimal conditions for oxygen enrichment for PEM fuel cells with oxygen concentrators and addressing potential challenges linked to the practical implementation of this strategy in real-world fuel cell applications. The accumulation of such insights can significantly advance the practical application of oxygen enrichment strategies for enhancing PEM fuel cell performance.

1.3. Pressure swing adsorption for oxygen production

1.3.1. Introduction

Pressure swing adsorption (PSA) is a well-established cyclic process that selectively separates and purifies gas mixtures. The distinction in adsorption kinetics and adsorbent capacity is tactically utilized to selectively eliminate one or more constituents from a specific gas mixture. This process leverages the differential adsorption properties of the components within the mixture, thereby facilitating targeted separation and purification. The first patent for a PSA process was granted to Charles Skarstrom in the United States in 1960 [10]. Since then, this technology has been broadly accepted across many industrial applications, including hydrogen production, natural gas processing, air separation, and biogas upgrading.

PSA offers fast response start-up, high-purity output, and lower energy consumption, which collectively render it an attractive solution for small to medium-sized applications. The design of the PSA permits straightforward replacement or regeneration of the adsorbent material, contributing to long-term, economically sustainable operation.

In recent decades, the application of PSA for oxygen production has experienced an appreciable increase, particularly within the sectors such as healthcare, military and aerospace, semiconductor manufacturing, and metal welding and cutting processes [11]–[14]. Notably, the onset of the COVID-19 pandemic has created an unprecedented demand for Medical Oxygen Concentrators (MOCs), thereby further catalyzing the focus on oxygen production via PSA[15].

The synthesis of adsorbents with higher selectivity, including LiX-, LSX-, LiLSX-type, and silver-exchange zeolites in the 1990s, marked a significant

milestone in enhancing the efficiency of the oxygen separation process [16], [17]. This pivotal development laid the groundwork for integrating oxygen concentrators with PEM fuel cells without compromising the net power output.

1.3.2. Adsorption Phenomena

Adsorption is defined as an exothermic process wherein gas or liquid molecules adhere to the surface of a solid or liquid medium, thereby creating a thin layer, as depicted in **Figure 2**. It is of critical importance to differentiate between adsorption, which is a surface phenomenon, and absorption, a process involving bulk phenomena. A comparison of key differences is listed in **Table 2**. The capacity for adsorbate adherence on an adsorbent is contingent on the physical and chemical attributes of the adsorbent, the adsorbate, and the adsorption conditions, such as temperature and pressure.

PSA exploits differences in the adsorption rate and capacity of various gases under varying pressure conditions. The adsorption process is performed under high pressure until the adsorbent reaches its maximum saturation level. Then, the pressure is lowered, prompting desorption of the adsorbed gases and regeneration of the adsorbent. This cyclic variation in pressure ensures continuous operation of the gas separation process.

PSA exploits differences in the adsorption rate and capacity of various gases under varying pressure conditions. The adsorption process is performed under high pressure until the adsorbent reaches its maximum saturation level. Then, the pressure is lowered, prompting desorption of the adsorbed gases and regeneration of the

adsorbent. This cyclic variation in pressure ensures continuous operation of the gas separation process.

Various adsorbent materials, such as zeolite, activated carbon, silica gel, and molecular sieves, are employed for PSA. The selection of appropriate adsorbent material hinges on many factors, including the composition of the gas mixture intended for separation, operating conditions, and desired purity level of the separated gas output.

Among the adsorbents used for oxygen separation, molecular sieves like 5A, 13X, and LiLSX are predominant. Despite their shared capability to separate oxygen from nitrogen, these adsorbent materials exhibit salient differences. One of the primary distinguishing factors is the dimension of pore size, as shown in Table 3. 13X and LiLSX, each with an approximate pore size of 9 angstroms, exceed the effective pore opening of 5A, which is about 5 angstroms. This larger pore structure equips 13X and LiLSX with enhanced capability to adsorb and remove larger molecules, including carbon dioxide and water vapor. Furthermore, the capacity to adsorb specific gas molecules varies among these adsorbents. LiLSX demonstrates a higher nitrogen adsorption capacity than 5A, 13X. The adsorption efficiency could be further improved using silver-exchanged zeolite, albeit with a cost increase.

(a)   (b)
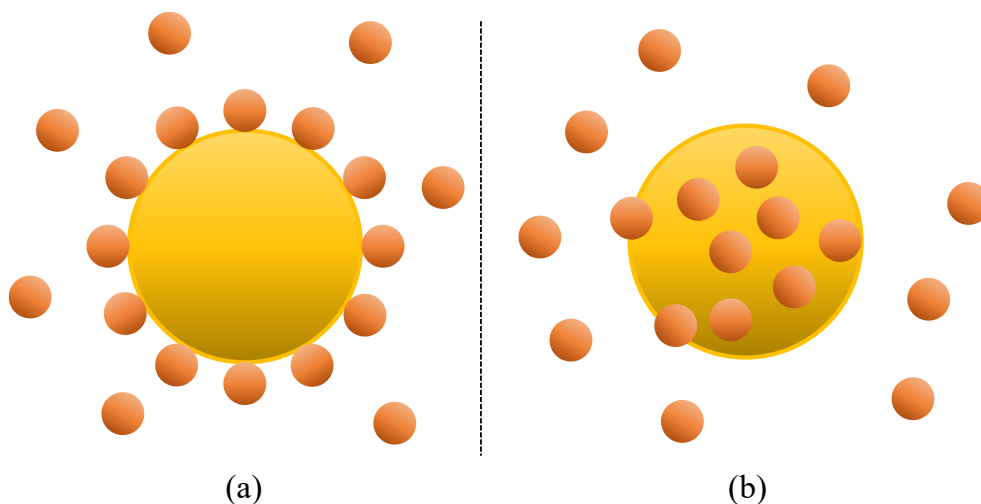
Figure 2 Illustration of (a) adsorption, (b) absorption

Table 2 Comparison between adsorption and absorption

	Absorption	**Adsorption**
Definition	Absorption is a bulk phenomenon when molecular species are fully integrated into one another.	Adsorption is a surface phenomenon when molecular species adhere to the surface of a solid
Rate of reaction	Generally uniform, as it is controlled by diffusion	Slows as the available surface area is covered
Reversibility	Not easily reversible	Readily reversible
Heat exchange	Endothermic process	Exothermic process
Temperature	Not affected	Favors low temperature

Table 3 Comparison of various zeolites for oxygen production

Adsorbent	O₂ Production Efficiency	Cost	Pore Size (Å)	Cation
Zeolite 5A	Good	Moderate	~ 4.7 [18]	Ca2+, Na+
Zeolite 13X	Better	High	7 ~ 9 [19]	Na+
Li-LSX Zeolite	Excellent	Higher	~ 8 [18]	Li+
Silver-exchanged Zeolite	Very Excellent	Very High	Similar to parent zeolite, but altered by Ag ions	Ag+

1.3.3. PSA cycles

The PSA system typically follows a sequence of four principal steps and two pressure equalization steps. These steps include pressurization, adsorption, depressurizing pressure equalization, blowdown, purge, and pressurizing pressure equalization. Including pressure equalization steps aims to conserve energy during pressurization and increase separative work.

The PSA system commonly incorporates two or more identical vessels filled with adsorbents to achieve a continuous product gas supply. These vessels, managed by valves, alternate between the adsorption and desorption cycle, ensuring an uninterrupted product gas flow. **Figure 3** depicts a dual-vessel configuration, visually representing the individual steps of the PSA cycle and demonstrating how one vessel engages in the adsorption process while the other undergoes regeneration.

Several configurations of PSA systems exist, including PSA, vacuum swing adsorption (VSA), rapid pressure swing adsorption (RPSA), and pressure vacuum swing adsorption (PVSA). Each configuration defines specific techniques and operational characteristics for efficiently separating gases within the PSA process. The two-bed PSA cycle is recognized for its simplicity and widespread use. The high pressure of the product stream produced by this process meets the needs of various industrial applications. The VSA cycle bears similarities to the PSA cycle but introduces a vacuum pump for bed regeneration. This modification grants VSA certain benefits over PSA, such as reduced energy consumption and lower capital cost. These advantages stem from its operation at lower pressures and the avoidance of high-pressure compressors. However, VSA's scalability for larger gas flow rates or complex gas mixtures may be compromised, and the choice of adsorbent can be

restricted due to the vacuum operation.

The RPSA is a variant of the PSA cycle optimized for high production rates and swift cycle times. The cycle involves two steps: pressurizing and depressurizing. The accelerated cycling time substantially shrinks the adsorbent size, but this reduction entails a compromise in recovery rate, leading to increased overall power consumption for a specific production flow rate [20]. Furthermore, it may adversely affect the quality of the resultant gas. Pressure-Vacuum Swing Adsorption (PVSA) integrates elements of both PSA and VSA cycles. This hybrid approach yields high separation efficiency and reduced energy consumption, albeit at a higher capital cost.
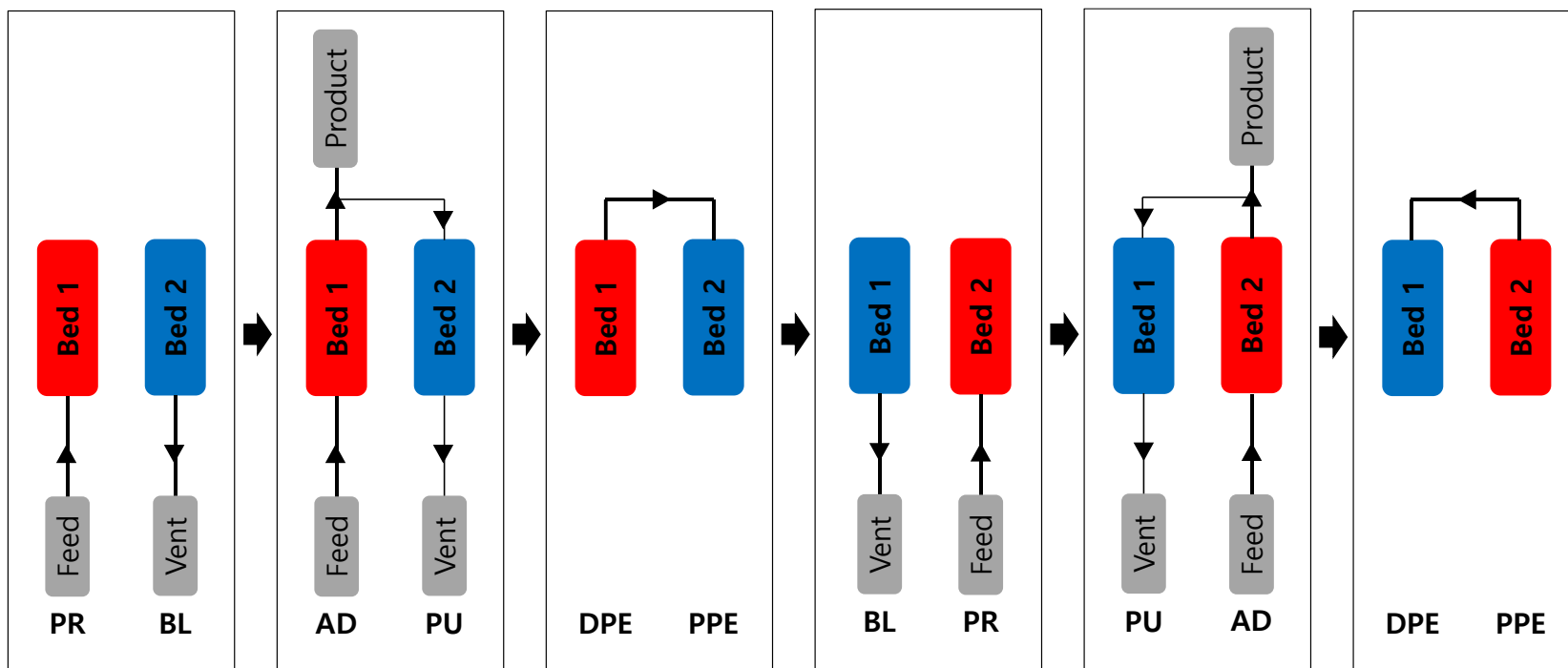
※ PR: Pressurization,　AD: Adsorption,　DPE: Depressurizing pressure equalization,　BL: Blowdown,　PU: Purge,　PPE: Pressurizing pressure equalization

Figure 3 Two-bed pressure swing adsorption cycles

1.4. Objectives of the study

The main objective of this study is to investigate the potential for performance enhancement of PEMFCs by applying PSA oxygen concentrators. A PSA oxygen concentrator leverages ambient air to generate an oxygen-enriched stream, which augments its power output when supplied to the PEM fuel cells.

Notably, the operation of a PSA oxygen concentrator necessitates additional energy, thereby increasing the power consumption of the balance-of-plant system. An integrated assessment of both components – the PEMFC and the oxygen concentrator – is requisite to ensure a net positive power output.

Firstly, this study thoroughly investigates the impact of varying oxygen concentrations on the performance of PEMFCs. Most extant studies have centered on PEM fuel cells operating either under atmospheric air or pure oxygen. While the benefits of pure oxygen operation vis-à-vis air operation are well established, the ramification of different oxygen concentrations on performance remains underexplored. This aspect warrants a more profound examination, particularly given this study's emphasis on oxygen-enriched operation in PEM fuel cell systems.

Secondly, the research involves constructing and evaluating small-scale PSA oxygen concentrators under diverse operations. Specifically, the internal pressure of the adsorbent bed and cycle timings will be varied to observe the resultant effects on product purity and flow rate. The aim is to pinpoint the optimal cycle timing for each pressure point and determine the most favorable PEM fuel cell integration operating conditions. This optimization is focused on maximizing the net power output of the PSA-PEM integrated system.

Thirdly, mathematical models for PSA and PEM fuel cells will be

developed. The PSA model will aid in calculating net power, product gas purity, and flow rate and assist in determining optimal operating parameters for our system. PEM fuel cell model will allow for the simulation of fuel cell performance under varying oxygen concentrations in the feed gas.

Additionally, the influence of anode gradient flow fields on PEMFC will be explored. Oxygen enrichment increases the operating current, exacerbating the membrane's water imbalance due to the intensification of electro-osmotic drag. Various anode gradient flow fields will be analyzed to identify potential solutions for improved membrane hydration.

In conclusion, this study aims to demonstrate that integrating PSA oxygen concentrators with PEM fuel cells can lead to a net power increase, despite higher maintenance and capital costs. The findings could potentially inform the development of more efficient and cost-effective PEMFC systems for various applications, including transportation and stationary power generation.

Chapter 2. Effect of Oxygen Concentration on PEM Fuel Cells

2.1. Introduction

Conventional PEM fuel cell systems are typically fed with hydrogen and ambient air. While using pure oxygen can augment the performance of PEM fuel cells, it introduces logistical challenges, including the requirement for additional storage space and regular replenishment of the oxygen supply. These complexities often confine the use of pure oxygen to specialized applications such as submarines or spacecraft, where the unique operational environment justifies the logistical complexity [21]–[24].

Nevertheless, the continual advancement in adsorbent materials has opened up new possibilities. Specifically, these materials can facilitate oxygen extraction from the air, leading to an oxygen concentration of up to 95%. Despite this potential, it is worth noting that, to our knowledge, no PEM fuel cell system currently employs oxygen-enriched air as the cathode feed gas.

Our work seeks to bridge this gap by integrating an oxygen concentrator into the PEM fuel cell system. To achieve this aim, it becomes imperative to understand how varying oxygen concentrations affect PEM fuel cell performance. Therefore, this chapter is devoted to exploring the impact of oxygen concentration on several key performance indicators of PEM fuel cells, including the performance curve and electrochemical impedance spectroscopy (EIS) results.

2.2. Experimental Setup

2.2.1. PEM Fuel cell with parallel serpentine channels

Our study employed a fuel cell with parallel serpentine channels due to their favorable gas distribution and moderate capability to remove liquid water from the channels through pressure drop. This configuration comprised five identical channels, each having a width of 1mm. Land, the areas between the channels, had a width of 1.04 mm. The depth of the anode and cathode channels was 0.4 mm and 0.8mm, respectively. The cathode channel is deliberately deeper to promote liquid water removal, a critical factor in operating at a high current density.

Given the anticipated enhancement in fuel cell performance under higher oxygen concentrations, we felt it necessary to adapt our experimental setup to fully capture its behavior. Traditional active area dimensions (50 mm by 50mm) might not accurately reflect the entire performance range under various oxygen-enriched scenarios. As a result, we chose to modify the active area to 40 mm by 50 mm, achieved by employing a gasket to restrict a portion of the MEA, as illustrated in **Figure 4**.

We prepared a 315-micron thick GDL with MPL (39BB, SGL Carbon, Germany) implemented on the MEA (VFP-A2B025-G00, Vinatech, South Korea). A 200-micron thick PTFE gasket was also applied to compress the GDL by 25% to enhance electrical contact. This preparation provides a comprehensive foundation for observing and understanding the behavior of the PEMFC under various oxygen concentrations.
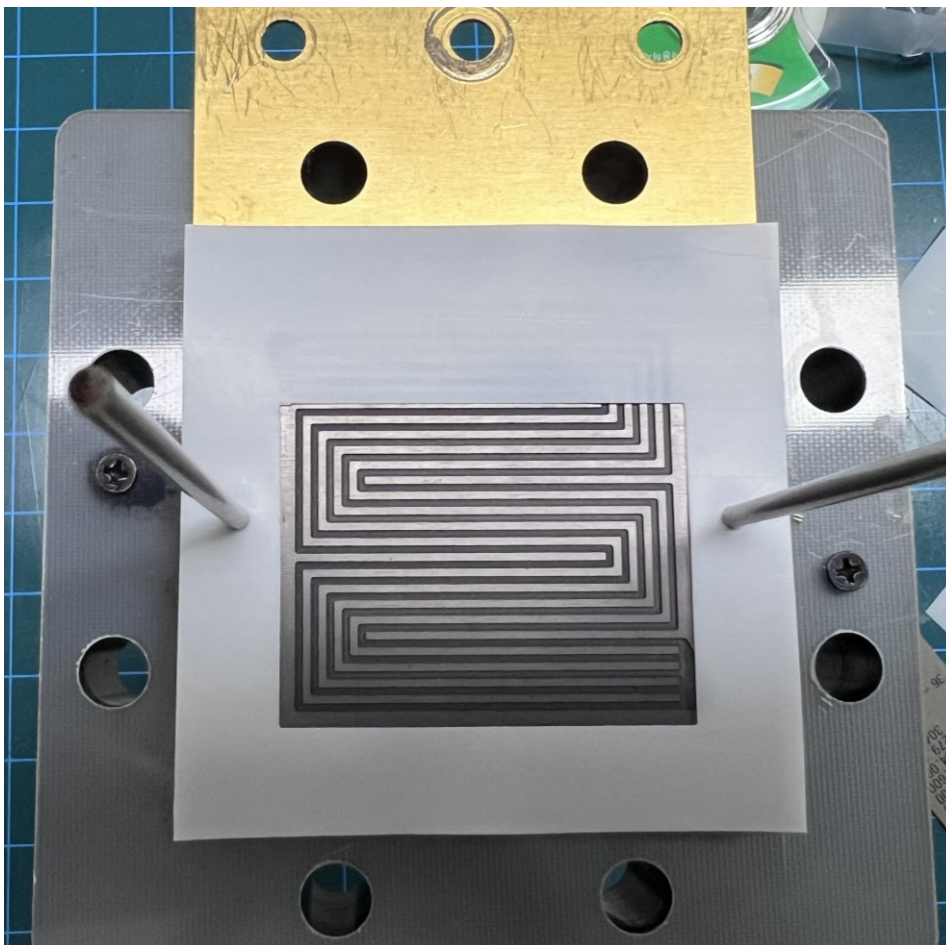
Figure 4 Strategic modification of active area through gasket configuration

2.2.2. Experimental conditions for oxygen concentration tests

In this study, we examined the impact of oxygen concentration on PEMFCs under various operating parameters, including pressure and stoichiometric ratio, through the current-voltage (IV) curves and EIS measurements. The specific parameters for our experimentation are detailed in **Table 4.**

The operating temperature was maintained at 65°C, and the reactant gases' relative humidity (RH) was modulated to be 100%. The stoichiometric ratio of anode and cathode was set to 1.5 and 2.0, respectively, except for stoichiometric ratio tests. As the oxygen concentration in the feed increase, we anticipate a corresponding increase in oxygen concentration at the catalyst following the electrochemical reactions due to the reduced presence of inert nitrogen gas. A lower stoichiometric ratio could thus still yield a similar residual oxygen concentration. However, a smaller stoichiometric ratio also corresponds to a slower flow rate, which can impact water removal from the channels. This suggests an optimal stoichiometric ratio exists, determining which forms an objective of our experiments.

In the IV curve tests, we held a constant current level for 120 seconds at each step, disregarding the initial 40 seconds' data to account for the voltage undershoot area and allow adequate time for species transport and stabilization of membrane hydration [25], [26]. We then utilized the voltage data collected over the next 60 seconds, sampled at 100 Hz, to calculate the average and corresponding standard deviation for each current step. We ensured the cell voltage did not fall below 0.3 to avoid irreversible cell degradation.

Impedance measurements, taken at 1.5 and 3.0 A/cm^2, covered a frequency range of 0.5 to 10 kHz, with the alternating current set at 5.0% of the load current.

Through this extensive and meticulously designed experiment, our goal is to deepen the understanding of how oxygen concentration impacts PEM fuel cell performance and to pave the way for optimal integration of oxygen concentrators into these systems.

Table 4 Experimental conditions for oxygen variation test

Parameter	Value
Operating temperature (°C)	65
Relative humidity of feed gas (%)	100
Operating pressure (atm)	1 (for most cases), 1.5 and 2.0 (for 20% O_2 case only)
Oxygen Concentration (%)	20, 21(Air), 30, 40, 50, 60, 80, 100
Stoichiometric ratio	1.5 for the anode, 1.25 1.5 1.75 2.0 for the cathode
Current (A/cm^2)	Stepwise increase: 0, 0.05, 0.1, 0.25, 0.375, … up to 4 (increments by 0.125)
Voltage measuring frequency (Hz)	100
Measuring period for each step (s)	120
EIS measuring frequency (Hz)	0.5 – 10,000
EIS measuring AC (%)	5.0
EIS moving average	16

2.2.3. Experimental apparatus

For the purpose of this study, a testing station, depicted in **Figure 5**, was constructed to facilitate our fuel cell experiments**.** This station incorporates four mass flow controllers (MC-Series, Alicat Scientific, USA), which control the mass flow rates of hydrogen, air, nitrogen, and oxygen gas. The simultaneous utilization of nitrogen and oxygen gas mass flow controllers enables the creation of a mixture of gas with varied oxygen concentrations, thereby providing flexibility in examining the fuel cell performance under different oxygen concentrations.

To ensure adequate reactant gas humidification, we integrated membrane humidifiers (Humidity bottles, Fuel Cell technologies Inc., USA) into the testing station. Electric heaters were applied to the gas lines to maintain the required temperature and prevent water condensation, ensuring constant humidified conditions. To maintain the desired cell temperature, we employed cartridge heaters coupled with a fan for heat dispersion.

This setup also includes electronic back pressure regulators (PC-Series, Alicat Scientific, USA) downstream of the water trap, facilitating precise control over cell pressure for pressurization tests. In our commitment to precise voltage recording at high frequencies, we incorporated an electronic load (PLZ664WA, Kikusui Electronics, Japan) and a data acquisition device (DAQ) (USB-6211, National Instruments, USA). These devices allowed for accurate application of current to the fuel cell and capturing of voltage data, respectively. We employed a fuel cell impedance meter (KFM2150, Kikusui Electronics, Japan) for detailed impedance measurements.
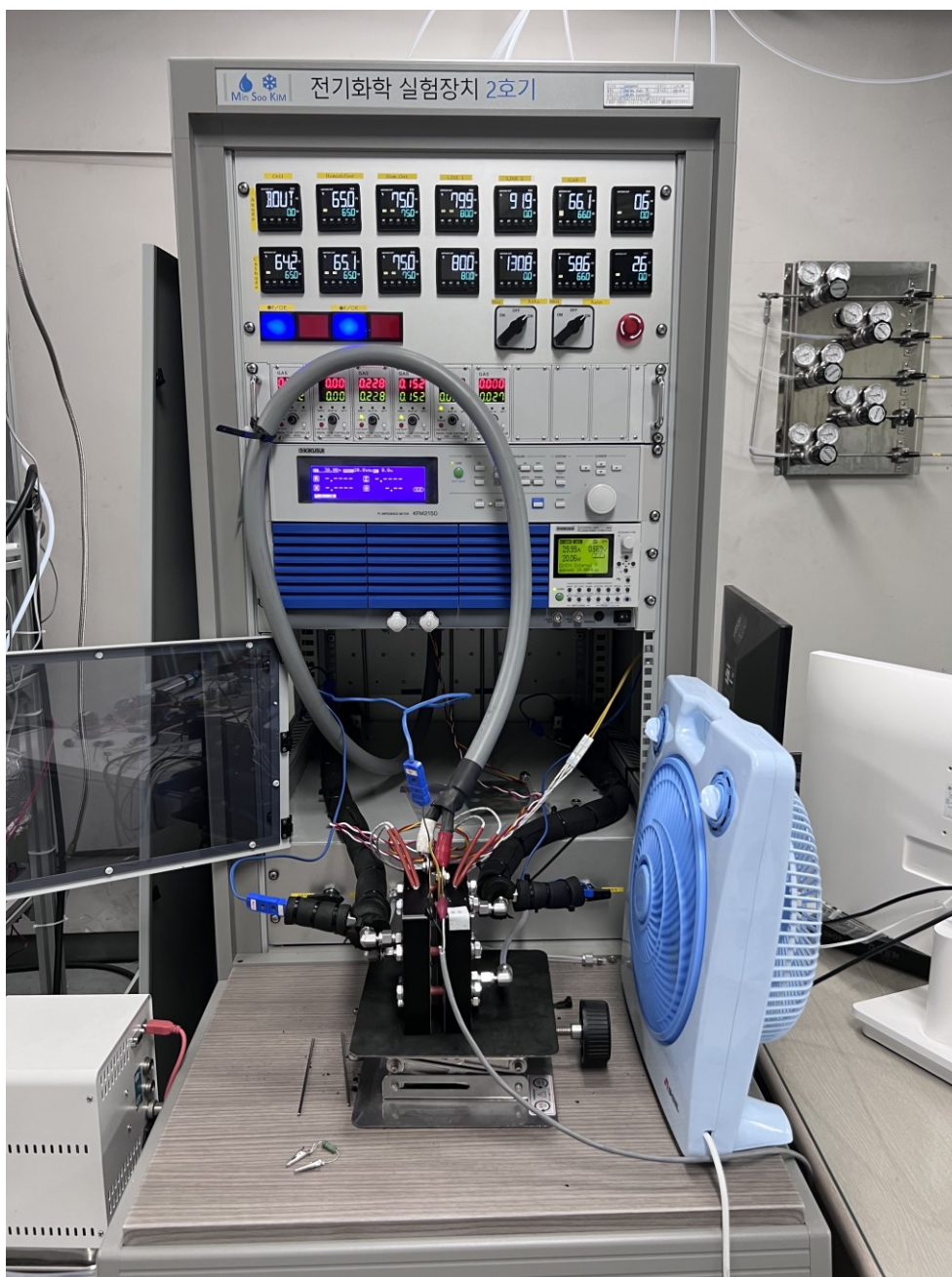
Figure 5 PEMFC testing station
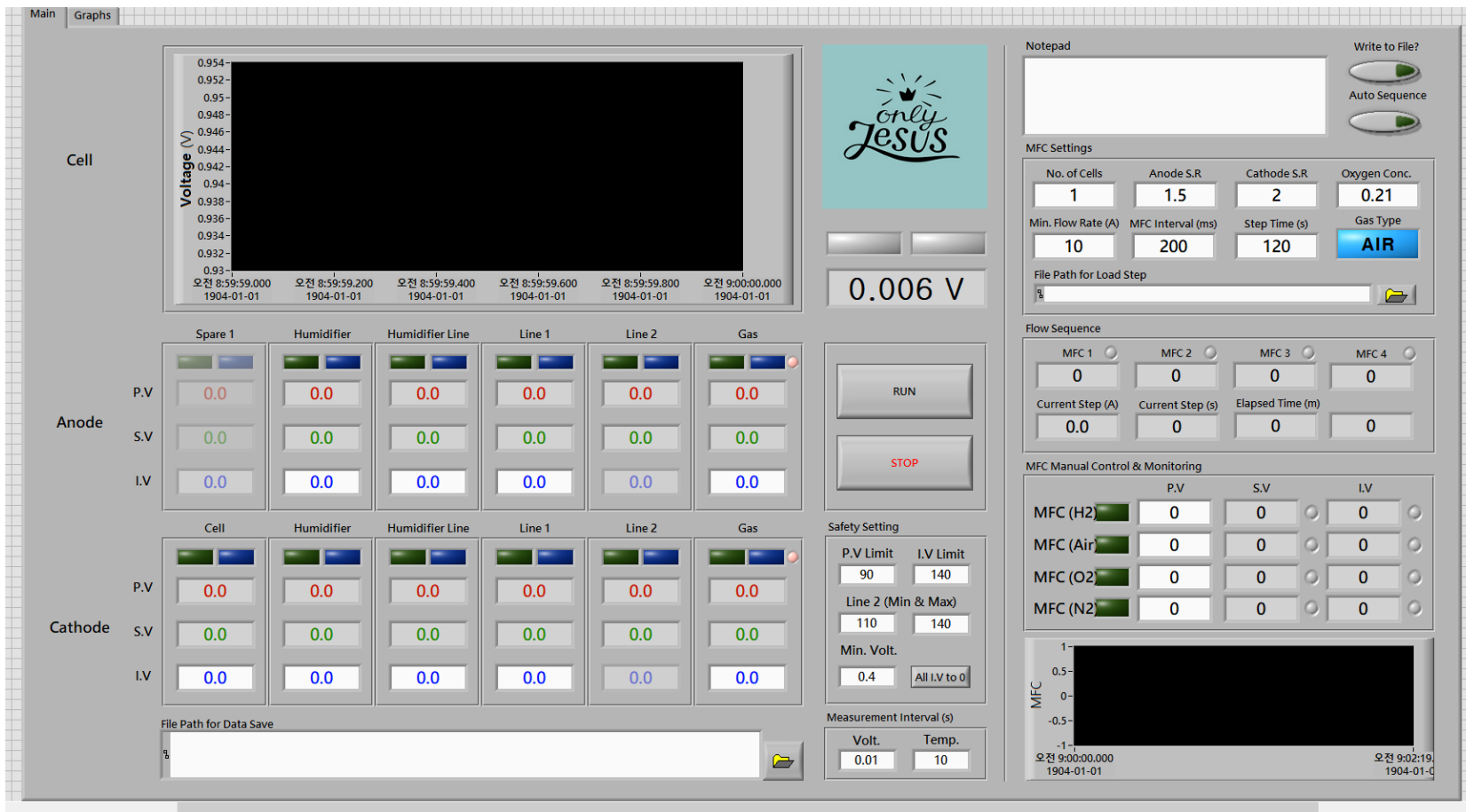
Figure 6 LabVIEW Control Panel for PEMFC testing station

2.3. Results and Discussion

2.3.1. Effect of oxygen concentration on cell performance

The feed gas oxygen concentration profoundly influences the performance of a PEMFC. The relationship can be understood through the Nernst and Butler-Volmer equation.

The Nernst equation, presented in Eq (2.1), provides insights into how the reversible voltage of the cell is influenced by temperature and concentration changes. It embodies the notion of activity, represented as α, illustrating the ratio of gas partial pressure to the standard-state pressure (1 atm).

$$E = E^0 + \frac{\Delta \hat{s}}{nF}(T - T_0) - \frac{RT}{nF} \ln \frac{\prod a_{products}^{v_i}}{\prod a_{reactants}^{v_i}} \tag{2.1}$$

Here, E^0 and v_i signify the standard-state reversible voltage and the stoichiometric coefficient of activity, respectively.

As seen in Eq. (2.2), the Butler-Volmer equation elucidates how the oxygen concentration affects the cathode reaction rate, influencing the overvoltage.

$$j = j_0^0 \left(\frac{c_{Reactant}^*}{c_{Reactant}^{0*}} e^{\frac{\alpha nF\eta}{RT}} - \frac{c_{Product}^*}{c_{Product}^{0*}} e^{\frac{-(1-\alpha)nF\eta}{RT}} \right) \tag{2.2}$$

Within this equation, $\eta, n, c^*, c^{0*}, and\ j_0^0$ denotes the voltage drop, the number of electrons transferred, the actual surface concentration, the reference concentration, and the reference exchange current density, respectively.

Figure 7 presents a PEM fuel cell's current-voltage curves under various oxygen concentrations. The figure illustrates that the cell voltage nears 0.4V at only 1.75 A/cm² for the air case. However, the current density at a similar voltage

escalates with increasing oxygen concentration. Therefore, oxygen concentration higher than 80% can draw more than 4.00A/cm^2 of current at 0.4V, offering 2.2 times more current for the same voltage. The curves from oxygen concentration 21%, which is air, to 60% display similar displacements among the curves. However, as the oxygen concentration increases, the distance between curves becomes closer, suggesting that increasing oxygen concentration beyond 60% might be less efficient.

Given that the humidification of reactant gases is constant for all cases, it can be assumed that the ohmic resistance is similar if we disregard the electro-osmotic drag and back diffusion. Consequently, the voltage difference from the low current density area is primarily attributed to the Nernst Equation and Butler-Volmer equation. Notably, there is a change in slope between the middle to high current density region. For example, the air case has a distinct slope change at 1.125A/cm^2. This sudden change in slope might be the indicator of mass transport loss or concentration loss. Other electrochemical measuring techniques, such as EIS, are required to understand the electrochemical reaction within the fuel cell.

Figure 9 represents the standard deviation of the voltage of current-voltage tests. The voltage standard deviation indicates how effectively and stable oxygen is transported to the catalyst surface. Factors such as liquid water formation and local flooding in the catalyst or channel impact the oxygen transport to the catalyst surface, resulting in voltage fluctuation. Even though the current-voltage curves are similar, the voltage fluctuations might differ. Therefore, it is crucial to observe the voltage standard deviation.

This graph shows that the air has the highest fluctuation, which decreases as the oxygen concentration increases. Since our experiments maintained a fixed

cathode stoichiometric ratio of 2.0, an increase in oxygen concentration resulted in a decreased flow rate. The reduced flow rate could increase channel flooding as the water removal gas speed decreases. Notably, there is no abrupt increase in standard deviation at higher oxygen concentrations, suggesting that significant flooding is not observed in all cases.

Figure 8 depicts power density curves under various oxygen concentrations. A consistent pattern emerges, showing that the peak power density increases with oxygen concentration. However, the growth in peak power density with increasing oxygen concentration is not linear. We measured the peak power density in all cases, demonstrating the effectiveness of our chosen active area for the tests.

Table 5 consolidates these observations, presenting the maximum power output under various oxygen concentrations. Despite the general trend of escalating power density with oxygen concentration, the rate of increasing attenuates at higher concentrations. For instance, each 10% increment in oxygen concentration from ambient level to 40% leads to a correspondingly significant boost in maximum power output, approximately 30% per each 10% oxygen concentration increment. Yet surpassing an oxygen concentration of 40% leads to a decline in performance enhancement, with the power density difference between 80% and 100% oxygen concentration being a mere 0.04 W/cm^2. Still, pure oxygen increases the maximum power density from 0.73 to 1.73 W/cm^2, more than double. By increasing the feed gas from air to enriched oxygen, the same cell can achieve over double the power output. This possibility is enticing for many researchers as it implies the potential for reducing stack size, number of cells, catalyst loadings, and other materials.

These outcomes propose that increasing oxygen concentration can improve fuel cell performance but not without a trade-off. Achieving higher purity oxygen feed gas necessitates more significant energy expenditure, suggesting that an optimal oxygen feed gas concentration might exist. This balance point between augmenting fuel cell power and the corresponding increase in the balance of plant (BoP) energy consumption is the topic for further research in the subsequent chapters.
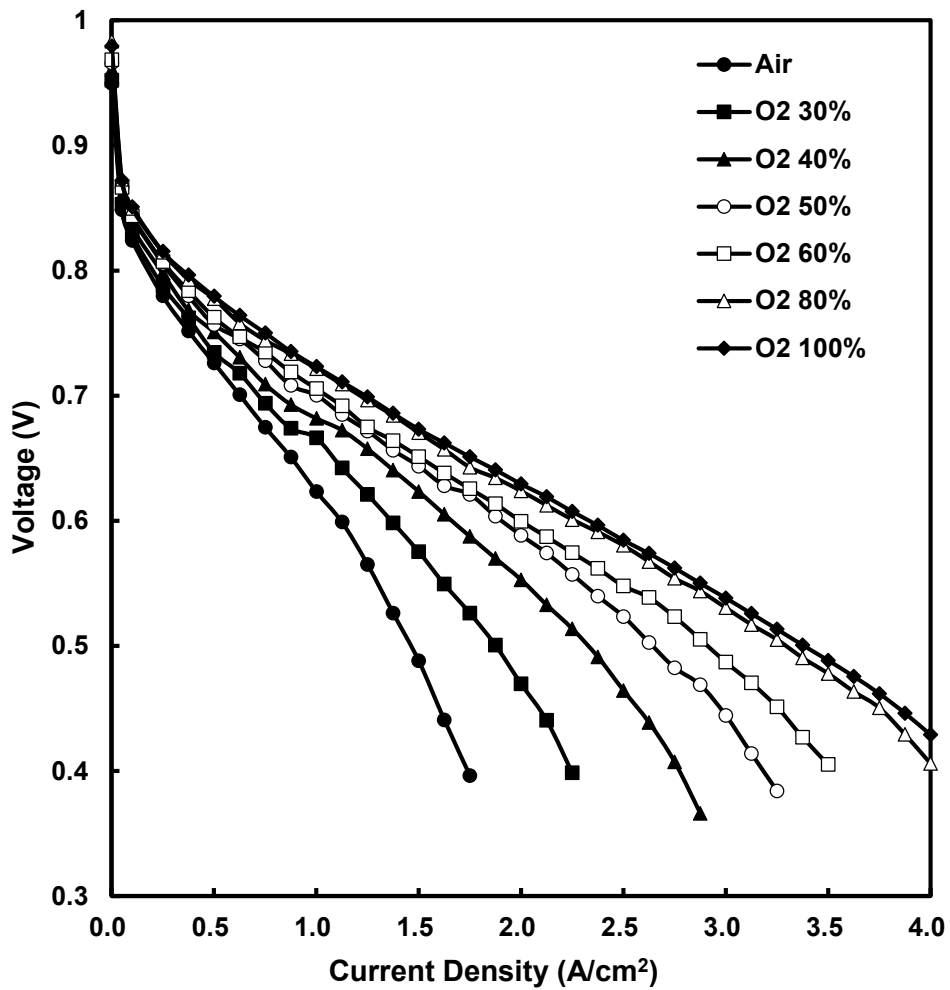
Figure 7 Polarization curves of a PEMFC under different oxygen concentrations
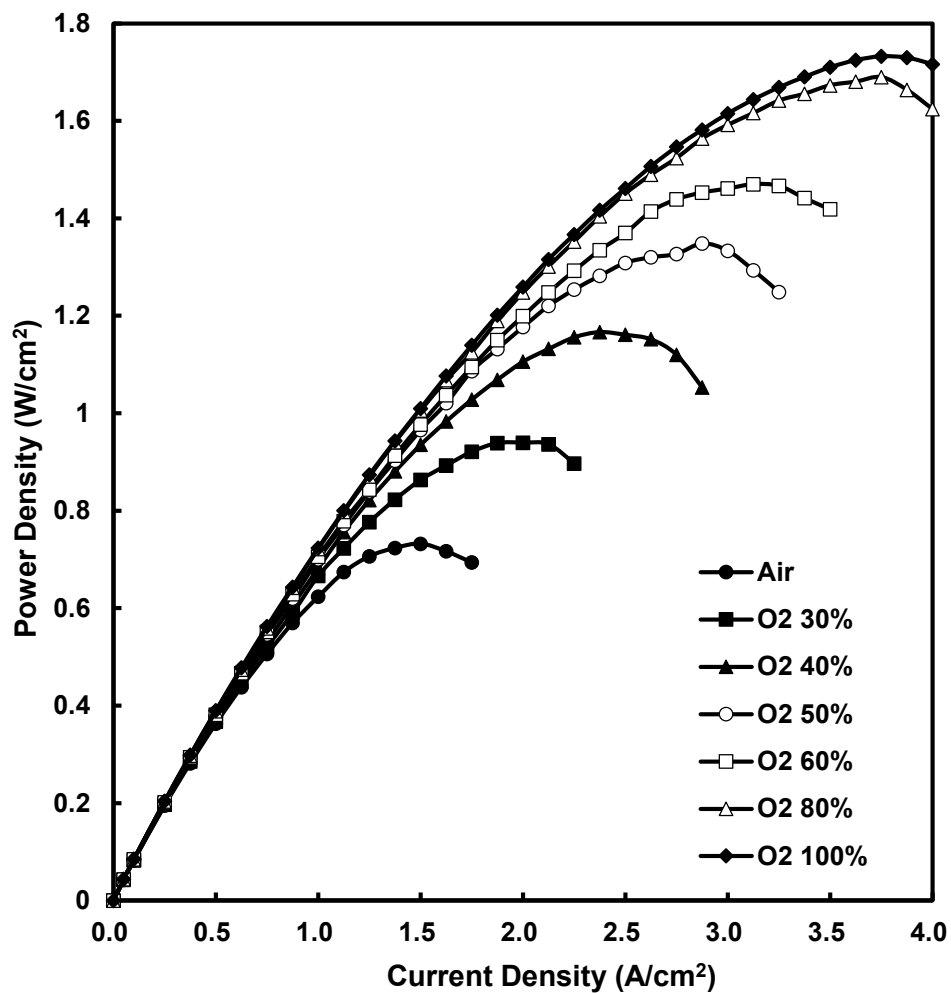
Figure 8 Power density curves of a PEMFC under various oxygen concentrations
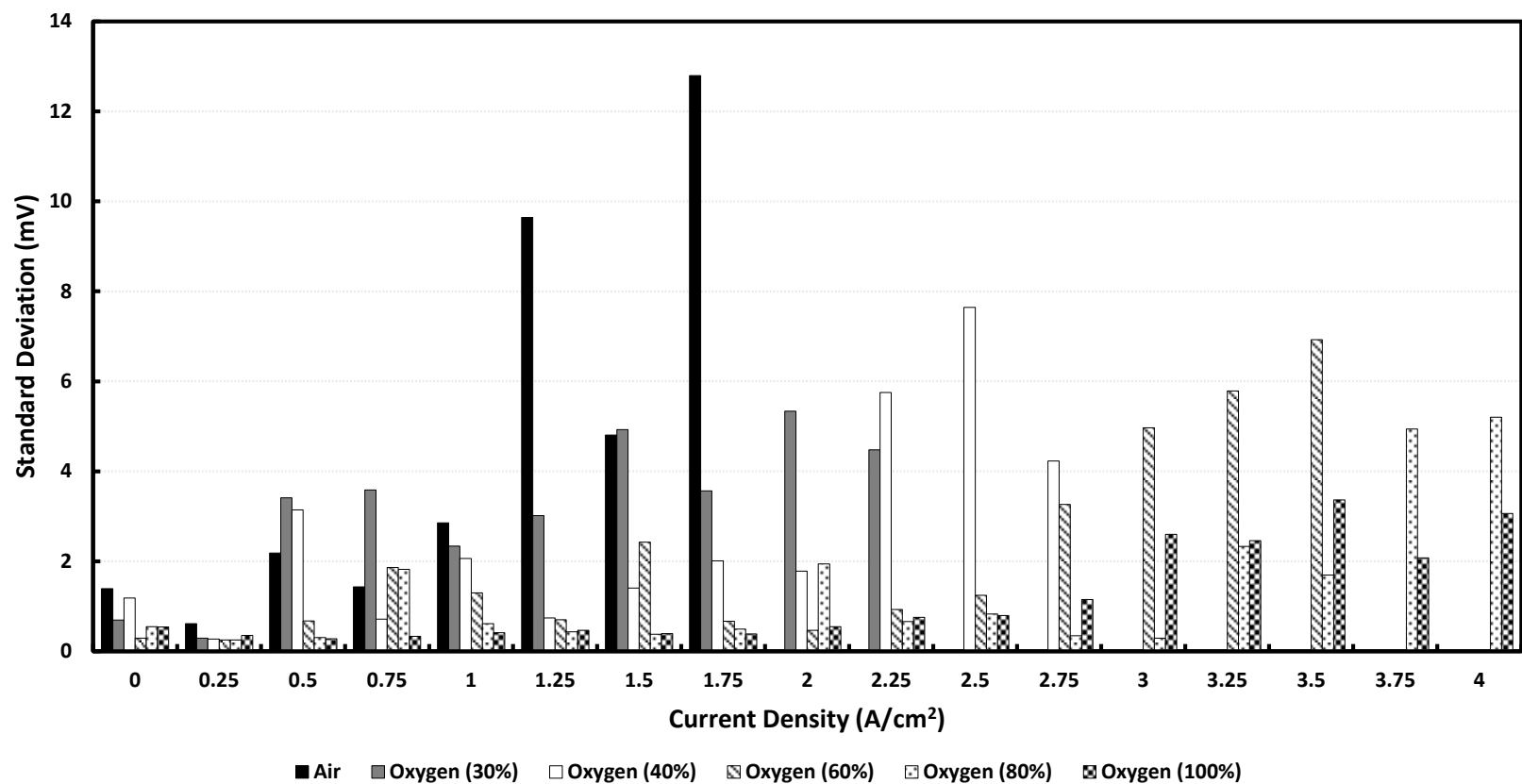
Figure 9 Standard deviation voltage of PEM fuel cell under various oxygen concentrations

Table 5 Effect of oxygen concentrations on OCV and maximum power density

Oxygen Concentration (%)	Open Circuit Voltage (V)	Maximum Power Density (W/cm^2)	Maximum Power Increase (%)
21 (Air)	0.950	0.73	Base
30	0.952	0.94	28
40	0.961	1.17	59
50	0.966	1.35	84
60	0.968	1.47	101
80	0.983	1.69	131
100	0.979	1.73	137

Electrochemical impedance spectroscopy (EIS) was performed for detailed analysis, and the acquired EIS data was then interpreted through fitting with an appropriate equivalent circuit. **Figure 10** shows an example of EIS measurement data, a graphical illustration of impedance value interpretation, and shows the equivalent circuit used for fitting EIS data of the PEM fuel cell. Interpreting impedance necessitates employing equivalent circuits that model the electrochemical reactions of the cell. These circuits typically combine elements like resistance, capacitance, inductance, and Warburg. In our analysis, we modified and applied widely-used Randles circuits for interpreting the measurements. This circuit incorporates the ohmic resistance (Ro), representing the combined proton and electron resistance, the charge transfer (R_{ct}), and the constant phase element (CPE_{dl}), which captures the non-ideal double-layer capacitance behavior due to rough and porous catalyst layers. Furthermore, a finite-length Warburg diffusion element (Z_w) compensates for mass transport losses. The CPE and Warburg elements comply with formulas (2.3) and (2.4), respectively. [27], [28]

$$Z_{CPE} = \frac{1}{T_{CPE} \cdot (j \cdot \omega)^{P_{CPE}}} \qquad (2.3)$$

$$Z_W = R_{Zw} \cdot \frac{\tanh(j \cdot \omega \cdot T_{Zw})^{P_{Zw}}}{(j \cdot \omega \cdot T_{Zw})^{P_{Zw}}} \qquad (2.4)$$

Here, the time constant, T_{Zw} is defined as $T_{Zw} = \frac{L^2}{D}$ L symbolizes the effective diffusion thickness, and D represents the effective diffusion coefficient.

During the process of selecting an appropriate equivalent circuit for our EIS measurement, we noted a slight inductive behavior within the high-frequency range.

Typically, inductive reactance characteristics manifest in two distinct frequency bands: high (above 2.5 kHz) or low (below 0.1 Hz). It is well-established that high-frequency inductive behavior is usually attributed to the electric cables and wiring inherent to the system. Conversely, low-frequency inductive behavior is often associated with side reactions involving intermediate species, water transport dynamics, and carbon monoxide poisoning [29], [30]. In our analysis, only the high-frequency inductive behavior was observed in our cases, even though we utilized low-inductance cables. Consequently, we incorporated an inductor into the Randles circuit to accurately represent this behavior and comprehensively fit our EIS measurement data.

The effectiveness of the proposed equivalent circuit was evaluated using Chi-squared tests, represented by the formula (2.5):

$$\chi^2 = \sum \frac{(O_i - E_i)^2}{E_i} \qquad (2.5)$$

In Nyquist plots, high-frequency region intercepts with real axis, referred to as high-frequency resistance (R_o), indicate the ohmic resistance of the PEM fuel cell components, including membrane, GDL, and bipolar plate resistance. However, the contribution of the membrane typically dominates over the other components [8]. Variations in total ohmic resistance during fuel cell are due to changes in membrane ionic conductivity, influenced by different levels of MEA hydration [31]. The first semicircular arc in the higher frequency range of 10 – 10,000 hertz indicates the anode and cathode's charge transfer resistance. This arc often comprises two overlapping arcs, with the cathode arc overshadowing a smaller anode arc. The

second semicircular arc appearing in the low-frequency range of 0.5 to 10 hertz represents impedance from the oxygen transport limitation to the electrode.

Figure 11 through **Figure 21** present the Nyquist and Bode plots for a PEM fuel cell under various oxygen concentrations at 30A and 60A, where applicable. Nyquist plots use orthonormal representation to preserve the impedance angle. The markers on these plots represent the actual measurement data, while the lines indicate the simulated data based on the fitted equivalent circuit. As exemplified in **Figure 22**, the inclusion of an inductor facilitated the high-frequency phase angles to match the experimental data across all cases closely.

The equivalent circuit with anode R-CPE, as illustrated in Figure 10(b), represented the fuel cell behavior adequately throughout the cases, excluding the pure oxygen one. This adequacy is confirmed by a low chi-squared value, reaching a maximum of a mere $8.88e^{-4}$. However, the Nyquist plot for the pure oxygen case demonstrated near single semi-circle shapes, and only one peak on phase angle is observed, contrasting with the other cases. As a result, the equivalent circuit for the pure oxygen case was modified by eliminating the anode resistance and constant phase element (see **Figure 10(c)**). These modifications were then applied to simulate the fitting.

Figure 11 illustrates the EIS measurement for the air case, with air being the lowest oxygen concentration in our experimental condition. Consequently, it shows the highest impedance value of 1.63 ohm·cm^{-2}. The Nyquist plot displays two semi-circles, each representing a different time constant in the fuel cell. Two semi-circles are typical for PEM fuel cells and signify two dominant processes: mass transport phenomena and charge transfer kinetics. On the other hand, the Bode plots

reveal two peaks in phase angle at 8 and 25.1 Hz. These peaks provide critical insights into the dynamic behavior and performance of the PEM fuel cell.

The low-frequency peak is representative of mass transport limitations, suggesting that the performance is significantly influenced by. Mass transport refers to the transport of reactant gas, in this case, oxygen gas, to the active sites of the catalyst, which can be hindered due to various factors, including water flooding, leading to a delay in the system and hence the phase shit observed. The high-frequency peak is associated with charge transfer kinetics, which involves the electrochemical reactions occurring on the catalyst surfaces. The presence of this peak suggests that the rates of these electrochemical reactions substantially impact fuel cell impedance at that frequency. In the air case, these phase peaks are quite close, indicating that both mass transport and charge transfer kinetic contribute comparably to the overall impedance and, thus, the performance of the fuel cell under these conditions.

In **Figure 12**, with an oxygen concentration of 30%, the maximum impedance value decreased notably to 0.82 ohm·cm^{-2}, almost half of the air case. This suggests an improvement in the performance, mainly due to enhanced oxygen availability for the oxygen reduction reaction (ORR) at the cathode. The two-semi-circles in the Nyquist plot appear to move apart slightly, reflecting separate dominant processes. The phase angle peaks occur at 6.3 and 50 Hz, a shift from the air case. The trend continues in **Figure 13** for the 40% oxygen case. The maximum impedance drops further to 0.52 ohm·cm^{-2} and the phase peaks are now found at 5 and 80 Hz, indicating further improved kinetics. **Figure 14** shows the scenario for a 50% oxygen concentration. Here, the maximum impedance continues to drop to 0.39

ohm·cm^{-2}. Intriguingly, the low- frequency semi-circle has a smaller arc size than the high-frequency arc, indicating significantly reduced mass transport resistance. The phase peaks are at 4 Hz and 158 Hz, with the high-frequency peak showing a larger phase angle, signaling better reaction kinetics. With 60% oxygen at 30A (**Figure 16**), the maximum impedance further reduces to 0.33 ohm·cm^{-2}. The low-frequency semi-circle is now less than half the size of the high-frequency arc, suggesting a significant reduction in mass transport. The phase peaks occur at 3.16 and 200 Hz. **Figure 18** presents the case for 80% oxygen concentration. The maximum impedance drops to 0.27 ohm·cm^{-2}, with the phase angle peaks at 3 and 251 Hz. The size of the low-frequency arc is almost one-tenth of the high-frequency arc, suggesting a small contribution to mass transport resistance. The peak at 3 Hz barely registers as a local peak, indicating the near elimination of mass transport limitation. In the pure oxygen case (**Figure 20)**, the maximum impedance dropped to the lowest value of 0.26 ohm·cm^{-2}. Interestingly, only a single semi-circle is seen on the Nyquist plot, and a single peak occurs at 300 Hz on the Bode plot. This result indicates that mass transport limitations are no longer an issue, likely due to the sufficient oxygen supply.

Overall, as we increase the oxygen concentration in the cathode feed gas, we observe a decrease in the high-frequency arc in the Nyquist plot and a shift in the low-frequency phase angle peak towards lower frequencies and the high-frequency peak toward higher frequencies in the Bode plot. This indicates enhanced oxygen transport to the reaction zone and a more efficient oxygen reduction reaction, leading to faster reaction rates and improved fuel cell performance.

This analysis extends to the performance of the PEM fuel cell under a higher current load of 60A at different oxygen concentrations. **Figure 15** corresponds

to a 50% oxygen concentration at 60A. The maximum is at 0.64 ohm·cm^{-2}, with 8 and 50 Hz phase peaks. Notably, compared to the 30A case, the impedance and arc size increased significantly. Now, the low-frequency arc is larger than the high-frequency one. This change and the shift in phase peak suggest that at 60A, the fuel cell is encountering a considerable mass transport limitation. These limitations were not evident in the current-voltage graphs. The trend continues with 60% oxygen at 60A, as shown in **Figure 17**. The maximum impedance drops slightly to 0.44 ohm·cm^{-2} with phase peaks at 6.3 and 158 Hz. However, the low-frequency arc remains larger than the high-frequency one, indicating ongoing mass transport limitations. **Figure 19** corresponds to the case with 80% oxygen at 60 A. The maximum impedance reduces further to 0.27 ohm·cm^{-2}, with phase angle peaks at 4 and 400 Hz. **Figure 21** represents the scenario with pure oxygen at 60A. The maximum impedance further reduces to 0.23 ohm·cm^{-2}, with one phase angle peak at 500 Hz. The Nyquist plot for this case exhibits a single semi-circle, suggesting that mass transport limitations have been overcome at this oxygen concentration and current level.

When comparing the 30A, and 60A scenarios, it is evident that both follow similar trends as the oxygen concentration increases – impedance decreases, and the fuel cell performance improves. However, there are differences in their high-frequency-resistance (HFR), which is the intercept with the resistance axis on the Nyquist plot. Despite both conditions being fully humidified, the higher electro-osmotic drag at 60A results in a larger amount of water being transported from the anode to the cathode, thus causing a more significant imbalance in membrane hydration. As a result, the HFR value at 60A is higher than 30A, even though the

water production at 60A is double than at 30A. This showcases the complex interplay between operating conditions, hydration levels, and fuel cell performance.

Table 6 presents the parameter values associated with the equivalent circuit representation of the PEM fuel cell, shedding light on the internal dynamics of the fuel cell and how changes influence them in current load and oxygen concentration. At 30A and 60A, the average HFR values are 2.65 mohm and 2.89 mohm, respectively, with the HFR at 60A being approximately 10% higher than 30A, mainly attributed to the membrane hydration imbalance. To address this, an anode flow field improvement was implemented, which is elaborated in chapter 5.

Furthermore, the parameter, R_{zw}, related to mass transport resistance, decreased with increasing oxygen concentration. Higher oxygen concentration suggests faster oxygen transport, reducing mass transport resistance within the fuel cell. Similarly, the sum of charge transport resistance decreases with increasing oxygen concentration, as enhanced oxygen transport facilitates electrochemical reactions. The inductance values, obtained at 30A and 60A, were fixed as they pertain solely to the electric wiring of the PEM fuel cell.
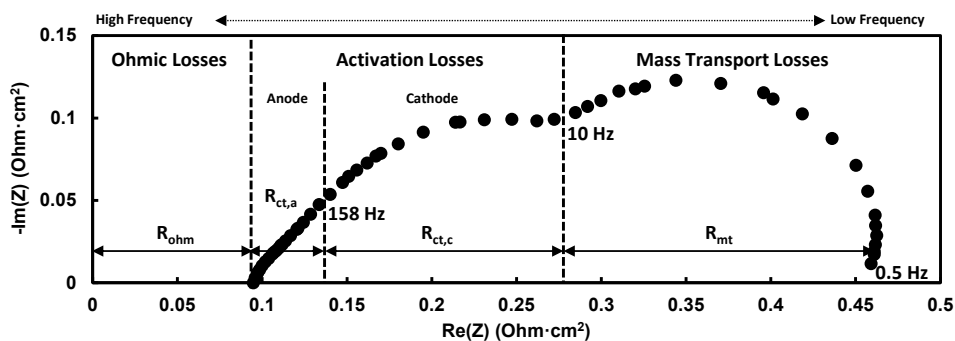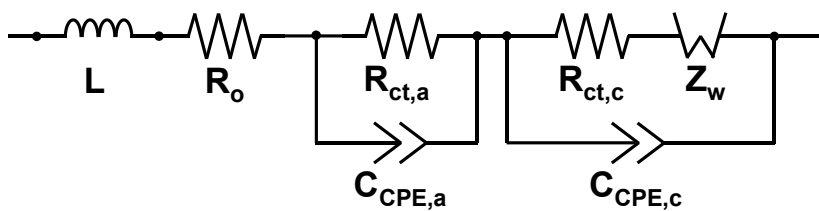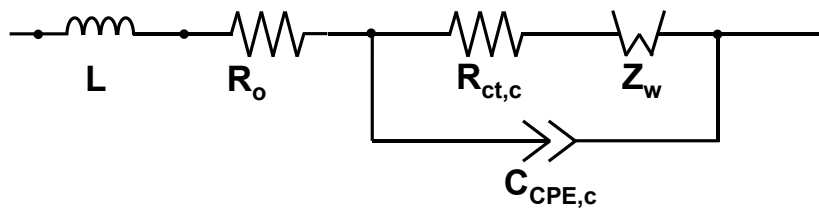
Figure 10 (a) Graphical interpretation of Nyquist plot, and

(b) Equivalent circuit used for fitting EIS measurement.

(c) Equivalent circuit used for pure oxygen case.
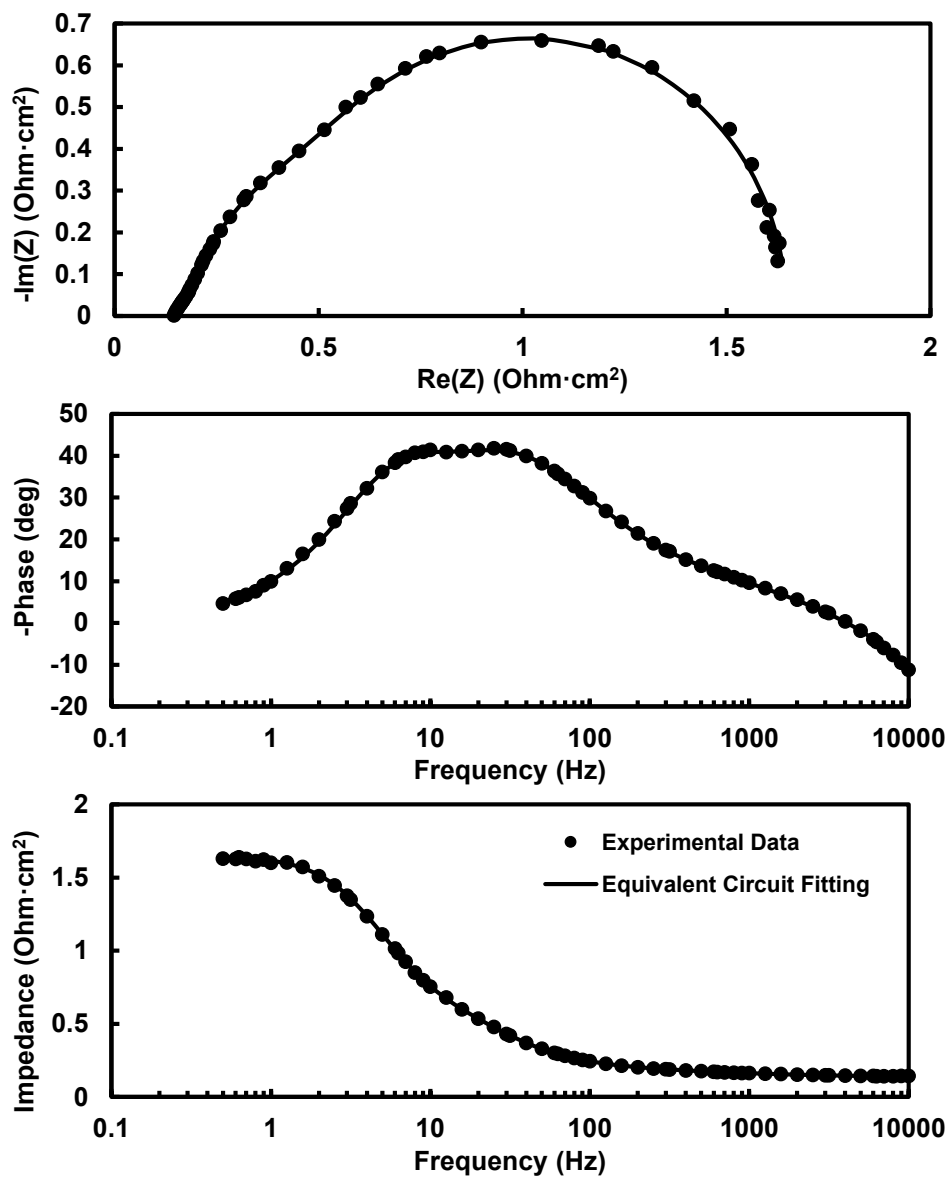
Figure 11 Nyquist and Bode plot at 30A, operating with air
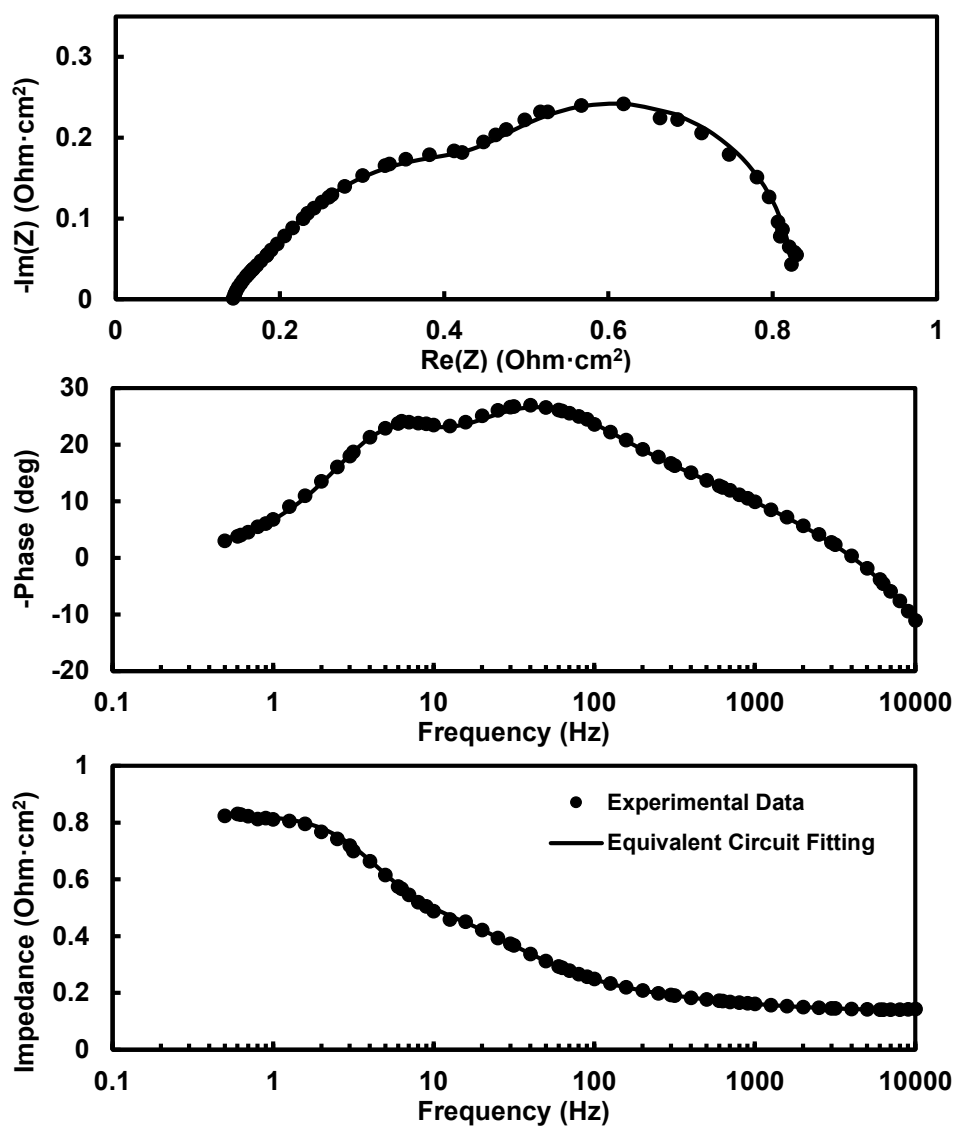
Figure 12 Nyquist and Bode plot at 30A, operating with 30% oxygen-enriched air
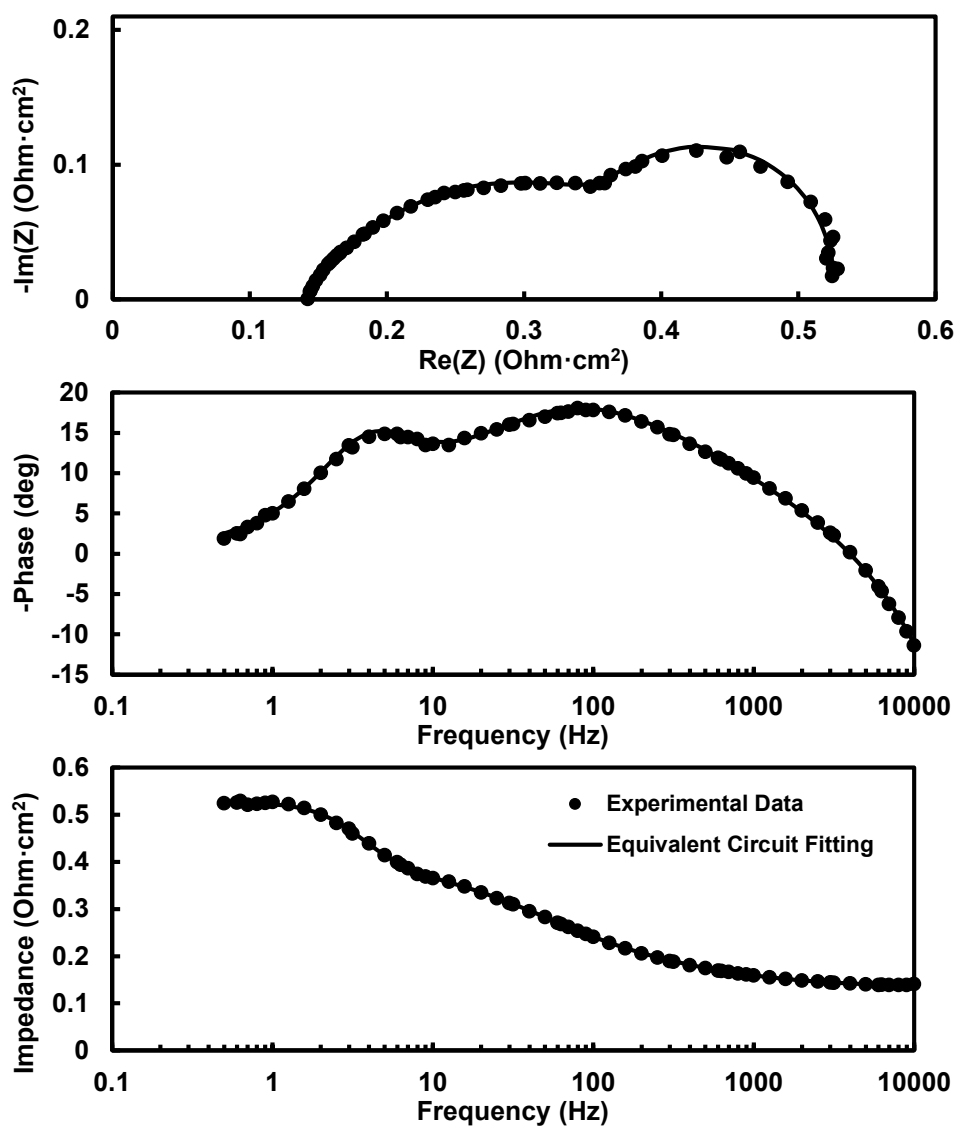
Figure 13 Nyquist and Bode plot at 30A, operating with 40% oxygen-enriched air
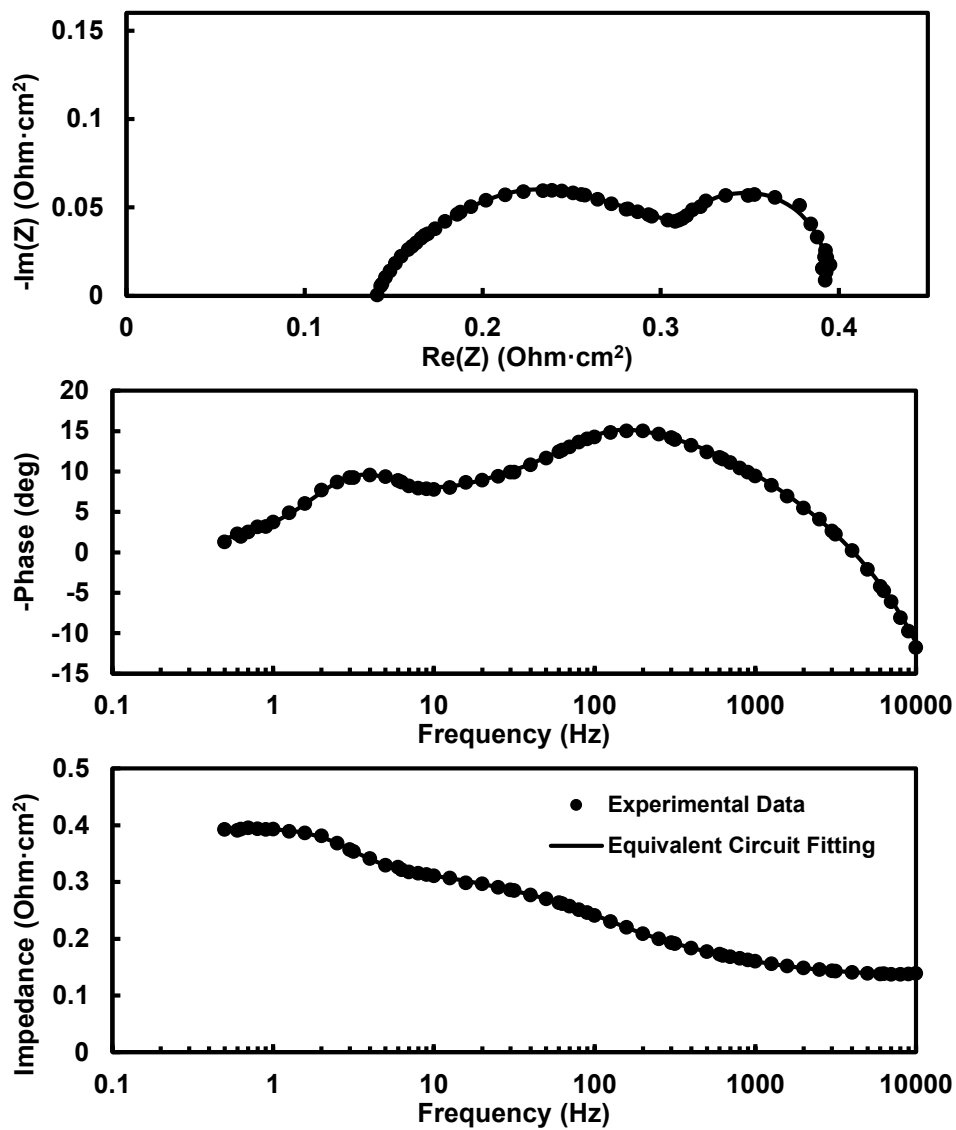
Figure 14 Nyquist and Bode plot at 30A, operating with 50% oxygen-enriched air
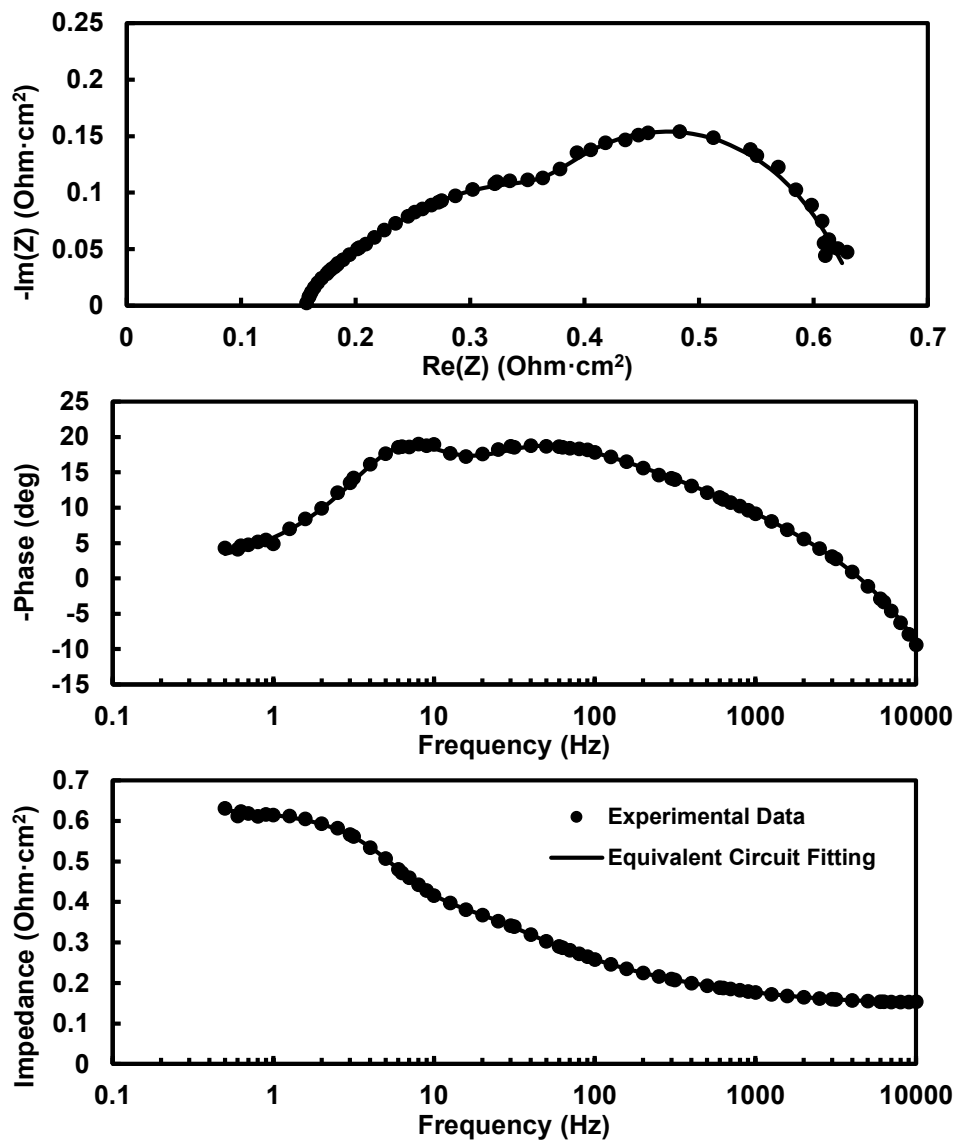
Figure 15 Nyquist and Bode plot at 60A, operating with 50% oxygen-enriched air
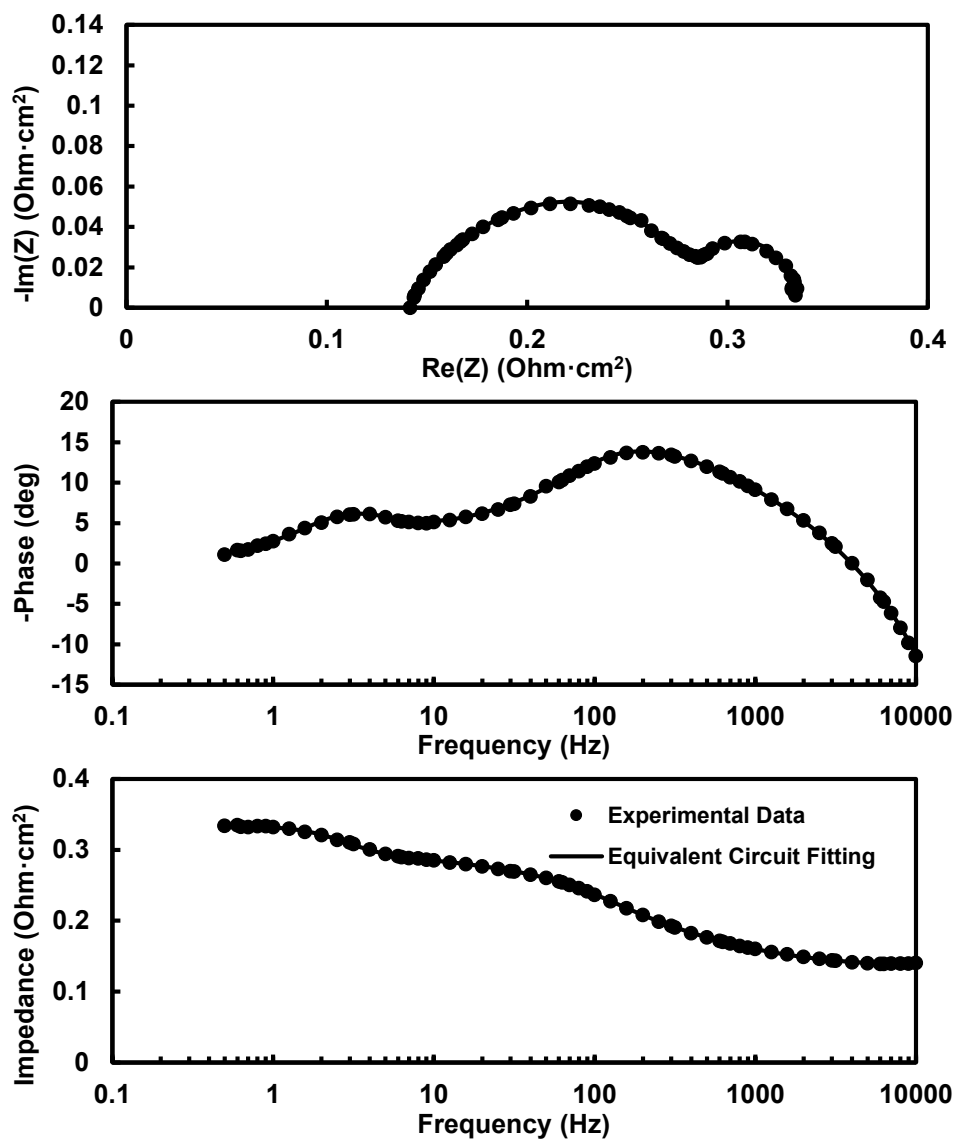
Figure 16 Nyquist and Bode plot at 30A, operating with 60% oxygen-enriched air
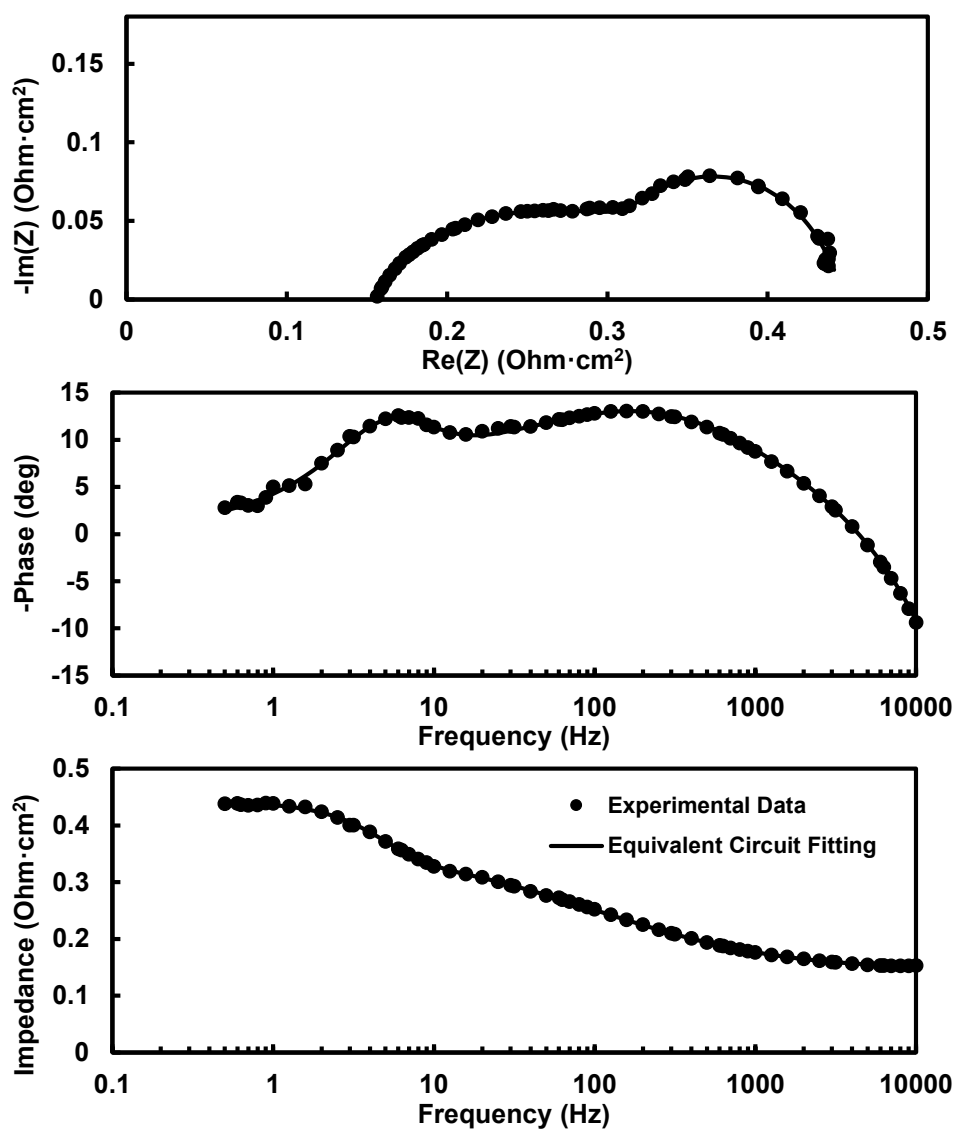
Figure 17 Nyquist and Bode plot at 60A, operating with 60% oxygen-enriched air
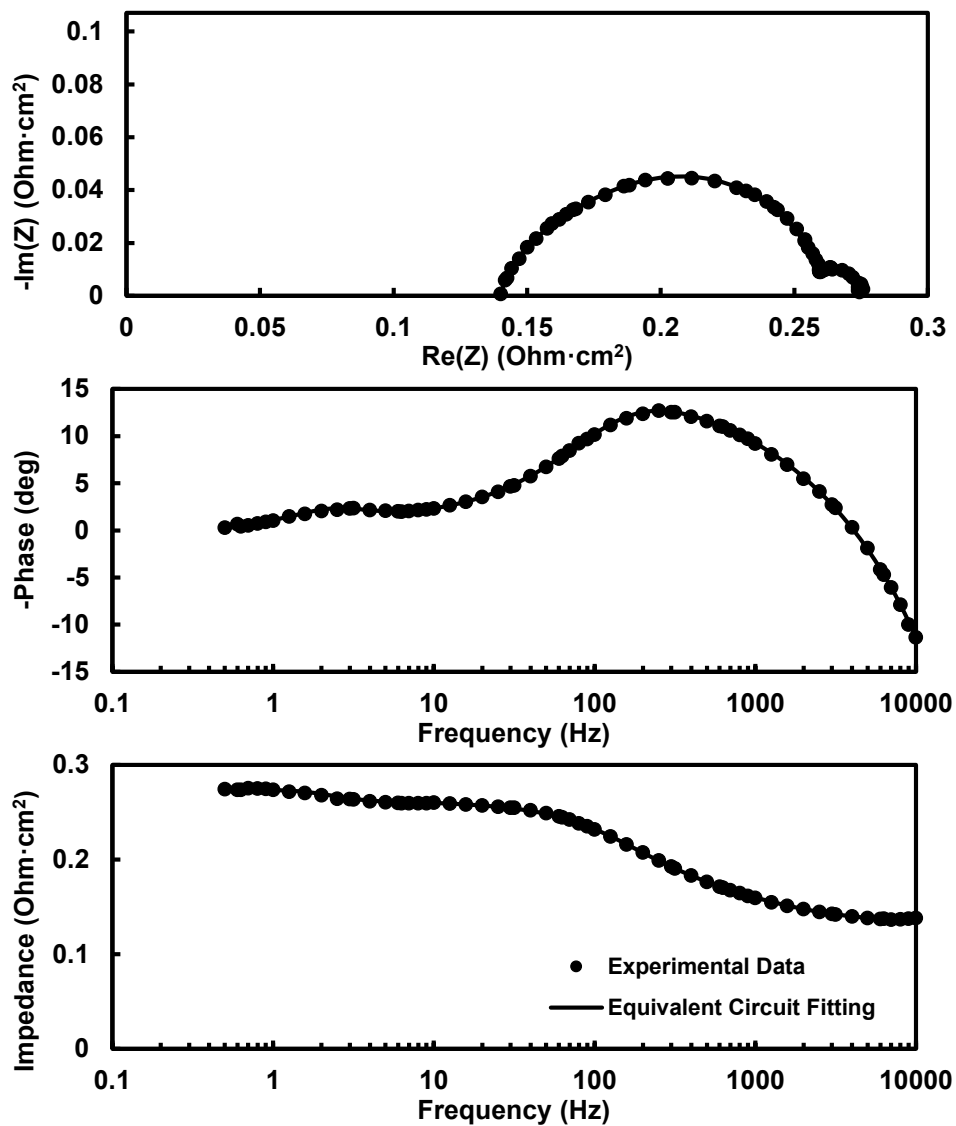
Figure 18 Nyquist and Bode plot at 30A, operating with 80% oxygen-enriched air
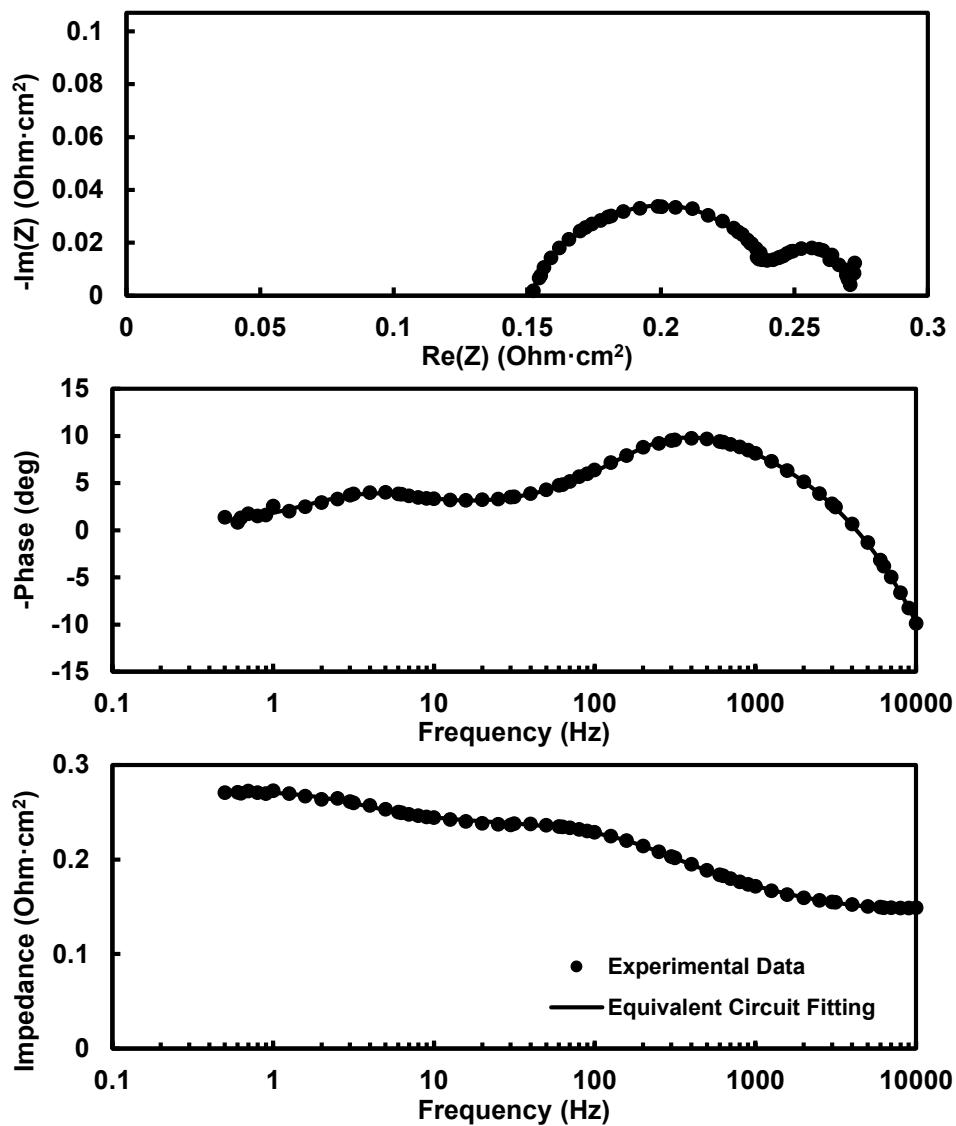
Figure 19 Nyquist and Bode plot at 60A, operating with 80% oxygen-enriched air
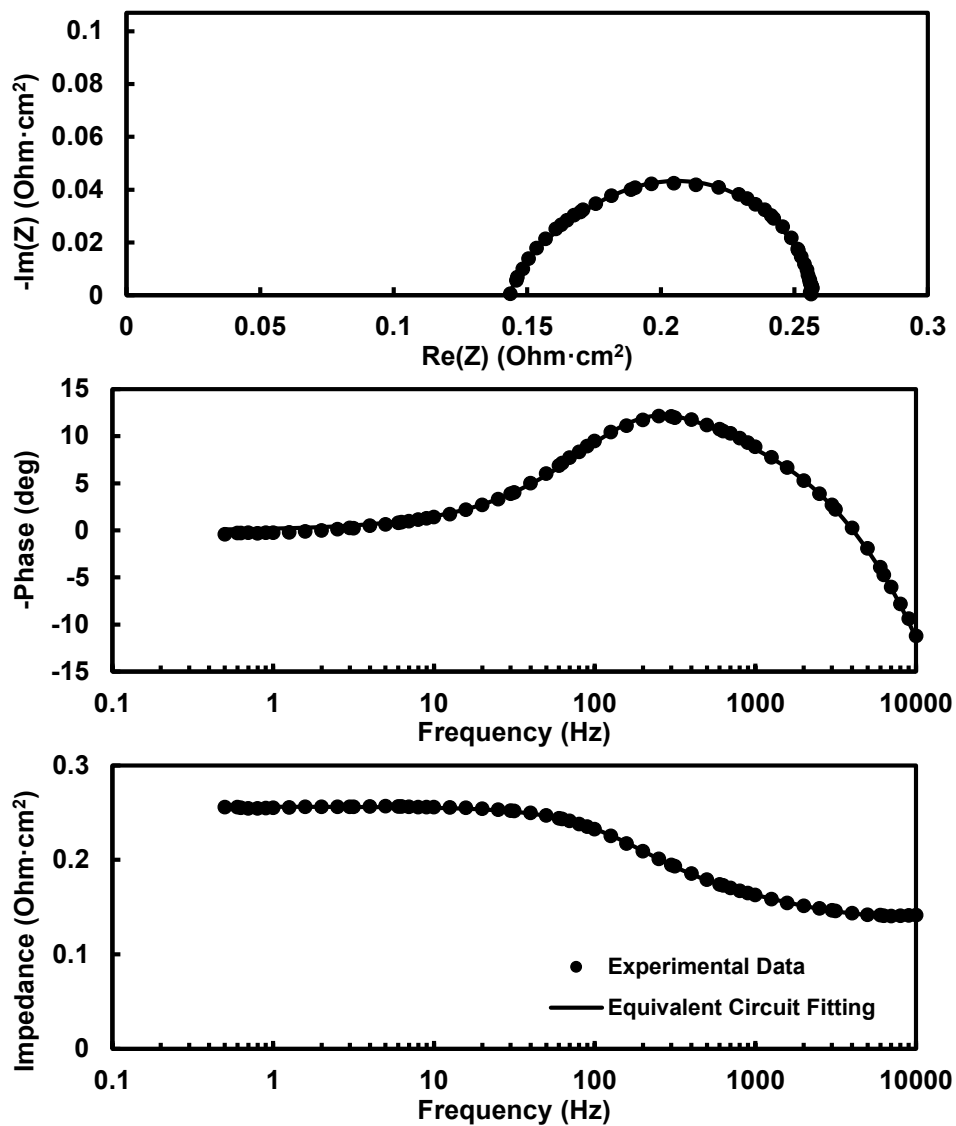
Figure 20 Nyquist and Bode plot at 30A, operating with pure oxygen
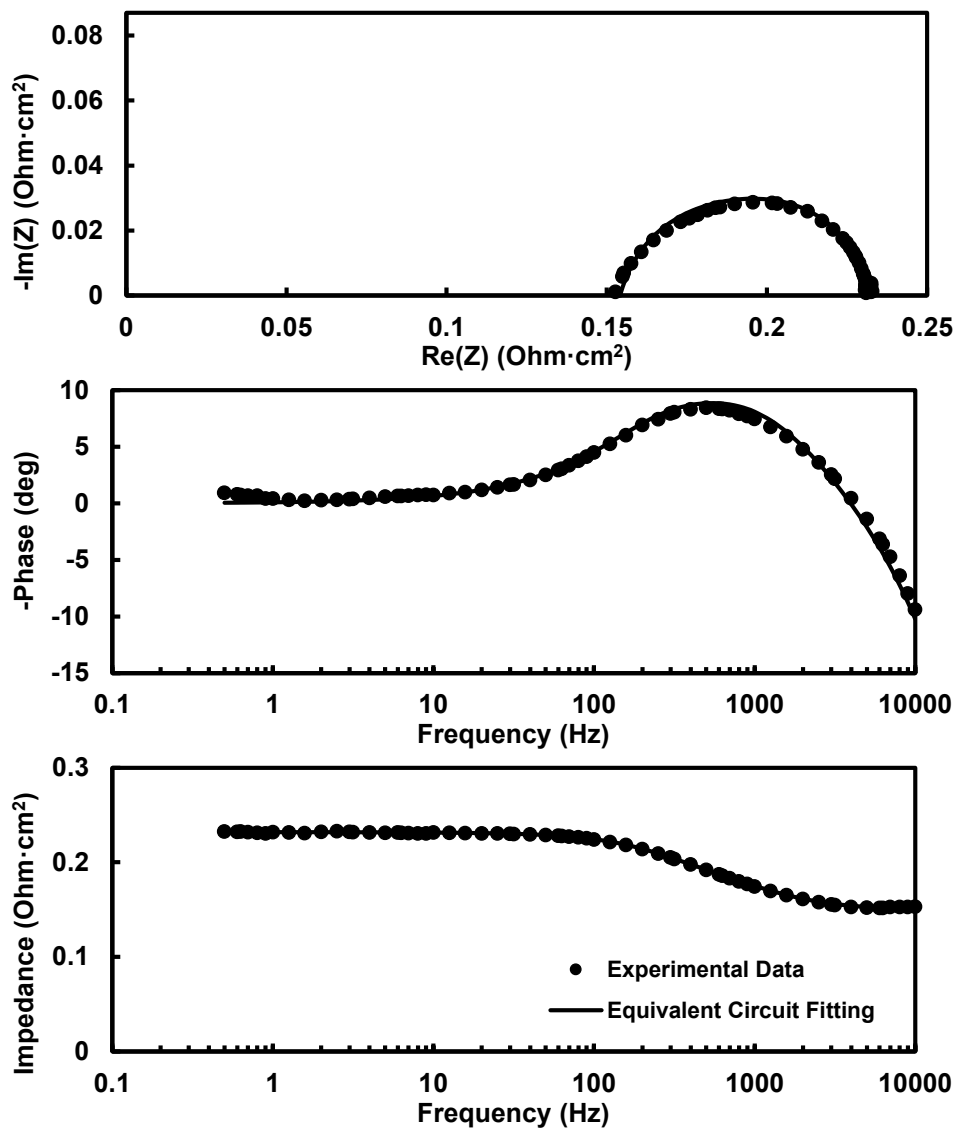
Figure 21 Nyquist and Bode plot at 60A, operating with pure oxygen
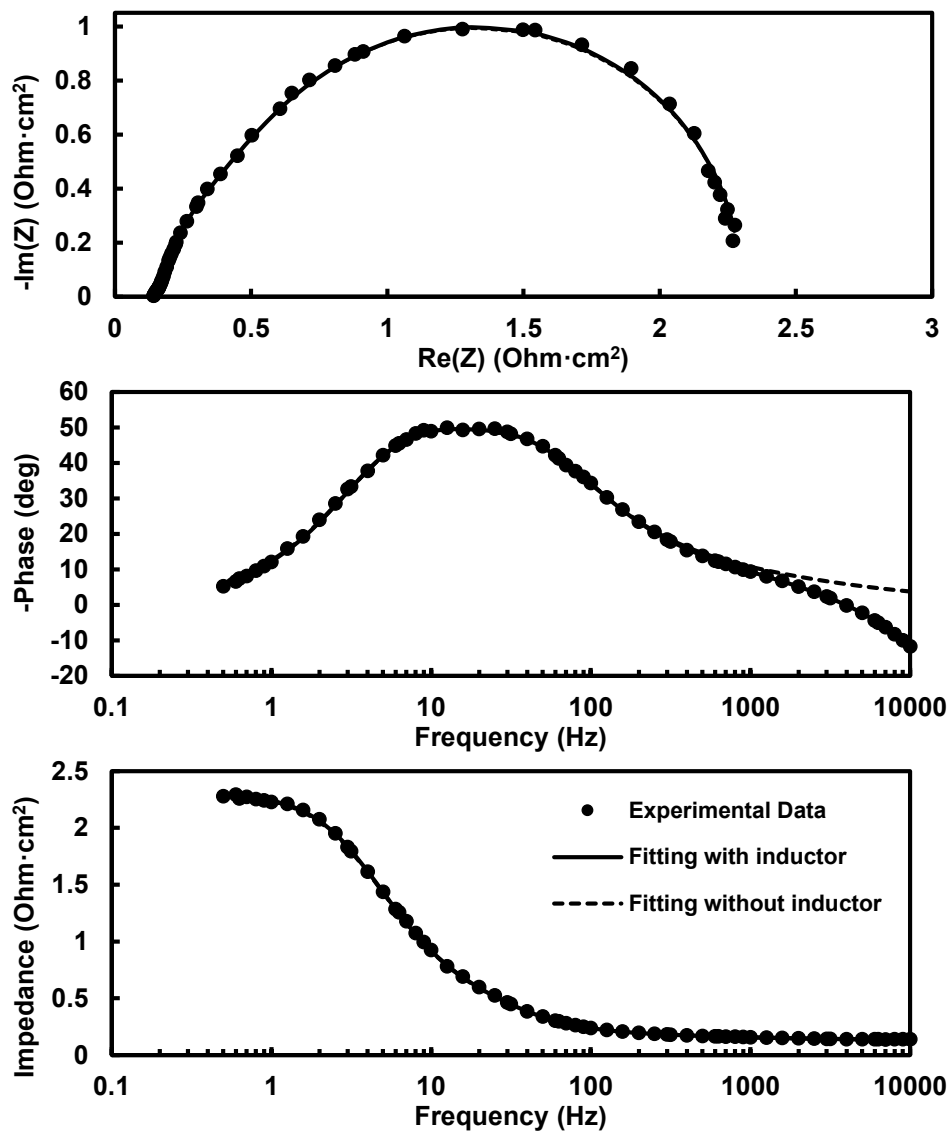
Figure 22 Effect of the inductor in EIS fitting

Table 6 Parameter values of equivalent circuits for oxygen concentration tests

Oxygen Conc.	Current (A)	R_o (mΩ)	$R_{ct,a}$ (mΩ)	$R_{ct,c}$ (mΩ)	R_{Zw} (mΩ)	T_{Zw}	P_{Zw}	$T_{CPE,a}$	$P_{CPE,a}$	$T_{CPE,c}$	$P_{CPE,c}$	L (mH)	$\chi2$ (-)
Air	30	2.697	1.457	11.979	16.782	0.058	0.555	0.004	0.643	0.001	0.980	1.13E-05	8.88E-04
30%	30	2.652	1.887	5.352	6.606	0.077	0.562	0.004	0.645	0.001	0.968	1.13E-05	1.97E-03
40%	30	2.620	1.009	3.958	2.988	0.090	0.582	0.002	1.084	0.006	0.607	1.13E-05	3.41E-04
50%	30	2.604	0.227	3.429	1.631	0.113	0.594	0.000	1.417	0.004	0.648	1.13E-05	1.77E-04
50%	60	2.867	1.970	3.282	4.825	0.057	0.605	0.004	0.925	0.006	0.590	1.07E-05	4.88E-04
60%	30	2.635	0.659	2.408	0.966	0.124	0.582	0.001	1.105	0.003	0.663	1.13E-05	8.46E-05
60%	60	2.888	0.547	3.127	2.445	0.065	0.603	0.013	0.633	0.005	0.640	1.07E-05	3.71E-04
80%	30	2.615	1.079	1.510	0.262	0.138	0.637	0.002	0.742	0.001	0.943	1.13E-05	1.19E-04
80%	60	2.841	0.926	0.935	0.760	0.107	0.496	0.001	0.974	0.001	0.758	1.07E-05	2.18E-04
100%	30	2.725	*	0.664	1.739	0.002	0.454	*	*	0.000	0.925	1.13E-05	1.09E-04
100%	60	2.969	*	1.369	0.301	0.001	0.537	*	*	0.000	0.872	1.07E-05	7.38E-05

※　For the pure oxygen case, a simplified equivalent circuit was employed.

2.3.2. Comparison between pressurization and oxygen enrichment.

An alternative approach to enhance fuel cell performance without component modifications is the pressurization of the system. As per the Nernst equation, the OCV increases with the overall pressure increase. Higher pressure creates a greater pressure gradient toward the catalyst surfaces, facilitating mass transport. The reactant gas partial pressure also rises with increased system pressure, reducing activation overvoltage.

Figure 23 shows the polarization curves under both pressurized and oxygen-enriched conditions. While pressurization improves the cell's performance, it does not achieve the same level of enhancement as seen with a 30% oxygen concentration feed. In Figure 24, the power density curves reveal significant differences between the two strategies. When the pressure is increased from 0 to 0.5 bar and then to 1 bar, we observed an increase in maximum power density from 0.69 W/cm^2 to 0.80 W/cm^2 and then to 0.86 W/cm^2. This represents an increase of 16% and 25%, respectively. However, when the oxygen concentration is increased to 30% and 40%, the maximum power density jumps remarkably from 0.69 W/cm^2 to 0.95 W/cm^2 and then to 1.18 W/cm^2, indicating a substantial increase of 38% and 71%, respectively. The standard deviation voltage graphs in Figure 25 further substantiate the superior performance of the oxygen-enriched approach showing a smaller variance in voltage.

Figure 26 to Figure 30 shows the Nyquist and Bode plots for each case, offering more detailed insight into the frequency response characteristics of the fuel cell under different conditions. Figure 31 compiles all the data and indicates that while the low-frequency arc decreased with pressurization, it was not more effective

than oxygen enrichment. Additionally, **Table 7** presents the parameter values for fitting the EIS measurement data, providing quantitative analysis. These findings further solidify that oxygen enrichment offers more significant improvement than pressurization.
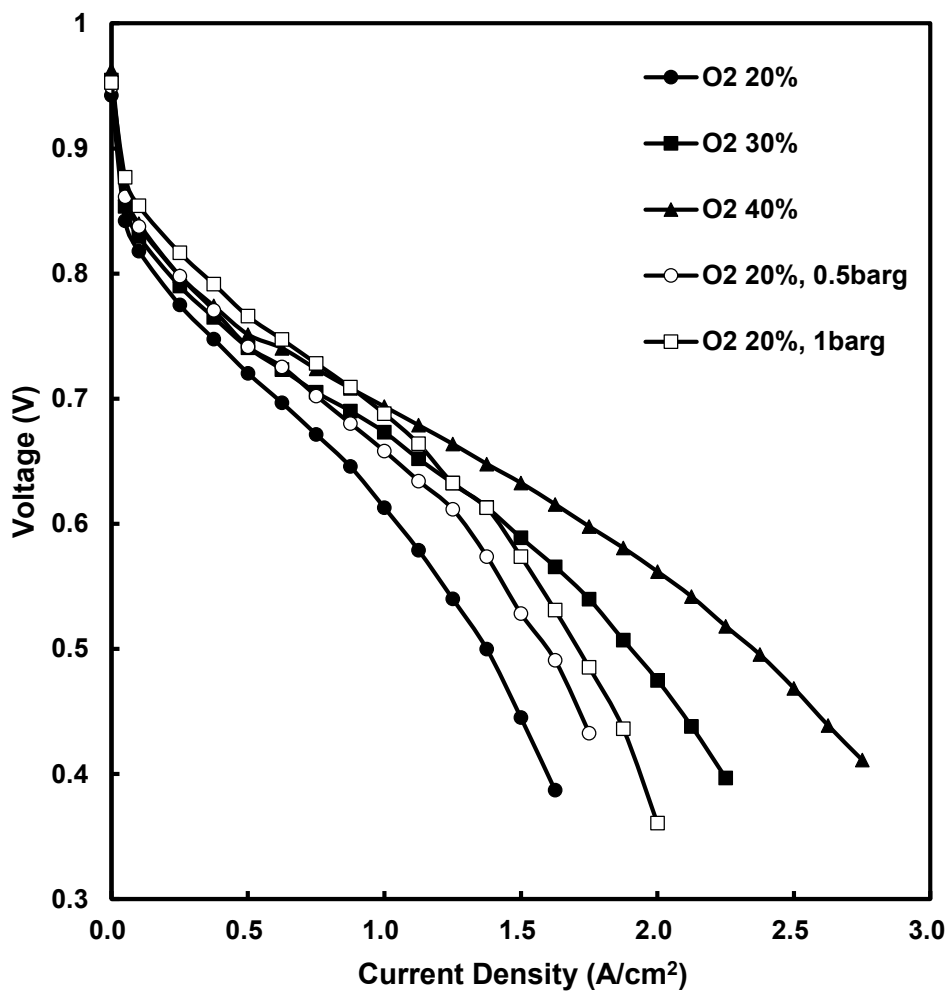
**Figure 23 Comparative polarization curves of a PEMFC under pressurization and
oxygen enrichment conditions**
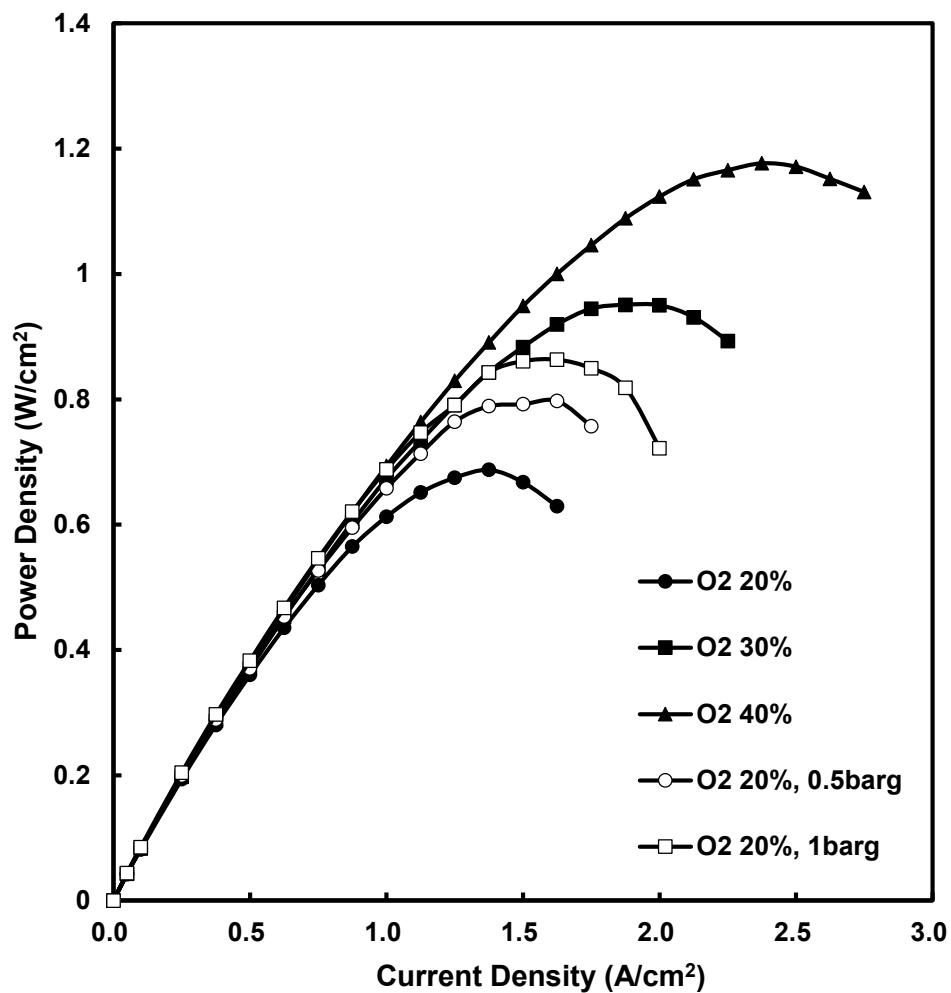
Figure 24 Comparative power density curves of a PEMFC under pressurization and oxygen enrichment conditions
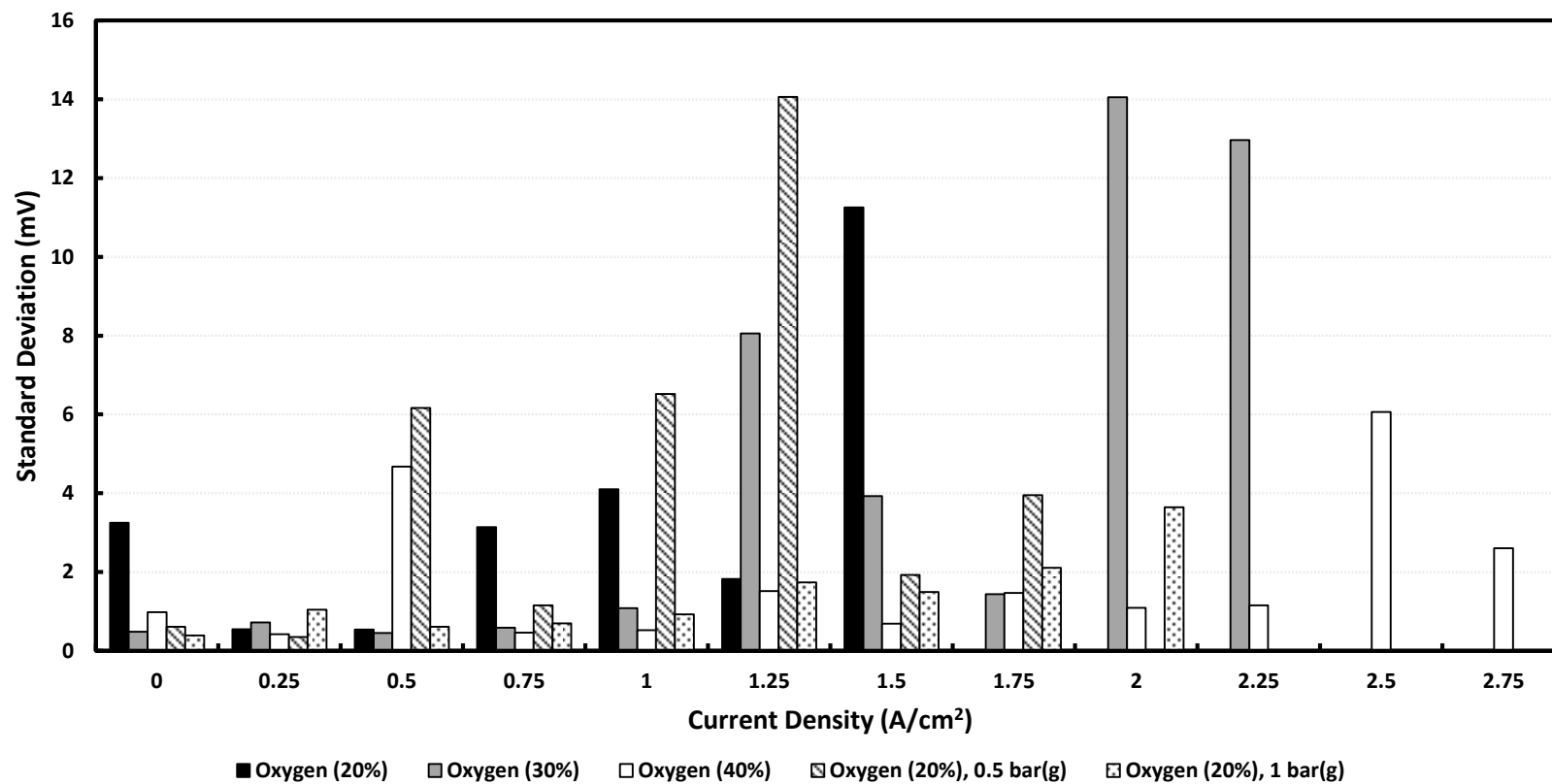
Figure 25 Voltage standard deviation of PEM fuel cell under pressurization and oxygen enrichment conditions
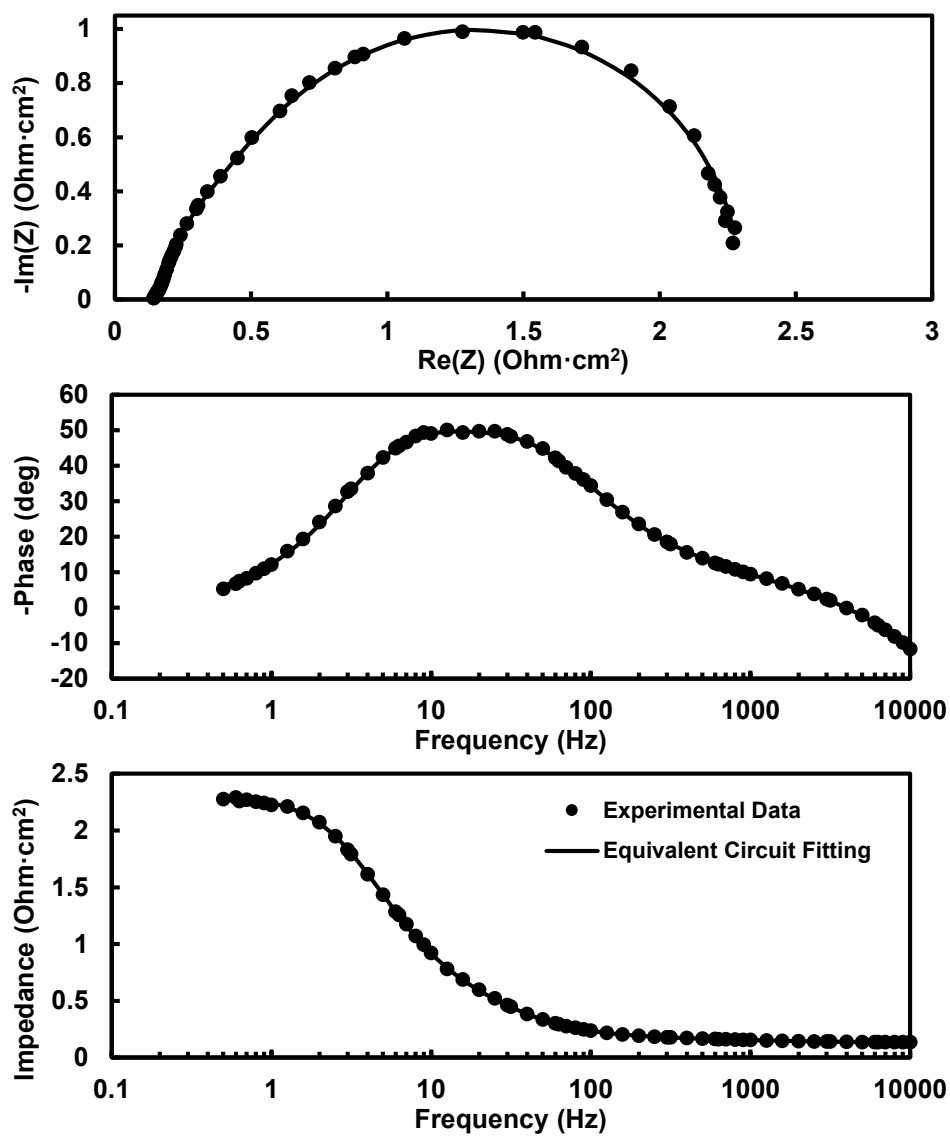
Figure 26 Nyquist and Bode plot at 30A, operating with 20% oxygen
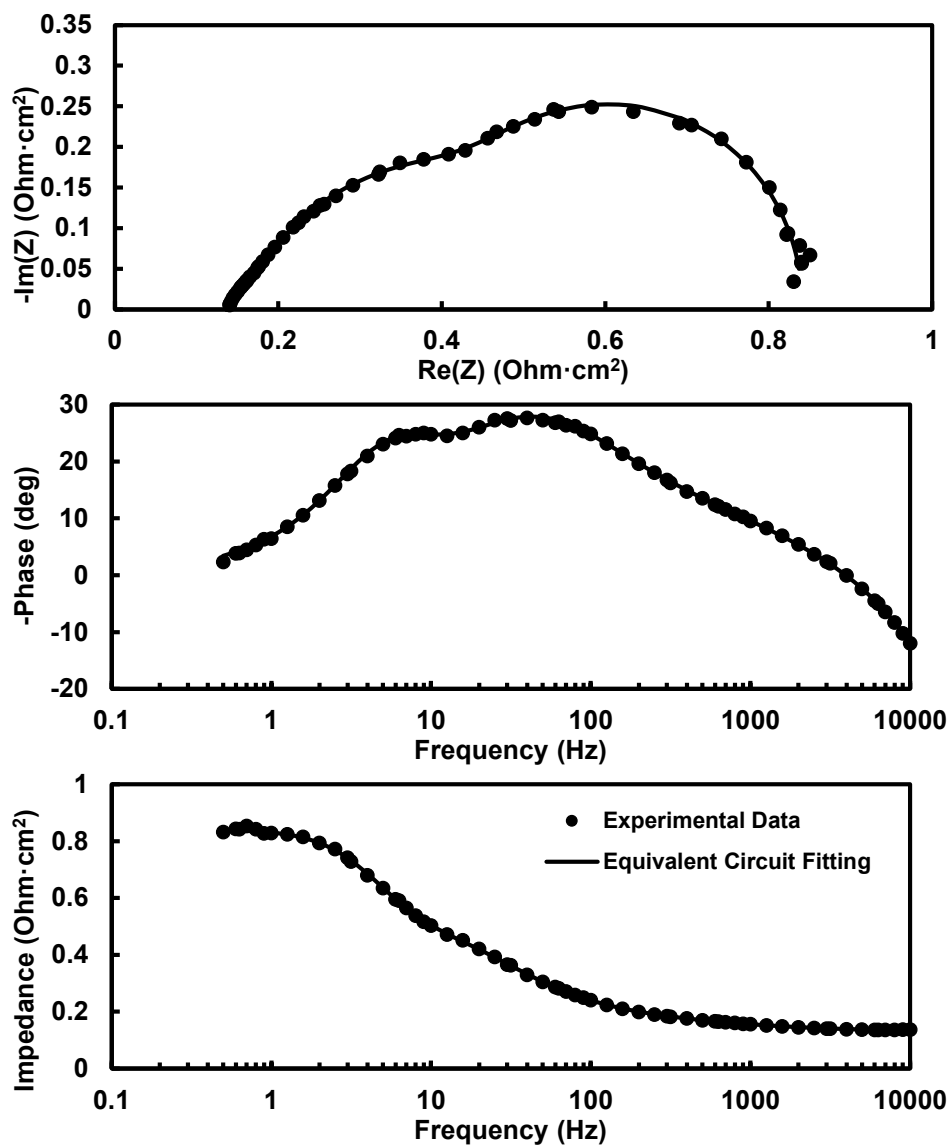
Figure 27 Nyquist and Bode plot at 30A, operating with 30% oxygen
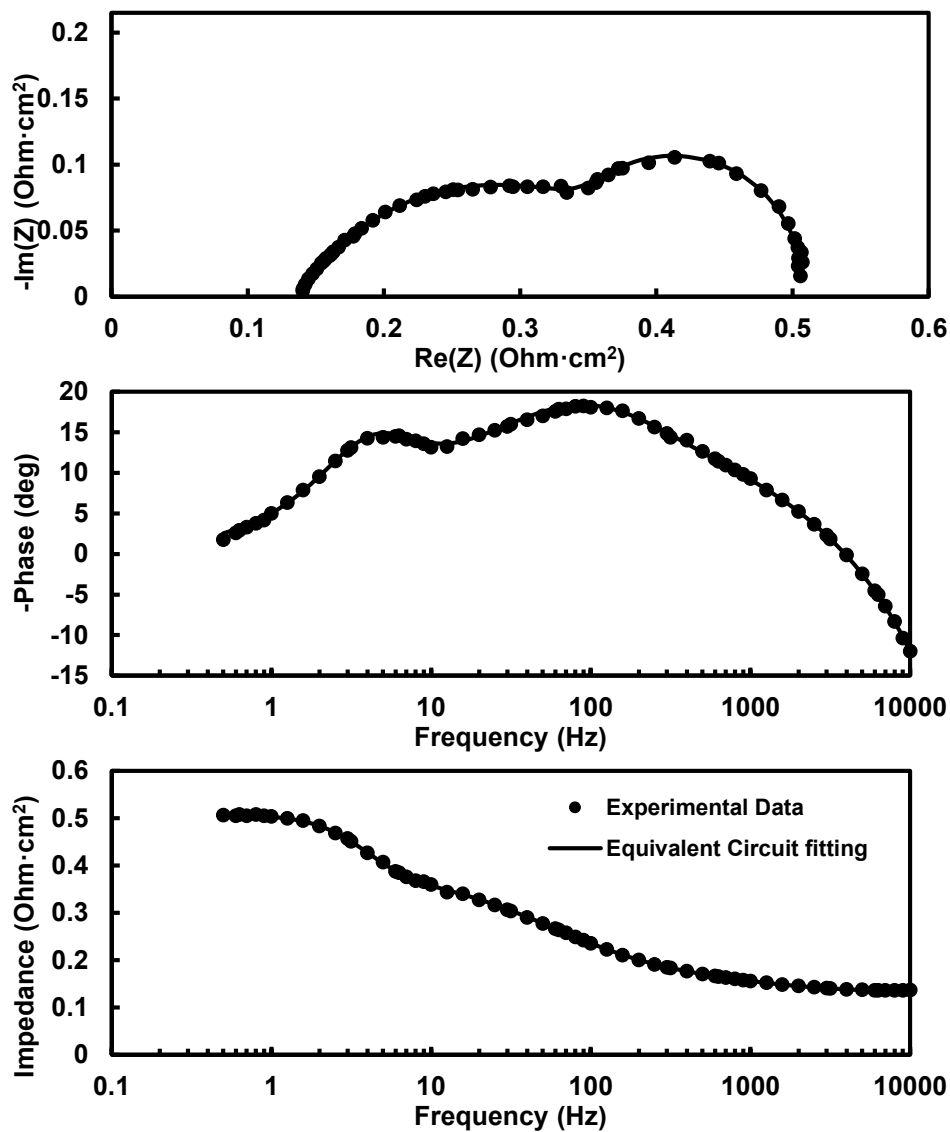
Figure 28 Nyquist and Bode plot at 30A, operating with 40% oxygen
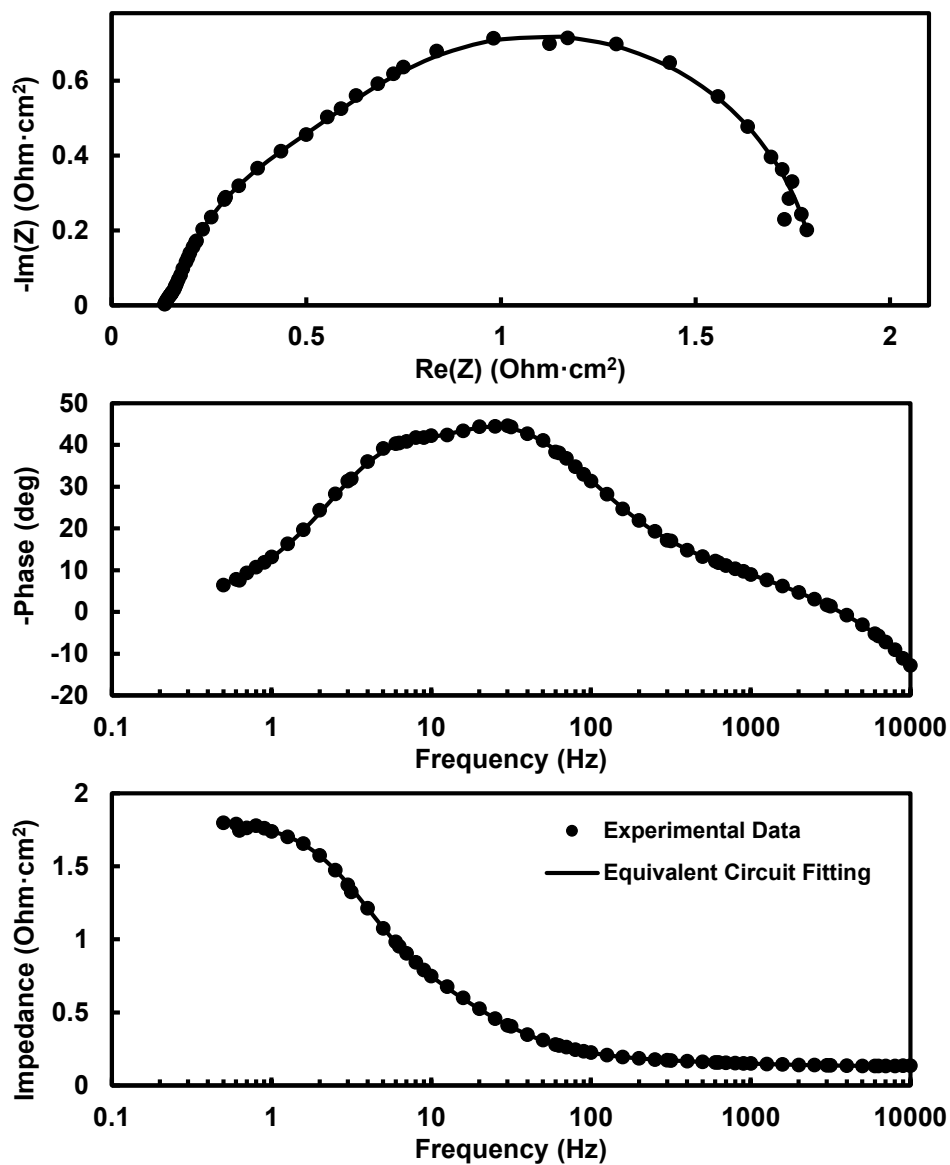
Figure 29 Nyquist and Bode plot at 30A, operating with 20% oxygen and 0.5 bar(g)
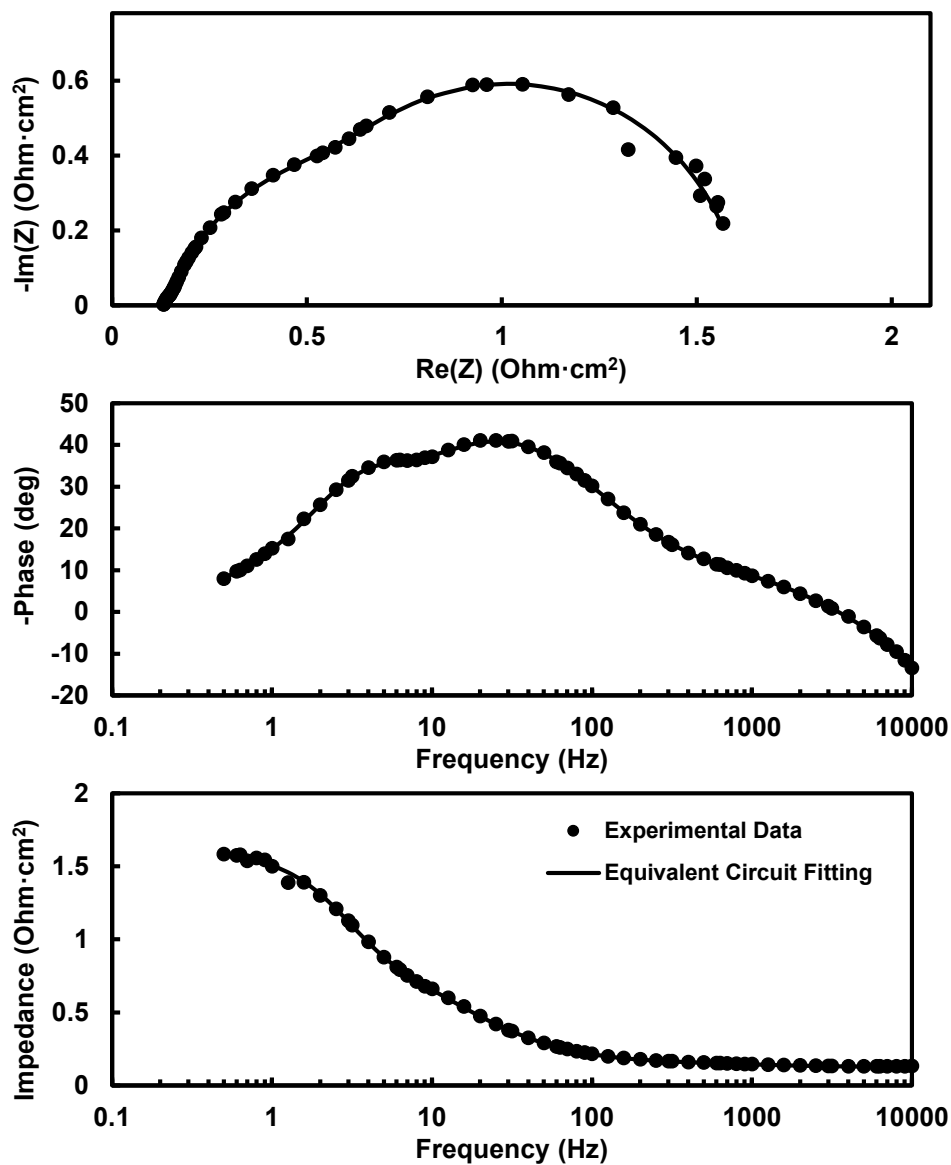
Figure 30 Nyquist and Bode plot at 30A, operating with 20% oxygen and 1 bar(g)
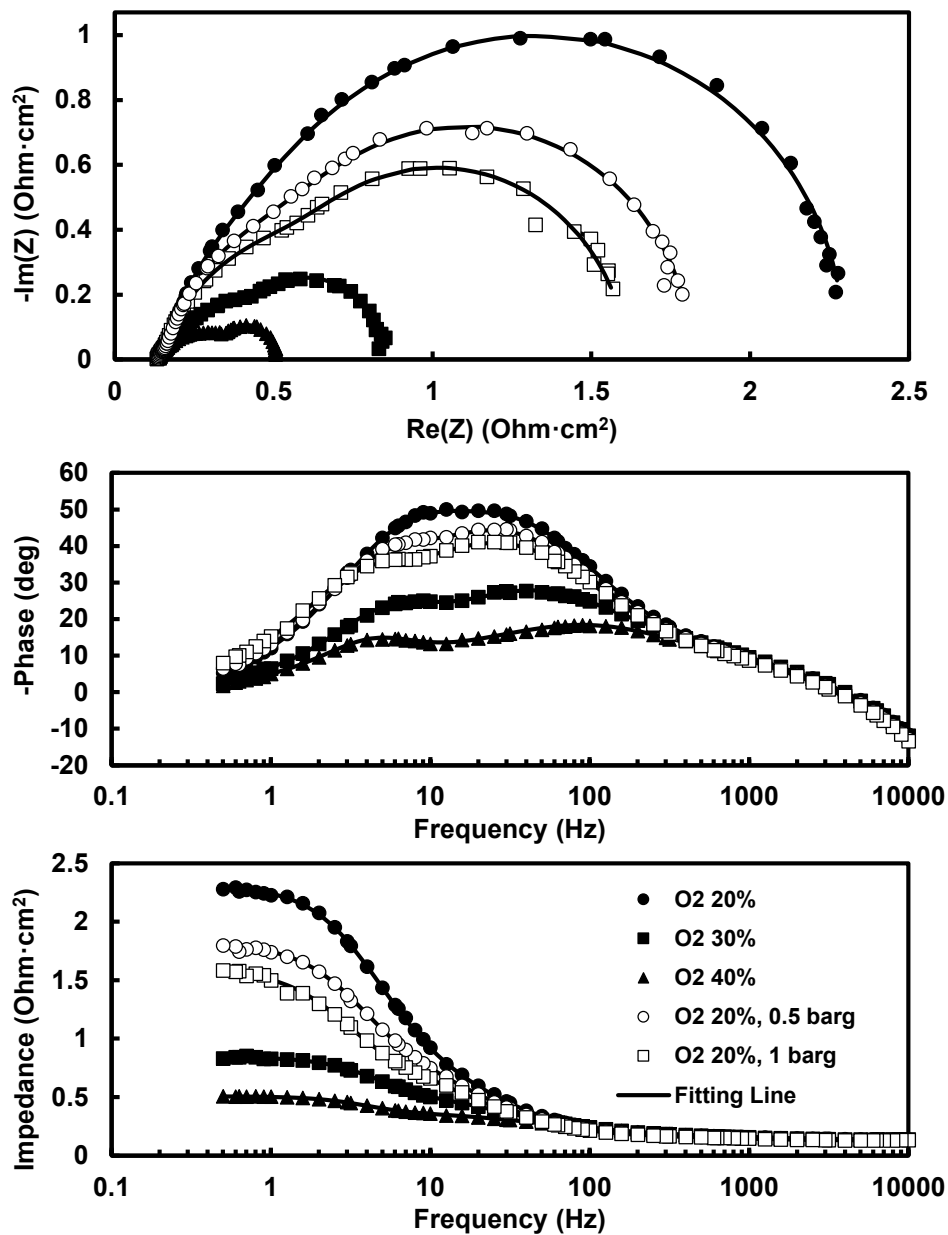
Figure 31 Comparative Nyquist and Bode plots at 30A under pressurization and oxygen enrichment conditions

Table 7 Equivalent circuit parameter values derived from pressurization tests

Oxygen Conc.	Pressure (bar(g))	R_o (mΩ)	$R_{ct,a}$ (mΩ)	$R_{ct,c}$ (mΩ)	R_{Zw} (mΩ)	T_{Zw}	P_{Zw}	$T_{CPE,a}$	$P_{CPE,a}$	$T_{CPE,c}$	$P_{CPE,c}$	L (mH)	$\chi 2$ (-)
20%	0	2.559	1.485	10.993	30.884	0.063	0.506	0.006	0.599	0.001	1.035	1.17E-05	1.38E-03
30%	0	2.530	1.738	5.927	6.647	0.069	0.559	0.007	0.591	0.001	0.938	1.18E-05	9.43E-04
40%	0	2.593	0.648	4.025	2.932	0.084	0.583	0.002	0.746	0.002	0.807	1.15E-05	2.25E-04
20%	0.5	2.539	0.909	15.361	17.511	0.075	0.550	0.003	0.712	0.001	0.947	1.16E-05	2.16E-03
20%	1	2.525	0.488	15.978	13.453	0.096	0.577	0.001	0.885	0.002	0.873	1.12E-05	5.00E-03

2.3.3. Effect of stoichiometric ratio (SR) under varying oxygen concentration.

Altering the oxygen concentration inevitably affects the flow rate of the reactant gas, provided that SR remains constant. Flow rate reduction has both beneficial and detrimental effects. While it diminishes the air supply system workload due to a lower pressure drop, it negatively impacts the water removal from the channels, as the reduced gas velocity and pressure drop cause challenges in water droplet removal from the channel.

Understanding the interplay of cathode SR and cell performance under varying oxygen concentrations is critical when integrating an oxygen concentrator with a PEM fuel cell. This relationship can inform suitable cathode flow rate settings. **Figure 32** to **Figure 37** depict the cell voltage and power density response according to the current density under different SRs and oxygen concentration feeds.

The detrimental impact of reducing the SR lessens as the feed gas oxygen concentration increases. In the air case, the maximum power density fell by 58.3% (from 0.732 to 0.305 W/cm^2), where the SR decreased from 2.0 to 1.1. In contrast, the pure oxygen case only demonstrated a 16.3% decrease (from 1.840 to 1.539 W/cm^2) under similar conditions.

Interestingly, this phenomenon occurs despite a higher oxygen concentration implying a reduced flow rate, which directly impacts the water removal process. However, the liquid water within the GDL, MPL, and catalyst layer is transported due to the capillary pressure gradient. This mechanism suggests that mass transport hindrance is limited to the channel and gas diffusion layer surface despite the significant decrease in flow rate. A parallel serpentine bipolar plate is effective under such conditions because it quickly expels liquid water if a water droplet obstructs the channel. Furthermore, it provides a relatively stable operation

and dispersion of the channel if blockages occur. One potential explanation for the higher oxygen concentration facilitating operation at higher current densities, even at low SRs, is that the higher oxygen concentration buys time when liquid droplets temporarily hinder oxygen transport.

Determining an optimal SR for each oxygen concentration is challenging because SR influences the reduction in axillary power consumption from the reduced SR value and the overall performance deterioration of the cell. Therefore, to effectively capture the interaction between flow rate and feed gas oxygen concentration, the utilization of a suitable PEM fuel cell model is necessary. This model, which we detail in a later chapter, will serve as a tool for further research and application in this domain.
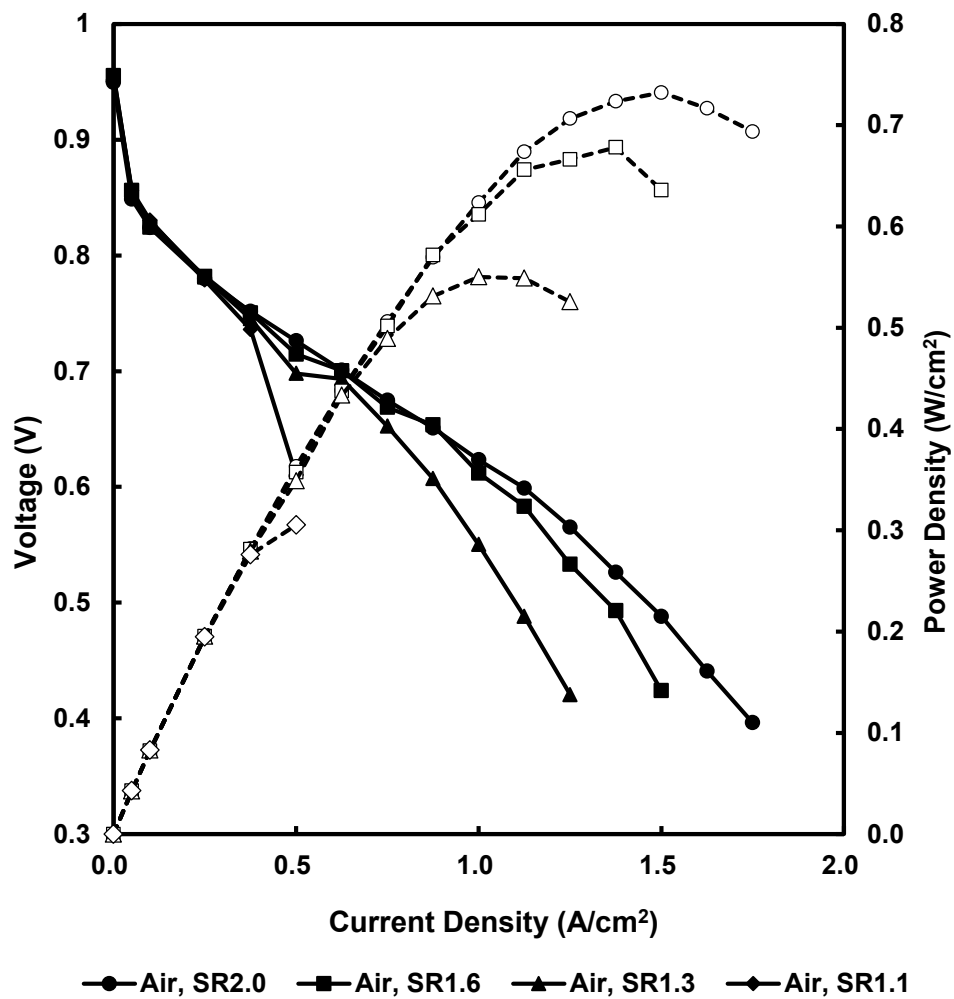
Figure 32 Effect of cathode stoichiometric ratio on PEMFC using air
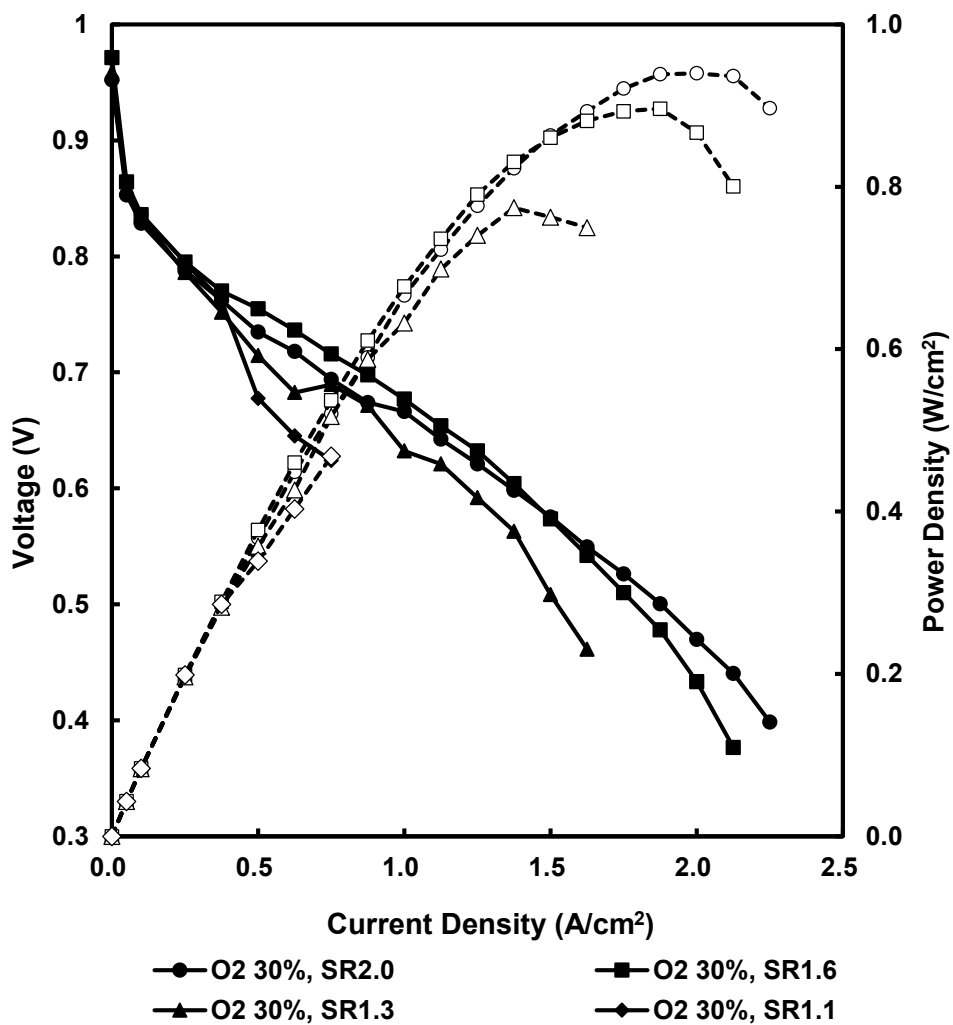
Figure 33 Effect of cathode stoichiometric ratio on PEMFC using 30% oxygen concentration feed
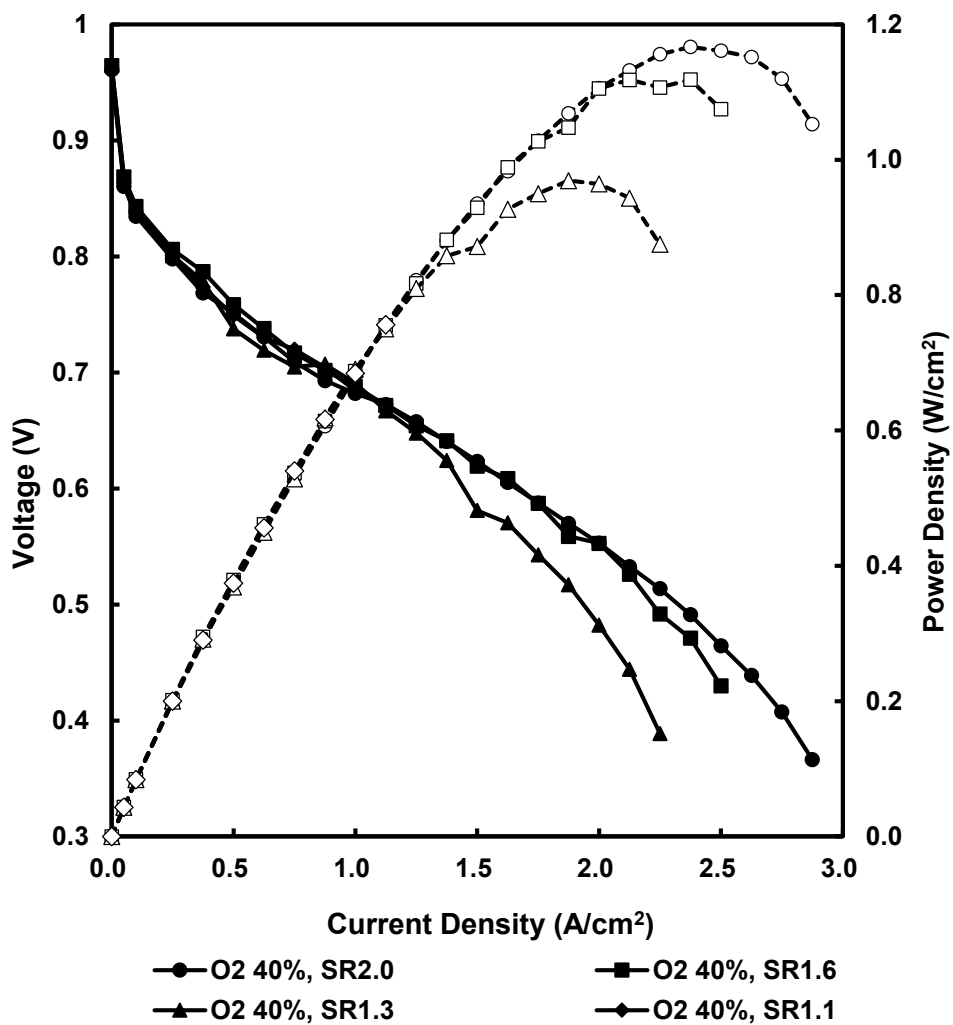
Figure 34 Effect of cathode stoichiometric ratio on PEMFC using 40% oxygen concentration feed
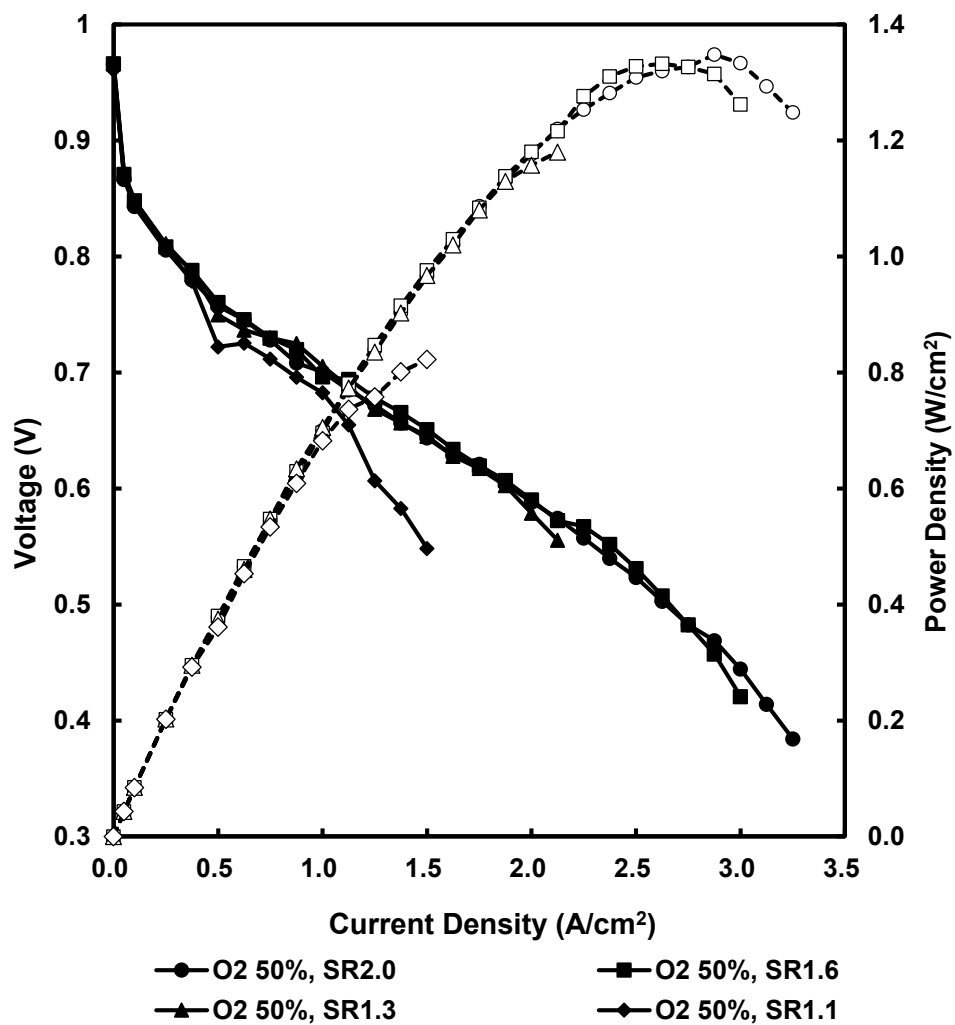
Figure 35 Effect of cathode stoichiometric ratio on PEMFC using 50% oxygen concentration feed
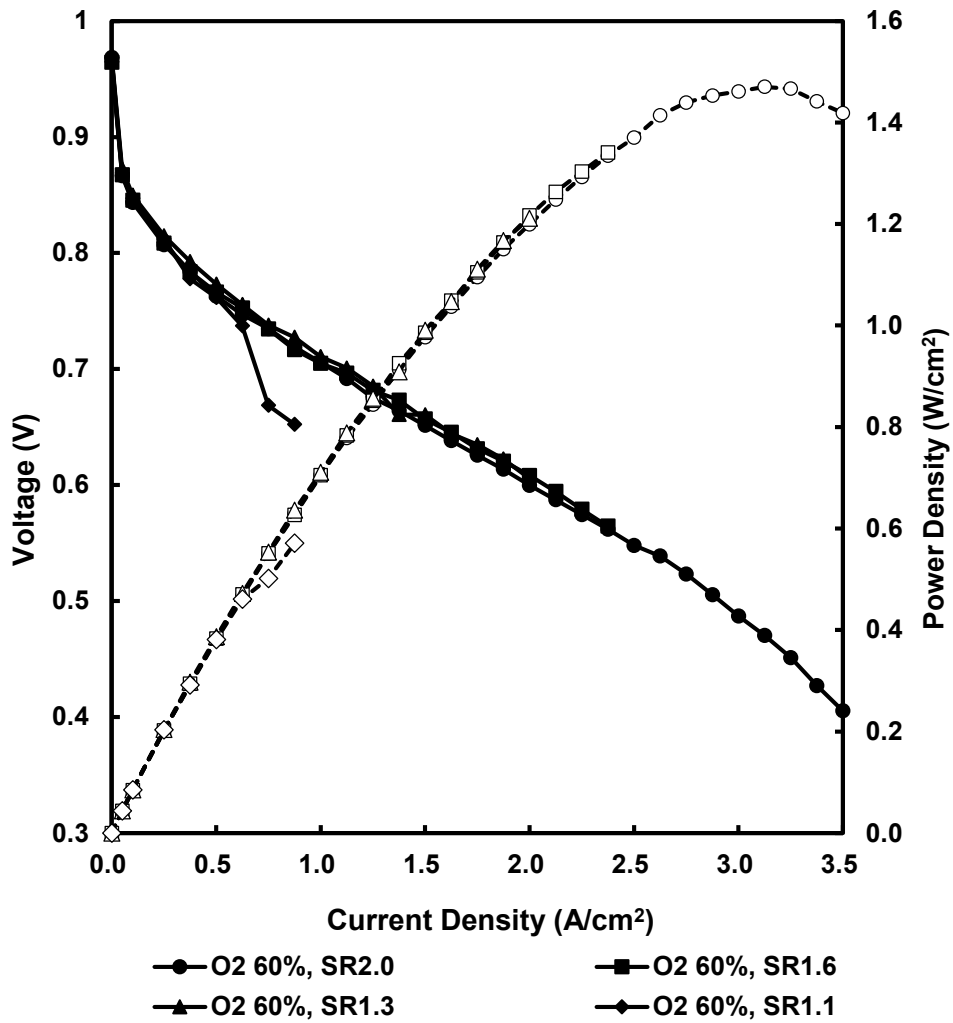
Figure 36 Effect of cathode stoichiometric ratio on PEM fuel cell using 60% oxygen concentration feed
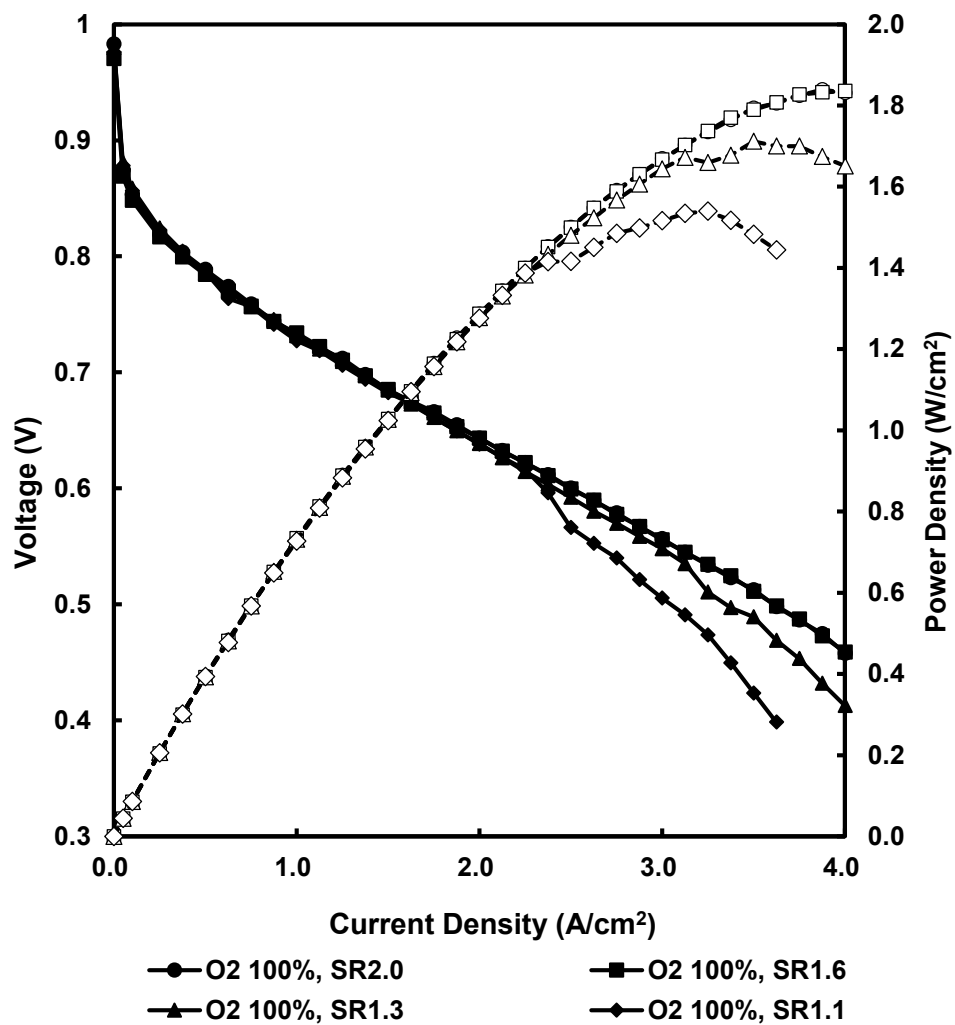
Figure 37 Effect of cathode stoichiometric ratio on PEM fuel cell using pure oxygen

2.4. Summary

In this chapter, we explored a PEM fuel cell performance under various oxygen concentrations. The enhanced oxygen concentration resulted in an elevated OCV and peak power density due to decreased mass transport limitations and improved kinetics. We also juxtaposed the performance improvement resulting from oxygen enrichment with that derived from the pressurization of the cell. Despite pressurization reducing the activation overvoltage and enhancing mass transport, its impact fell significantly short compared to oxygen enrichment. Consequently, we identified oxygen enrichment as superior to optimizing cell performance without necessitating cell modification.

We further examined the influence of the SR to ascertain an appropriate flow rate for oxygen-enriched streams. The complexity tied to the reduction in auxiliary power consumption from a lower SR and the peak power deterioration linked to a decreased SR necessitated the development of a dedicated PEM fuel cell model. This model will be invaluable for identifying the optimal SR value. Despite these challenges, our experimental results recommend an SR higher than 1.3– preferably exceeding 1.6– given that it does not exhibit a rapid voltage drop triggered by flooding in the channels. Additionally, our findings favor using parallel serpentine channels, which facilitate water expulsion even at lower flowrate.

Chapter 3. Oxygen Concentrator

3.1. Introduction

In the continuous pursuit of improving the efficiency of the PEM fuel cell systems, this chapter delves into developing a small-scale oxygen concentrator. The underlying premise of this initiative is to leverage an oxygen concentrator's ability to intake ambient air, selectively separate nitrogen from the air, and supply an oxygen-enriched stream. This oxygen-enriched feed can potentially augment the power output of the PEM fuel cell system.

Nevertheless, the incorporation of an oxygen concentrator comes with challenges. Paramount among them is the additional energy consumption attributed to the concentrator, which affects the overall system's efficiency. Thus, striking a delicate balance between the PEM fuel cell's power augmentation, courtesy of the oxygen-enrich stream, and the energy overhead associated with the oxygen concentrator is vital.

This chapter begins with a brief overview of various methods for oxygen enrichment. Focusing on PPSA technology, we delve into the design and construction of an oxygen concentrator. Further, the performance of the developed concentrator is appraised by measuring critical parameters like the flow rate and the purity of the oxygen-enriched stream. We also evaluate the impact of cycling timing on the parameters mentioned above.

Through a rigorous examination, this chapter offers an insightful understanding of

the feasibility and implications of integrating the developed oxygen concentrator with the PEM fuel cell system, a detailed exploration of which is undertaken in Chapter 5. This knowledge is valuable to the collective understanding of PEM fuel cell system efficiency and opens doors to future investigations in this area.

3.2. Experimental Setup

3.2.1. Selection of oxygen separation method

Several techniques on extracting oxygen from air exist, each with distinct advantages and limitations. These technologies include pressure swing adsorption (PSA), temperature swing adsorption (TSA), polymer membrane, cryogenic distillation, and ion transport membrane, as summarized in **Table 8**.

Temperature swing is an alternative adsorption technology for generating oxygen-enriched gas. In TSA, the adsorbent materials are selectively designed to adsorb nitrogen at lower temperatures and release it at elevated temperatures, enabling separation based on temperature changes instead of pressure variations (**Figure 38**). TSA shares similarities with PSA, but it demands higher regeneration temperatures, leading to increased energy consumption and longer cycle times. Thus, PSA often finds favor in small to medium-scale applications where low energy consumption and ease of operation are prioritized.

Cryogenic distillation, a well-established technique for producing oxygen, nitrogen, and argon, uses the principles of fractional distillation under low temperature and pressure conditions to separate air components. State-of-the-art cryogenic separation units boast an impressive oxygen purity of up to 99.5% by volume and an oxygen recovery rate of 97.85%. However, the technique suffers from substantial energy consumption and lengthy startup times, which can pose feasibility issues for specific applications.

Polymeric membranes are another technology used for oxygen enrichment. These leverage the differing diffusion rates of oxygen and nitrogen across a semi-permeable membrane. With quick startup times, these membranes are widely

employed in small-scale applications. However, they hit a purity ceiling for the enriched gas at around 50%, and commercially available membrane modules can withstand maximum temperatures only up to 65°C, rendering them unsuitable for many industrial applications. Even though it has the advantage of having no moving parts, membrane separation is generally less efficient compared to PSA. While polymeric membranes find use in some small-scale scenarios, they fall short as a practical option for large-scale oxygen enrichment.

Ion transport membranes use a solid inorganic oxide ceramic material that allows the selective transport of ions (such as oxygen or hydrogen) while blocking other gases. Ion transport is instigated by either an applied voltage or partial pressure differences of the molecules. Although these membranes can potentially produce high-purity oxygen, they demand high-temperature operations (800-1,000°C), making them suitable mainly for high-temperature processes like syngas production. Additionally, the high-temperature operation and potential for material degradation undermine the commercial viability of this technology for oxygen enrichment applications.

In conclusion, compared to the alternative separation technologies, PSA offers an optimal blend of operational simplicity, energy efficiency, and high-purity oxygen output. Its promises extend to both small-to-medium-scale applications and larger industrial operations. While other methods like TSA, cryogenic distillation, and membrane technologies bring specific merits, PSA stands out as a superior solution for oxygen enrichment due to its performance and adaptability. Hence, the PSA separation method was selected to design a small-scale oxygen concentrator for a PEM fuel cell.

Table 8 Oxygen Separation Technologies, modified from [32]

Separation Technology	Maturity	Economic Range (sTPD)	Purity limit (Vol.%)	Start-up time
Cryogenic	mature	>20	99+	hours
Adsorption	semi-mature	<150	95+	minutes
Polymeric Membrane	semi-mature	<20	*50	minutes
Ion Transport Membrane	developing	undetermined	99+	hours
Chemical	developing	undetermined	99+	hours

* Values updated
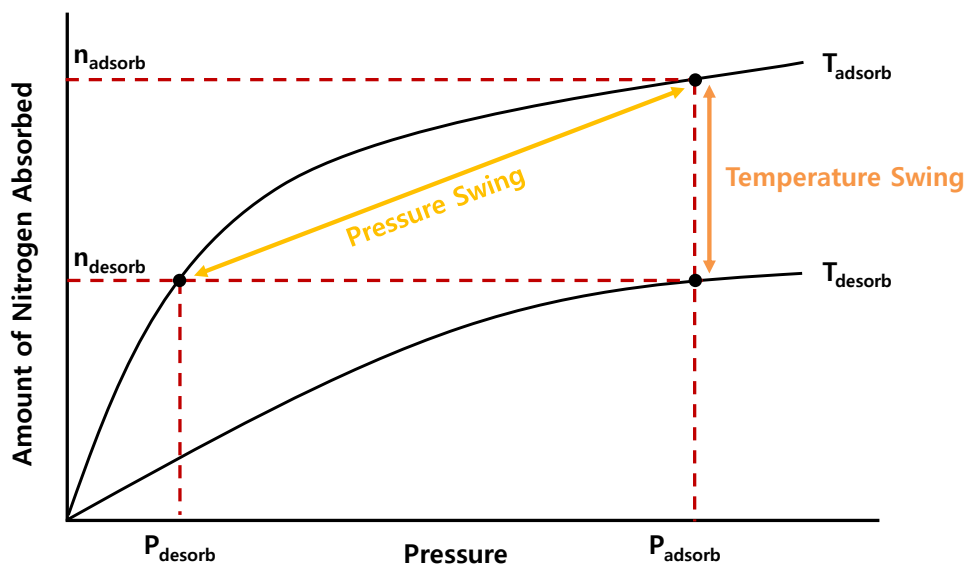
Figure 38 An example of adsorption isotherms, highlighting the fundamental principle of PSA and TSA.

3.2.2. Selection of PSA cycle for PEM fuel cells.

In Chapter 1, a review of the most commonly used PSA cycles was presented, and the selection process for the prototype design of the oxygen concentrator was discussed. The two-bed PSA cycle was chosen as the most appropriate option for this study due to its simplicity and ability to continuously supply oxygen-enriched gas by alternating between the two beds. This cycle offers a more straightforward design, making it easier to construct and maintain, which is beneficial for a prototype that aims to demonstrate the feasibility of the technology. An air compressor and valves are required to build the oxygen concentrator using the selected PSA cycle. The air compressor provides the necessary pressure to force the air through the adsorbent beds, while the valves control the flow of air and product gas in and out of the beds.

Other PSA cycles, such as PVSA and VSA, were considered but ultimately not selected due to their additional requirements. PVSA, for example, requires an air blower, an air compressor, and a vacuum pump. This requirement increases the design's complexity and requires more energy, which is not desirable for a prototype design aimed at demonstrating the feasibility of the technology. Similarly, VSA requires both an air blower and a vacuum pump, which makes the design more complex and increases the system's energy consumption.

3.2.1. Experimental apparatus

The construction of the PSA oxygen concentrator requires careful selection and arrangement of the various components. As shown in **Figure 39**, the system required two adsorbent beds and eight solenoid valves at the core of the oxygen concentrator. A small DC air pump was used to supply air to the adsorbent beds. Alternatively, a building air pipe was controlled via a mass flow controller, offering flexibility in sourcing the initial air feed. A manual backpressure regulator was utilized to fine-tune the adsorption pressure.

Two variants of adsorbents were employed in the experiments: 5A and Li-LSX (HCS13Li-4385, Hanchang, South Korea). The Li-LSX molecular sieve was selected later due to its higher selectivity for nitrogen/oxygen, an essential attribute for efficient oxygen enrichment. Small-size beads with a diameter between 0.43 to 0.85 mm were selected to increase the surface area. However, this resulted in a slightly higher pressure drop.

The two adsorbent vessels, repurposed components previously functioning as moisture traps (MT400-4, Agilent, USA) for an inline gas filter, were cylindrical with a diameter of 3.8 cm and a length of 33 cm. They could endure temperature up to 100 ℃ and pressure up to 17.2 bar. Instead of using a commercially available air compressor with a pressure output of 7.9 bar, a small 24W DC air pump (U-won company, South Korea) was employed in the prototype design to mitigate power consumption.

The solenoid valves (HAD series, Hyoshin Electric Co. Ltd, South Korea) were controlled by a DAQ module (NI 9472, National Instruments, USA) to execute a six-step PSA cycle. Measuring instruments such as an oximeter (GOX 100, Greisinger Germany), a mass flow meter (MWB series, Alicat Scientific, USA), and

power meters (WT130, Yokogawa, Japan) were utilized to measure the oxygen purity, product gas flow rate, and the energy consumption of the oxygen concentrator. As shown in **Figure 40**, the prototype PSA oxygen concentrator was constructed using commonly available components and instruments, which makes it easy to replicate and maintain.

Mass Flow Meter

Back Pressure Regulator

Ⓟ **Buffer Tank**

Ⓟ   Ⓟ

Vessel 1   **Vessel 2**

Vent

**Air Pump /
Mass Flow Controller**

Ⓟ **Pressure Gauge**
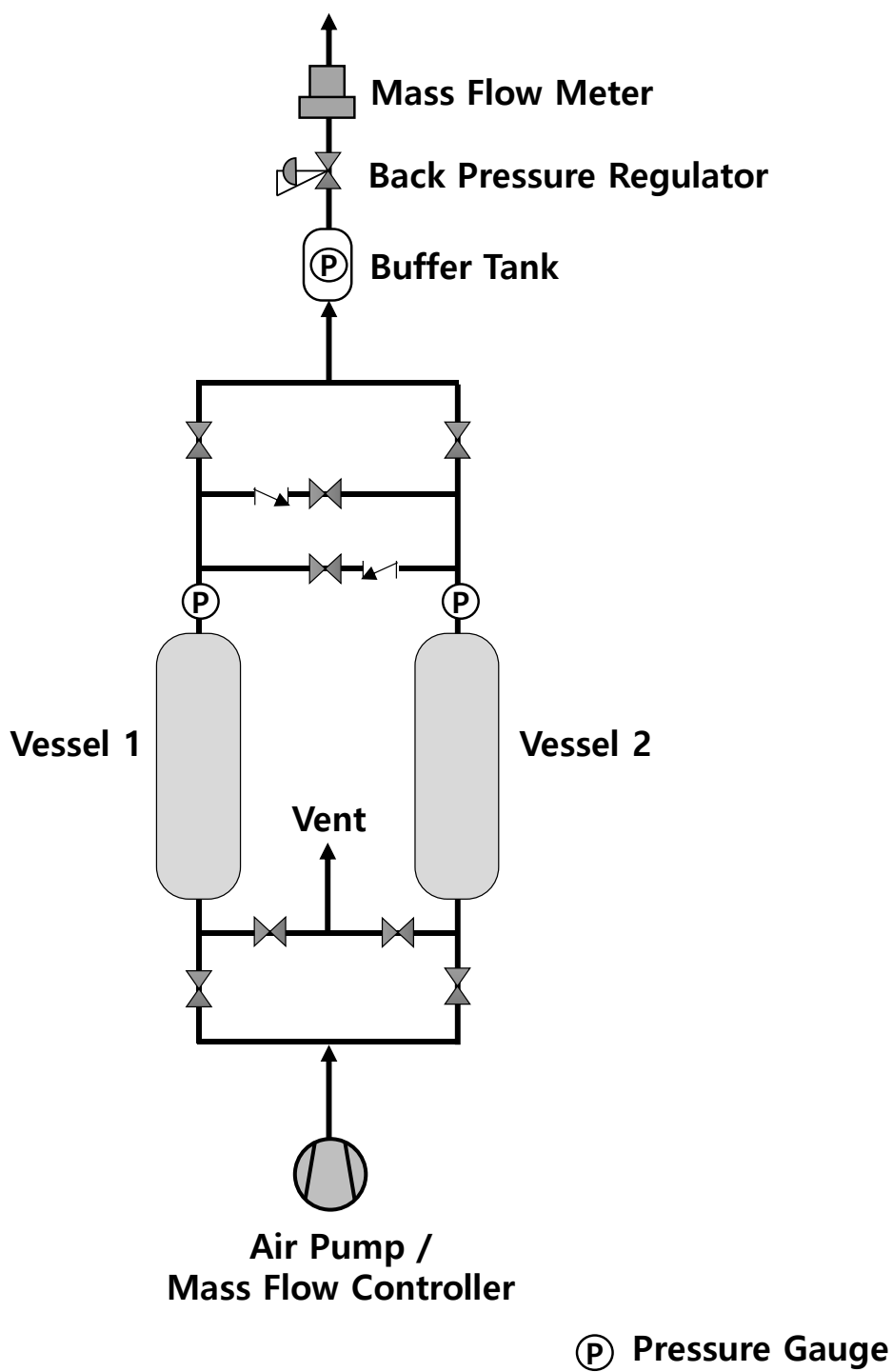
Figure 39 Schematics of oxygen concentrator
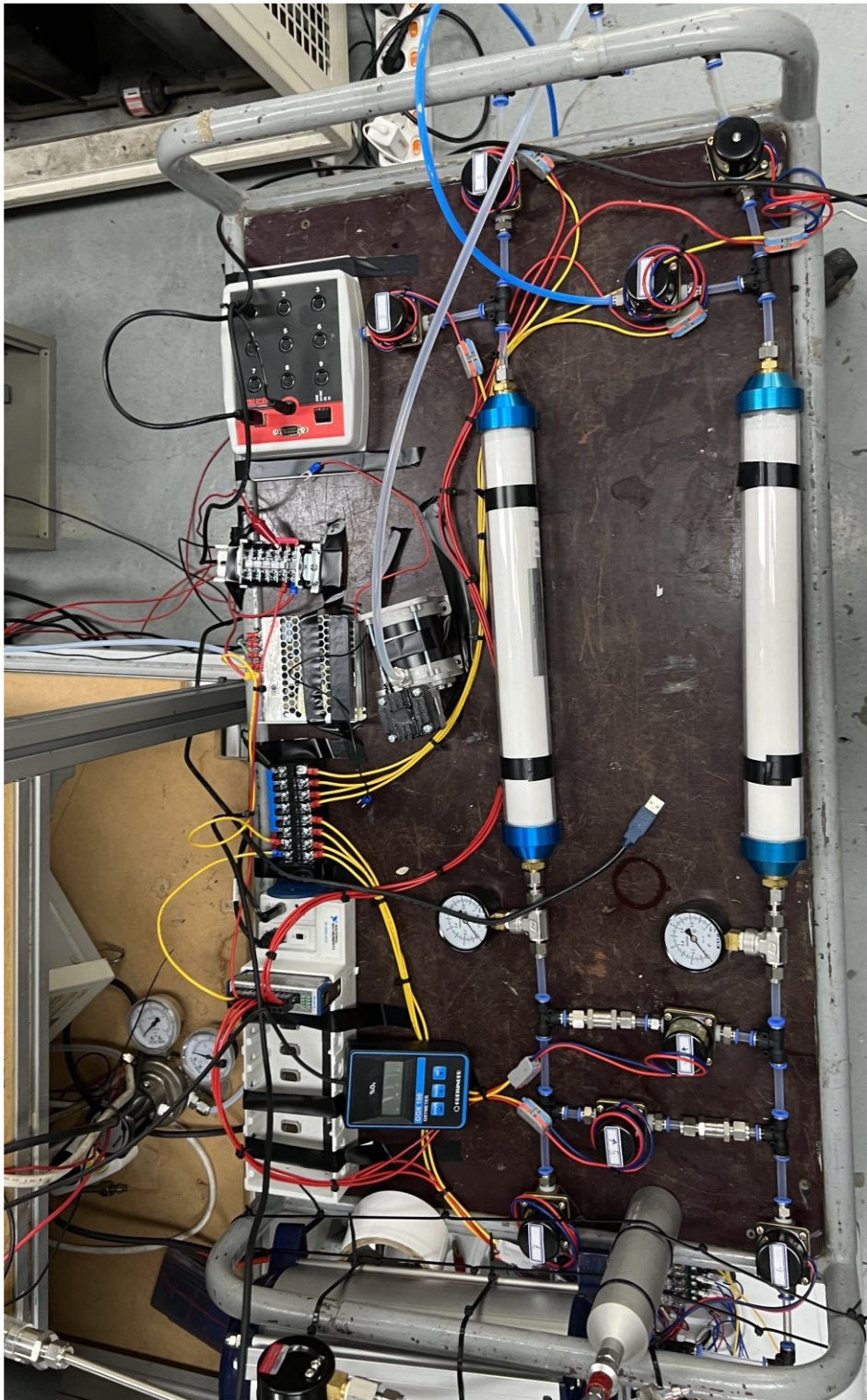
Figure 40 Two-bed PSA oxygen concentrator

3.3. Results and Discussion

3.3.1. Effect of adsorption duration of the oxygen concentrator

The effectiveness of the PSA process is highly contingent on its operating parameters. One such crucial parameter is the adsorption duration, which, when manipulated, profoundly affects the system's performance. For our study, we have varied the adsorption duration while keeping the intake flow rate constant at 6 SLPM using a mass flow controller. Molecular sieve 5A was employed in the adsorbent beds. To pressurize the adsorbent beds, the backpressure regulator was adjusted to limit the gas outflow. Instead of implementing a traditional, distinct pressurization step, we allowed pressurization and adsorption to coincide, thus simplifying the process. Furthermore, the purge was achieved by by-passing the product flow following the adsorption cycle, ensuring readiness of the adsorbent bed for subsequent cycles.

Table 9 encapsulates the impact of adsorption cycle duration on output flow. It is observed that a longer adsorption duration leads to an increase in the maximum pressure inside the adsorption towers, a consequence of allowing a greater amount of gas to be fed over an extended period. The increase in pressure within the adsorbent beds also increases the outlet oxygen concentration. The mechanism behind this observation is the enhanced saturation capacity of the adsorbent at higher pressures, which facilitates superior nitrogen adsorption from the feed gas. For instance, when the adsorption duration increased from 5 to 30 seconds, a corresponding rise in the outlet oxygen concentration from 32.0% to 47.8% was noted. However, there exists an optimum adsorption duration. Beyond this optimal duration, the adsorbent reaches a saturation point where its nitrogen adsorption efficacy decreases. Consequently, any further extension in adsorption duration

becomes counterproductive, causing a reduction in the outlet oxygen concentration. A typical case is represented by our fifth scenario, where an overextended adsorption duration led to a lower oxygen concentration of 29.2%.

The results obtained underline the critical need for optimizing the adsorption duration in the PSA process. Achieving the right balance is essential for ensuring both efficient and effective operation and for attaining the desired oxygen concentration.

Table 9 Effect of adsorption step duration on oxygen concentrator performance

Case	Step Time (second)						Inlet (LPM)	Maximum Pressure (bar(g))		O2 Conc. (%)
	PR	AD	DPE	BD	PU	PPE		Tower 1	Tower 2	
1	5		0.5	5	0.1	0.5		0.1	0.25	32.0
2	10		0.5	10	0.1	0.5		0.7	0.7	36.0
3	20		0.5	20	0.1	0.5	6	1.5	1.5	44.2
4	30		0.5	30	0.1	0.5		1.6	1.65	47.8
5	60		0.5	60	0.1	0.5		1.75	1.8	29.2

PR: Pressurization
AD: Adsorption
DPE: Depressurizing Pressure Equalization
BD: Blowdown
PU: Purge
PPE: Pressurizing Pressure Equalization

3.3.2. Product flow rate variations at different oxygen concentrations

Figure 41 provides a graphical representation of how product flow rate changes for various target oxygen concentrations while keeping the cycle time constant across three cases. The cyclic steady state was obtained or all three cases. In this experiment, the backpressure regulator adjustment was made to impact the product flow rate and oxygen purity.

An inverse relationship was observed between the mean flow rate and the oxygen concentration. When aiming for oxygen purity of 70%, the mean flow rate was 0.44 SLPM. However, as the oxygen purity target lessens to around 60% and 40%, the mean flow rates rise correspondingly to 0.53 to 1.21 SLPM. This reduction in outlet flow rate allows for elevated pressure in the adsorbent tower, bolstering its adsorption capacity and manifesting the reciprocal relationship between oxygen concentration and product flow rate. The flow rate also exhibits variability in all three cases, with the highest fluctuation (standard deviation of 0.63 SLPM) observed at 40% oxygen concentration. It contrasts the lower standard deviations of 0.13 and 0.10 for 60% and 70% oxygen cases.

These outlet flow rate oscillations, detrimental to the operation of a PSA system, can be curtailed by incorporating a suitably sized product buffer tank or a mass flow controller after the buffer tank. By stabilizing the output flowrate, the PSA system can foster operational consistency. To conclude, meticulous system design is required to optimize the PSA oxygen concentrator.

(a)

(b)
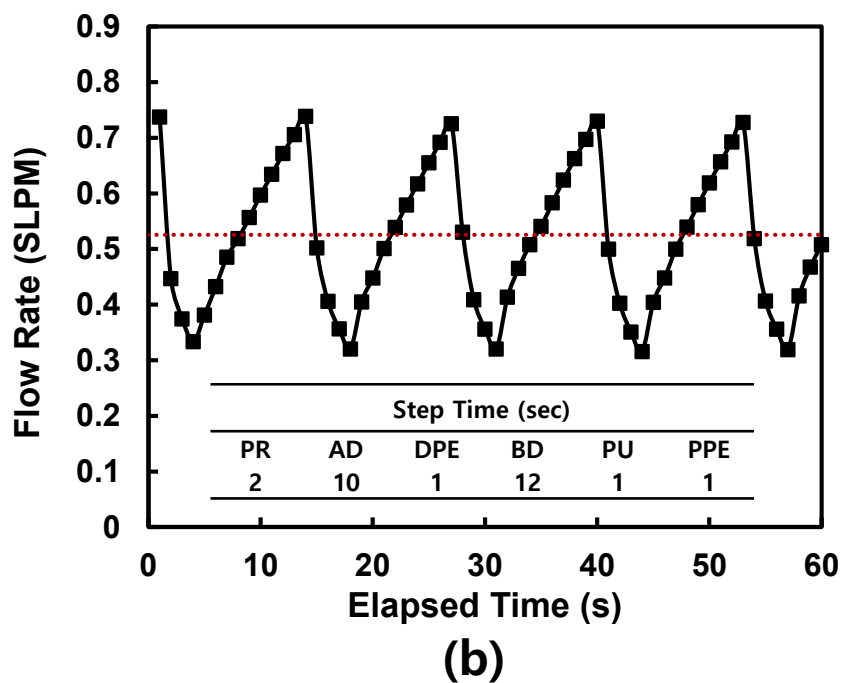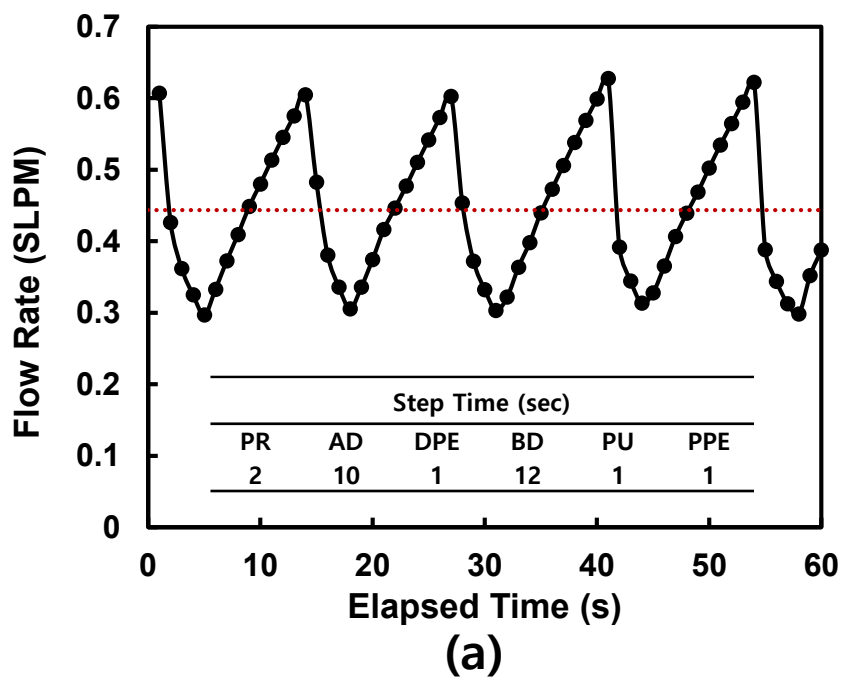
Figure 41 Comparison of PSA product flow rates at different target oxygen concentration rages: (a) 70.1–70.6%, (b) 60.0-61.6%, and (c) 37.1–41.1%

Step Time (sec)					
PR	AD	DPE	BD	PU	PPE
2	10	1	12	1	1

(c)
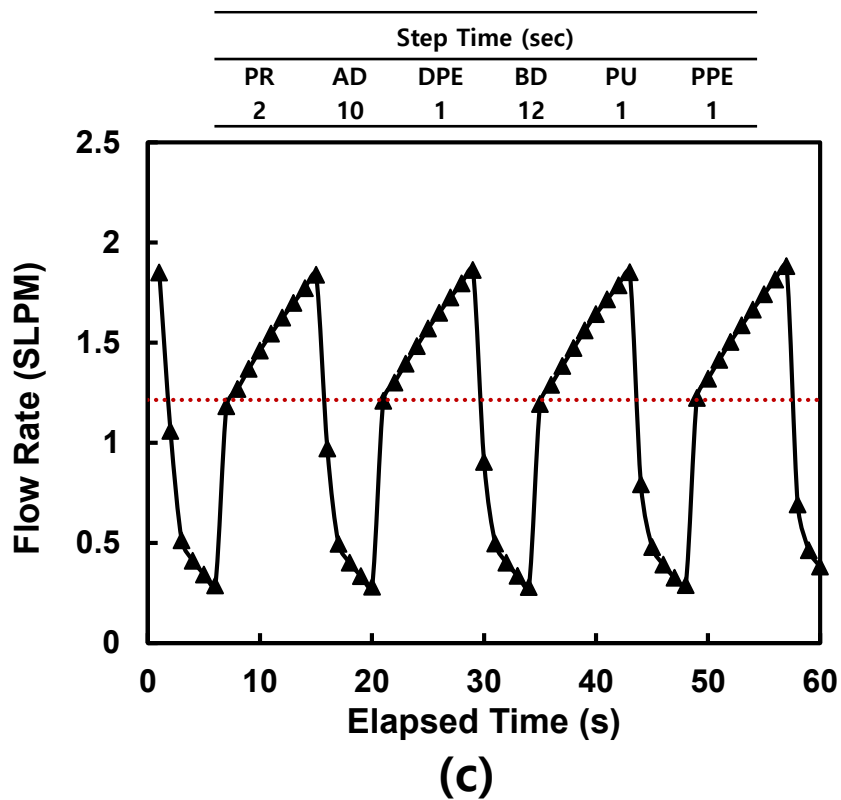
Figure 42 Comparison of PSA product flow rates at different target oxygen concentration rages: (a) 70.1–70.6%, (b) 60.0-61.6%, and (c) 37.1–41.1% (Continued)

3.3.3. Assessing the impact of buffer tank size and pressure drop

This section delineates the effect of the buffer tank size and the effect of the pressure on the performance of the oxygen concentrator. As shown in the previous result, the buffer size was increased to reduce the flow rate fluctuation to observe the butter tank's impact by replacing it with a bigger tank, as shown in **Figure 44(a).** The corresponding result**s** (**Figure 44(b))** indicate that flow rate fluctuations decline significantly when a larger buffer tank is incorporated into the system. This suggested a solution to the previous finding where an increase in flow rate led to an elevation in standard deviation. Specifically, with a larger buffer tank, the standard deviation in flow rate reduces form 0.347 to a mere 0.015, thereby enhancing system stability. Furthermore, a larger buffer tank provides a more stable tank pressure, maintaining a constant 1.8 bar compared to the fluctuating pressure (1.6 to 2.0 bar), i.e., stable oxygen concentration, exhibited by the smaller buffer tank.

On the other hand, an inverse correlation emerges between the buffer tank size and the oxygen purity, with the larger tank causing a drop in oxygen concentration from 7.50-75.4% to 67.3 to 67.5%. This decrease can ascribe to the differential pressure drop invoked by the larger buffer tank, which also incites a change in flow rate from 0.294 to 0.363 LPM. It is noteworthy that adjusting the flow rate can restore the oxygen concentration to its original levels.

Subsequently, the impact of a pressure drop on the performance of the concentrator is examined. As the fabric filter for preventing the loss of the adsorbent is inserted, the metal filter, deemed initially unnecessary, was left from previous vessel usage, which was installed at both ends. **Table 10** compares the concentrator's performance metrics – oxygen concentration and flow rate – with and without the metal filter. The metal filter resulted in an oxygen concentration range of 37.1% to

41.1% and a flow rate of 1.23 SLPM. However, without the metal filter, the system displayed a slightly increased oxygen concentration range of 39.6% to 41.4 % and a higher flow rate of 1.62 SLPM. The introduction of an metal filter caused an undesired increase in pressure drop, highlighting the importance of careful design considerations in achieving an optimized system. The effect of the buffer tank, as well as the system pressure drop warrant careful consideration and optimization in system design and operation.

(a)
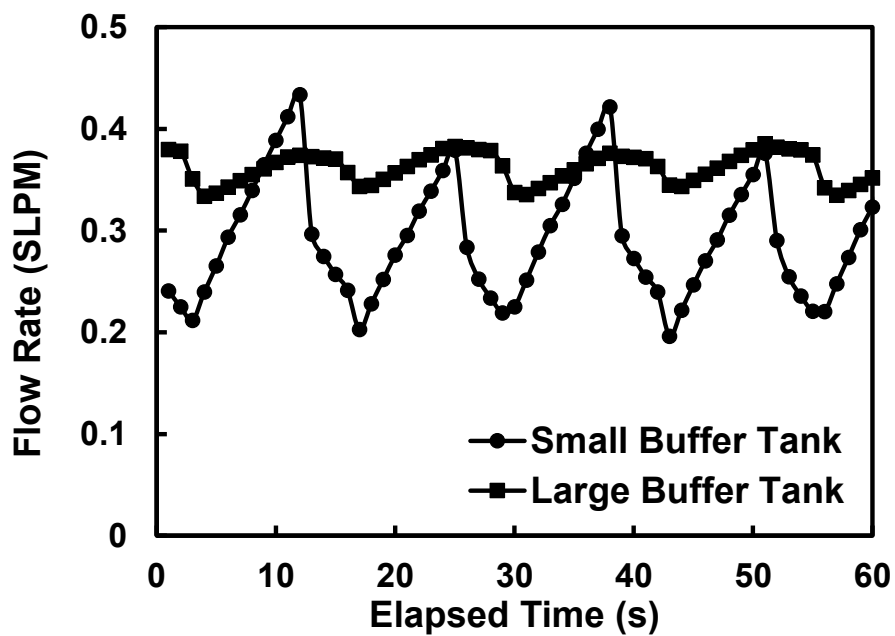
(b)

Figure 43 (a) Two different size of buffer tanks used for oxygen concentrator
(b) Effect of buffer tanks on product flow rate

Table 10 Comparison of oxygen concentration and flow rates in the PSA system with and without the fine filter

With fine filter (Higher pressure drop)		Without fine filter (Lower pressure drop)	
Oxygen conc. (%)	Flow rate (SLPM)	Oxygen conc. (%)	Flow rate (SLPM)
37.1 – 41.1	1.213	39.6 – 41.4	1.620
60.0 – 61.6	0.526	42.6 – 44.5	1.444
70.1 – 70.6	0.444	45.2 – 45.6	1.33

3.3.4. Feasibility Test

The prototype of the newly developed oxygen concentrator was subjected to testing with a 24V DC air pump. The results, illustrated in **Figure 42**, revealed the system's capacity to achieve an oxygen purity of 40% at a flow rate of 1.62 SLPM, without the optimization of design or cycle process parameters.

Remarkably, the oxygen concentrator's flow rate was sufficient to supply 2.27 units of fuel cells. Each of these cells draws 60A at a 1.5 stoichiometric ratio. According to the data in Figure 13, there would be a mere 4% power degradation when the stoichiometric ratio decreased from 2.0 to 1.5.

Through simple calculations, it is evident that 2.27 units of fuel cells utilizing a 1.5 stoichiometric ratio and 40% oxygen as fuel gas could collectively generate 24.47 Watts of power. This surpasses the power consumption of 24 Watts, indicating that the system can operate efficiently.

This feasibility test strongly suggests that an oxygen concentrator, optimized in design and process, could yield a net system surplus. Additionally, as the oxygen concentration increases, a corresponding decrease in the pressure drop from the cell is anticipated. This will potentially result in fewer cells required, thus saving on the costly platinum catalyst.

There are, however, certain challenges, such as the need for an additional air pump and maintaining the oxygen concentrator. Despite these, integrating the oxygen concentration using PSA into the fuel cells is still beneficial from a net power perspective. This advantage is worth noting, despite the potential increases in both maintenance and initial investment costs.

3.4. Summary

In this chapter, we developed a small-scale oxygen concentrator. Firstly, we explore how the design of the cycling timing, such as the adsorption period, affects the performance. The developed oxygen concentrator was assessed to obtain purity and flow rate information. Lastly, we explore the effects of the buffer tank size and the pressure drop in the system. We find that there exists an adsorption duration that yields the highest oxygen concentrator. Deviating from this optimal duration by increasing or decreasing it could decrease performance. Optimizing adsorption duration is critical for achieving desired oxygen concentrators, balancing the system's efficiency and effectiveness. A salient inverse correlation was observed between oxygen concentration and product flow rate. Hence, applying the oxygen concentrator to the PEM fuel cell requires the best combination for the best net power output. Also, a meticulous design, including the pressure drop and buffer tank size, is necessary for an optimized oxygen concentrator when designing a real-application oxygen concentrator. Lastly, the feasibility test of the developed oxygen concentrator was performed using a 24W air pump, which resulted in a diminutive surplus, excluding the power consumption of solenoid valves.

Collectively, these sections emphasize the intricate balance and interplay of various parameters in an oxygen concentrator, stressing the importance of system design optimization for efficient operation.

Chapter 4. Mathematical Modelling

4.1. Introduction

The preceding chapters (2 and 3) provide an experimental analysis centered on the impact of an oxygen concentrator on PEM fuel cells and delve into the performance of a developed small-scale oxygen concentrator. These investigations show the potential of improving PEM fuel cell performance by integrating an oxygen concentration. To proceed further, it is necessary to develop mathematical modes for both the PEM fuel cell and the oxygen concentrator to attain the synergy of these systems. Therefore, this chapter embarks on the development and elucidation of mathematical models, and they are expected to aid in understanding the underlying mechanisms and serve as an invaluable tool for refining the design and operational strategies of integrated PEM fuel cell systems with oxygen concentrators.

4.2. PEM fuel cell model

4.2.1. Model overview and key assumptions

A PEM fuel cell model was developed using the Matlab Simulink® platform. A one-dimensional node for the PEM fuel cell was formulated, focused on the through-plane direction. This model allows node replication and arrangement, capturing the fuel cell's in-plane direction. This creates a quasi-three-dimensional model representation. Instead of introducing the full three-dimensional model, this methodology offers a balanced compromise between computational accuracy and efficiency, effectively capturing the spatial characteristics of the cell in the in-plane direction [33]. Multi-component equations are strategically integrated to facilitate real-time operations under various oxygen concentrations. This ensures accurate reflection of the effects induced by varying oxygen concentrations.

To translate the complex behavior of an actual PEM fuel cell into a manageable computational model, we adopted the following assumptions:

1. Each control volume is denoted by species mole fraction, temperature, and pressure.

2. In-plane diffusion in the gas diffusion layer and the electrolyte membrane is disregarded.

3. Diffusive flux in flow channels is not considered, given that convective flux is the predominant force governing flow within these channels ($Pe=10^{10}$)[8]

4. An equipotential electrode is postulated.

5. Electrochemical reactions are treated as quasi-steady, reflecting their rapid temporal nature in electrochemistry.

6. Liquid water transport along the channel is omitted owing to the intricate

nature of modeling two-phase transport in the gas channel. Notably, this might introduce discrepancies in species concentration distribution and overall fuel cell performance. [34].

7. Any liquid water in the catalyst is assumed to envelope the agglomerates, forming a water-coating layer [35].

8. Agglomerates are located at the catalyst-membrane interface.

9. Transport phenomena occurring within the agglomerates are not factored in the model.

4.2.2. Discretization and model development

Developing a PEM fuel cell model requires its discretization into multiple control volumes to aptly represent the intricate behavior of a cell. This discretization commenced perpendicular to the gas stream and proceeded in the flow direction. This approach effectively mimics mass transport phenomena, including convection, diffusion, and capillary water flux, as illustrated in **Figure 44(a)**.

A standard PEM fuel cell comprises a bipolar plate with channels, gas diffusion layers integrated with a microporous layer, and a membrane-electrode-assembly. Each component had at least one control volume designated to it, ensuring an accurate representation of mass and heat transfer. PEM fuel cell system regulates the stack temperature using coolant flowing through coolant channels. Hence, the fuel cell model was built to include the cooling channels. However, as our actual fuel cell uses the heating poles inserted into the endplates to control the bipolar plate temperature, we have the constant temperature to the bipolar plate, which could streamline the model and contribute to decreased computational time.

Given the disparity in the pore size range between MPLs (approximately

hundred nanometers) and substrate (around hundred micrometers) in GDLs, mass transport phenomena such as diffusion and capillary flux across GDLs requires finer discretization. Hence, eight control volumes were designated for each GDL to mirror the variations in physical properties, as depicted in **Figure 44(b)**. Of these, the substrated was assigned four control volumes, two control volumes for MPLs and two for the MPL penetrated substrate.

Discretization's influence is unmistakably evident along the flow direction, a dimension that mirrors the changing gas compositions due to variables like fuel consumption and product water generation. Opting for more detailed discretization elevates the model's precision. Still, it concurrently amplifies the computational demands – a challenge, especially when the model's design underscores swift calculation. In navigating this balance, we have prudently limited the discretization along the channels.

Each control volume was subjected to energy and species conservation principles, determining local temperatures, mole fractions, and corresponding fluxes. Newton's law of cooling and Fourier's law were instrumental in calculating the heat rate. During molar flux evaluations, the model also leans on the "perfect mixing" premise. For a deeper dive into the conservation equations, readers are direct to Kang's work research [36].

Flow Direction : Fuel

Anode Bipolar Plate

Anode GDL

MEA

Cathode GDL

Cathode Bipolar Plate

Cooling Plate

Oxidant

(a)

Bipolar Plate

Flow Channel

Substrate 1
Substrate 2
Substrate 3
Substrate 4
Substrate 5

MPL 1
MPL 2
MPL 3

Catalyst layer
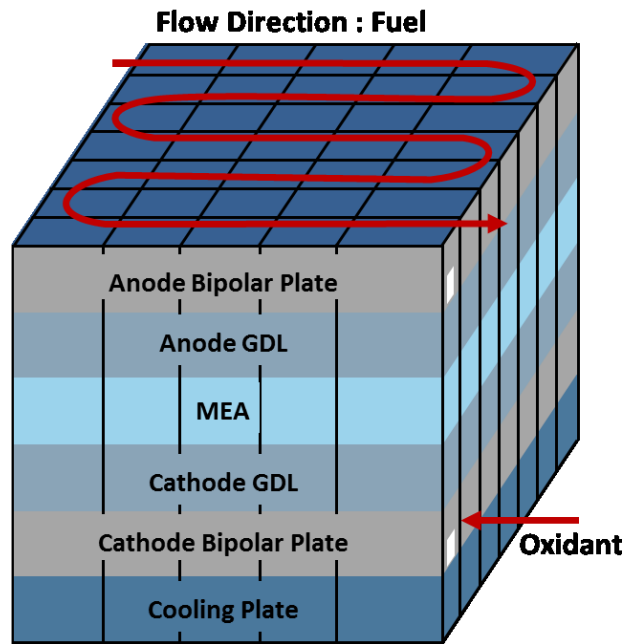
MEA
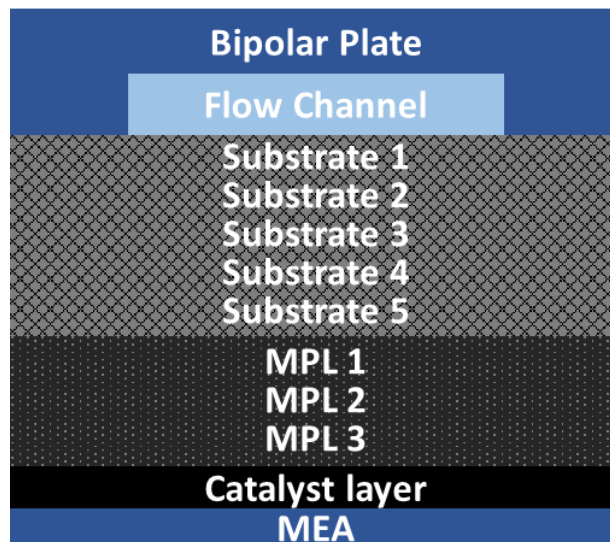
(b)

Figure 44 (a) An example of discretization layout of PEM fuel cell model

(b) Illustration of control volumes in the fuel cell control volumes

4.2.3. Mass transfer in PEM fuel cells

For a proper representation of PEM fuel cell behavior, creating a meticulous model of the gas-phase mass transfer is essential. The integrity of this model directly correlates to the precision in estimating the oxygen transport to the catalyst layer. Typical models adopted constant binary diffusion coefficient values. They sidestepped the influence of gas composition changes on the diffusion coefficient. They also often neglect the Knudsen diffusion and ionomer resistance. This section introduces the equations that cater to these factors, offering a detailed overview of the mass transfer mechanisms within the PEM fuel cell.

Gas diffusion is influenced by temperature, pressure, gas composition, and the medium's properties. Our model's molecular diffusion coefficient was derived from coupling the binary diffusion equations and multicomponent mixture gas equation for each control volume. For components like MPLs and catalyst layers, where the Knudsen diffusion starts, the effective diffusion coefficient was determined via a harmonic average of molecular and Knudsen diffusions. The foundational equations used to predict binary gas diffusion is presented by Fuller et al. [37] :

$$D_{AB}(cm^2/s) = \frac{1.00 \times 10^{-3} T^{1.75} \left(\frac{1}{M_A} + \frac{1}{M_B} \right)^{0.5}}{P \left[(\sum v_A)^{\frac{1}{3}} + (\sum v_B)^{\frac{1}{3}} \right]^2} \qquad (4.1)$$

The unit for temperatures and pressures are in Kevin and atmospheric pressure, respectively, where M is the molar mass of the molecule, and v is the diffusion volume of molecules.

To simulate convective mass transfer between the gas channel and GDL, the following equations were applied [38] :

$$\vec{\Phi}_{conv} = \vec{h}_m A (C_{i,channel} - C_{i,GDL}) \tag{4.2}$$

$$\vec{h}_m = \frac{Sh \cdot \vec{D}_m}{D_h} \tag{4.3}$$

The diffusion length of porous materials hinges on their tortuosity, which, given the randomness of carbon fiber stacking, can be challenging to quantify. However, the Bruggeman correlation offers a robust method to gauge tortuosity's effect [39]:

$$\vec{D}_m^{eff} = [\varepsilon(1-s)]^{1.5} \vec{D}_m^g \tag{4.4}$$

The diffusion mass transfer rate, based on Darcy's equation, is:

$$\vec{\Phi}_{diff} = \frac{\vec{D}_m^{eff} A}{t} (C_{i+1} - C_i) \tag{4.5}$$

Efficient liquid water management in PEM fuel cells is crucial to ensuring optimal performance. The formation of liquid water can clog catalyst layer pores, impairing oxygen transfer and causing a dip in cell voltage. Conversely, when liquid water is proximate to the membrane, it enhances membrane conductivity, curtailing the ohmic voltages. This dual nature underscores the importance of meticulous modeling of liquid water transfer. Our approach leverages the multiphase mixture model [40], building on Kang's foundational work [36], but we have integrated several refinements for more accurate liquid water flux prediction. The relative permeability model was carefully selected to fit the diffusion medium better [41]

$$k_{rl} = s^{2.16}, \; k_{rg} = (1-s)^{2.16} \qquad (4.6)$$

While the widely accepted Kozeny-Carman relation [40]factors in pore diameter and porosity for permeability computation, it falls short for fibrous materials like gas diffusion layer substrates, especially under transition flow conditions. Instead, we have adopted a tailored equation for fibrous porous media crafted by Jeong et al.[42]

$$\frac{K}{D_{CF}^2} = \exp\left\{ C_1 \ln\left(\frac{\varepsilon^{\frac{11}{3}}}{(1-\varepsilon)^2} \right) - C_2 \right\} \qquad (4.7)$$

$$\begin{cases} C_1 = 0.7128 - 0.4953 K_n \\ C_2 = 1.974 - 4.2892 \end{cases}$$

Adjusting for the water diffusion through the membrane is also paramount. While the initial model was designed for the Nafion™ membrane, our study employs membranes from Vinatech. Intriguingly, a 2007 study by Ye and Yang[43] found the Gore-Select membrane's water diffusion coefficient to be roughly half that of Nafion. Thus for our simulation, the membrane is postulated to contain 50% Nafion materials, as Vinatech uses a reinforced membrane like Gore's.

$$D_{w,eff} = 0.5 D_w \qquad (4.8)$$

4.2.4. Catalyst layer and Agglomerate model

PEM fuel cell models conventionally simplify the catalyst layer, presuming its diminutive thickness, thus rendering its intricate structure negligible. This traditional oversimplification is now challenged by experimental observations indicating that the resistance to oxygen transport within the catalyst layer constitutes approximately 15% of the total dry transport resistance[44]. Such empirical revelations have necessitated the introduction of a porous electrode model, which more adequately captures the agglomerate structure pivotal to the oxygen transport phenomena. However, the updated catalyst model assumes uniform concentration and potential across the entire catalyst layer [38]. **Figure 45** provides a graphical elucidation of the model where an ionomer film wholly encompasses the agglomerate surface. Any liquid water localized within this layer is hypothesized to morph into water films, coalescing around the ionomers. This hypothesis can be mathematically delineated as follows:

$$\delta_w = \sqrt[3]{(r_{agg} + \delta_{ion})^3 + \frac{3s\varepsilon_{cl}}{4\pi N_{agg}}} - (r_{agg} + \delta_{ion}) \qquad (4.9)$$

Oxygen molecules transported to the reaction site are obligated to experience either a single of multiple layers. The inherent phasic nature of this transport induces discrepancies in molar concentration at phase boundaries. To model these concentration variances, Henry's constants, calibrated via experimental data [35], are employed:

$$H_{O_2}(Pa.m^3.mol^{-1}) = 0.11552 \, exp\left(14.1 + 0.0302\lambda - \frac{666}{T}\right) \qquad (4.10)$$

The liquid-phase diffusive behavior of oxygen molecules is ascertained using the Stokes-Einstein equation:

$$D_{O_2-H_2O} = \frac{k_B T}{6\pi\mu R_o}$$

(4.11)

In this context, R_o signifies the estimated solvent radius, with a specific value for oxygen documented as 1.734 ångström.

Oxygen transport through Nafion ionomer was calculated using oxygen diffusivity revealed by Marr and Li [45] as

$$D^{eff}_{O2-M} = 1.3926 \times 10^{-10}\lambda^{0.708} exp\left(\frac{T-273.15}{106.65}\right)$$
$$-1.6461 \times 10^{-10}\lambda^{0.708} + 5.2 \times 10^{-10}$$

(4.12)
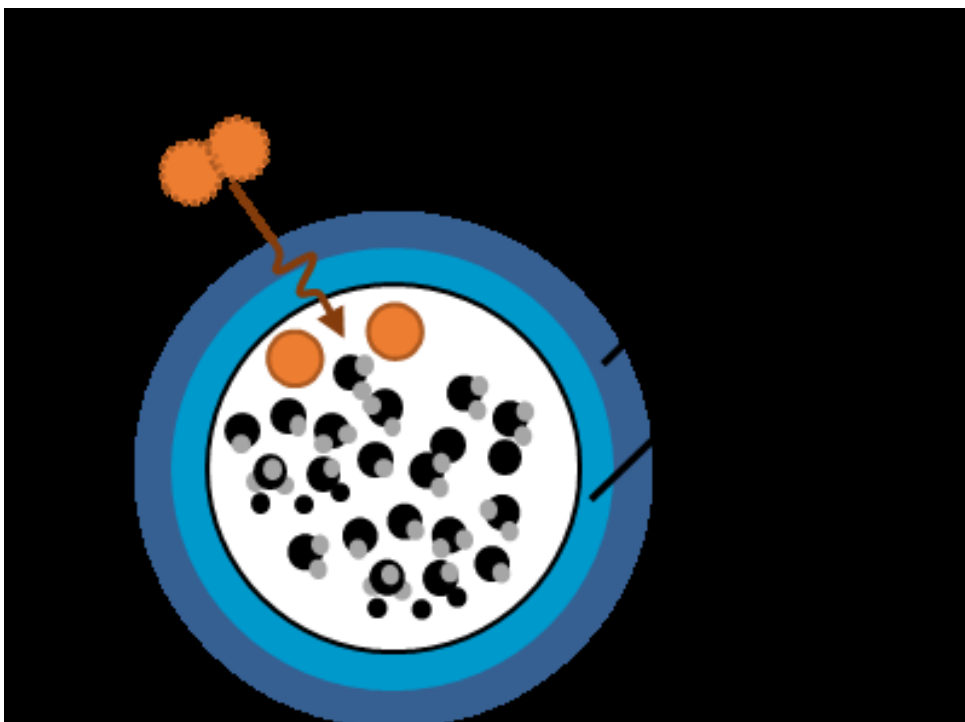
Figure 45 Graphical representation of the agglomerate model, illuminating the oxygen transport resistance by water and ionomer film.

4.2.5. Voltage Calculations and model validation

The voltage across a cell can be conceived as a holistic measure influenced by various contributing overvoltages. Computationally, the cell voltage is determined by subtracting the sum of activation and ohmic overvoltage from the open circuit voltage:

$$V_{cell} = V_{OCV} - \eta_{act} - \eta_{ohm} \qquad (4.13)$$

Historically, the model references the theoretical reversible voltage as a constant within the Nernst equation. However, utilizing the theoretical reversible voltage can lead to overestimating the open circuit voltage. This overestimation is attributed to its omission of voltage deterioration, mainly stemming from hydrogen crossover and mixed potentials that arise on the Pt/PtO catalyst surface [46]. Thus, an improved method to calculate the open circuit voltage was proposed, substituting Eq.(4.13)[47] into the Nernst equation

$$V_{OCV} = 0.0025\text{T} + 0.2329 \qquad (4.14)$$

Within the realm of activation overvoltage, our focus was restricted to the cathodic reaction kinetics; hence, a simple version of the Butler-Volmer equation was employed.

$$\eta_{act} = \frac{RT}{\alpha F} \ln\left(\frac{j}{j_o} \frac{C_{O_2}^{ref}}{C_{O_2}}\right) \qquad (4.16)$$

The ionic conductivity of Nafion manifests a strong dependency on its water content,

as articulated in Eq. (4.17) [8]. In our model, the proton conductivity of the membrane is posited to be half of that exhibited by a pristine Nafion membrane for the aforementioned reason.

$$\kappa = (0.005139\lambda - 0.00326) \exp\left(1268\left(\frac{1}{303} - \frac{1}{T}\right)\right) \qquad (4.18)$$

$$\kappa_{eff} = 0.5\kappa \qquad (4.19)$$

From there, the cumulative resistance was calculated as follows:

$$R_{ohm} = \frac{t_{mea}}{\kappa_{eff}} + \frac{2t_{GDL}}{\sigma} + R_{contact} \qquad (4.20)$$

Applying Ohm's law, we then derived the ohmic overvoltage:

$$\eta_{ohm} = IR_{ohm} \qquad (4.21)$$

Lastly, our model's foundational assumption was that all electrodes maintained an equipotential state. This assumption necessitated that all node voltages across the cell converge to a singular value. The nodal current underwent iterative adjustments until cell voltages were converged, as encapsulated by:

$$V_{cell} = V_{node} = \sum I_{node}R \qquad (4.22)$$

4.2.6. Pressure drops

The pressure within a PEM fuel cell exhibits variations primarily attributable to two distinct phenomena. The electrochemical reactions that unfold whin the cell contribute to the alteration in molecular count across channels. Simultaneously, as the supplied gas travel through the flow channel, it confronts frictional resistance. Although the variance caused by an electrochemical reaction can be dismissed as minimal and therefore omitted in the model, the pressure changes resulting from frictional forces are crucial and demand attention.

The Reynolds number and the friction coefficient were obtained in our attempts to quantify these changes. Both were ascertained using Eq. (4.23) to Eq. (4.24). When confronted with turbulent flow scenarios, the model invoked the Filonenko equation, premised on a smooth surface [48].

For Laminar Flow:

$$Re = \frac{\rho v D_H}{\mu} \tag{4.23}$$

$$Re < 2300, \ f = \frac{fRe}{Re} \tag{4.24}$$

For turbulent Flow

$$Re \geq 2300, \ D_{eff} = \left[\frac{64}{fRe}\right] D_H \tag{4.25}$$

$$Re_{eff} = \frac{\rho v D_{eff}}{\mu} \tag{4.26}$$

$$f = (1.82 \log_{10} Re - 1.64)^{-2} \tag{4.27}$$

Beyond the predominant head loss, minor head losses are incorporated to

encapsulate the pressure drop resulting from geometric intricates, such as 90 degrees bends. The major and minor pressure losses were deduced from Eq. (4.28) to Eq. (4.31).

$$h_f = f \frac{L}{D_h} \frac{v^2}{2g} \tag{4.28}$$

$$h_m = \frac{v^2}{2g} \Sigma K \tag{4.29}$$

$$h_{total} = h_f + h_m \tag{4.30}$$

$$\Delta p = \rho g h_{total} \tag{4.31}$$

Table 11 Laminar friction constants for the rectangular channel [49]

height/width	fRe	height/width	fRe
0.0	96.00	0.25	72.93
0.05	89.91	0.4	65.47
0.1	84.68	0.5	62.19
0.125	82.34	0.75	57.89
0.167	78.81	1.0	56.91

4.3. Oxygen Concentrator model

4.3.1. Model overview and key assumptions

The mathematical model delineating the oxygen concentrator's performance was crafted on the Matlab® platform. While the principle aim was to encapsulate the transient and dynamic behavior within the adsorption bed, several assumptions were indispensable to mitigate calculation speed. The major assumptions are detailed below:

(1) Ideal gas characteristics for gas phase.

(2) Radial variation within the adsorption bed is neglected.

(3) Extended Langmuir isotherm models represents the adsorption behavior.

(4) Linear Driving Force model using a lumped mass transfer is employed.

(5) Energy equations have been omitted for simplification.

4.3.2. Principal equations

Based on the assumption mentioned above, the adsorption behavior is articulated through following equations. Component and total mass balance equations, including an approximated axial dispersion coefficient, are given in (4.32a, 4.32b)[50].

$$-\varepsilon_b D_{ax}\frac{\partial^2 c_i}{\partial z^2} + \frac{\partial(v_g c_i)}{\partial z} + \left(\varepsilon_b + (1-\varepsilon_b)\varepsilon_p\right)\frac{\partial c_i}{\partial t} + \rho_p(1-\varepsilon_b)\frac{\partial q_i}{\partial t} = 0 \quad (4.32a)$$

$$-\varepsilon_b D_{ax}\frac{\partial^2 c}{\partial z^2} + \frac{\partial(v_{g_i} c)}{\partial z} + \left(\varepsilon_b + (1-\varepsilon_b)\varepsilon_p\right)\frac{\partial c}{\partial t} + \rho_p(1-\varepsilon_b)\frac{\partial q}{\partial t} = 0 \quad (4.32b)$$

c_i and q_i signify the gas and solid phase concentrations for component i, respectively. D_{ax} stands for the coefficient of axial dispersion, and its empirical equation is

provided by:

$$D_{ax} = 0.73D_m + \frac{v_g R_p}{\varepsilon_b \left(1 + 9.49 \frac{\varepsilon_b D_m}{2v_g R_p}\right)} \tag{4.33}$$

The axial pressure gradient within the packed bed is described by the Ergun equation.

$$-\frac{\partial P}{\partial z} = \frac{150\mu(1-\varepsilon_b)^2}{\varepsilon_b^3(2R_p)^2} v_g + 1.75\frac{(1-\varepsilon_b)\rho_g}{2R_p\varepsilon_b^3}|v_g| v_g \tag{4.34}$$

Here, R_p symbolizes the adsorbent particles' radius, while ε_b represents bed porosity. Furthermore, μ and ρ_g is for dynamic viscosity and fluid density, respectively.

The LDF model assumes that the driving force for the adsorption process is proportional to the difference between the concentration of adsorbate's bulk and surface concentration. The equation representing the adsorption isotherm is as follows.

$$\frac{\partial q_i}{\partial t} = \frac{\varepsilon_p}{\tau} \frac{15D_{c,i}(q_i^* - q_i)}{R_p^2} \tag{4.35}$$

$$q_i^* = \frac{IP_{1i} \times e^{\frac{IP_{2i}}{T}} \times P_i}{1 + \sum_i IP_{3i} \times e^{\frac{IP_{4i}}{T}} \times P_i} \tag{4.36}$$

The coefficient IP1, IP$_2$, IP$_3$, and IP$_4$ correspond to the isotherm model fitting parameters, as shown in **Table 12Table 12**. The corresponding experimental isotherm data measured by static volumetric methods at various temperatures are elucidated in **Figure 46**.

Specific boundary conditions were indispensable for the present investigation to simulate the cycle operation. For pressurization and adsorption phases, Danckwert's boundary conditions dictate the entry-point concentration for each constituent:

$$v\left(C_i - y_{i,f}\frac{P}{RT}\right) = \varepsilon_b \, D_{ax}\frac{\partial C_i}{\partial z} \, , \quad \text{for i} = 1, \dots, c \tag{4.37}$$

For the outgoing gas stream, the concentration's axial gradient becomes zero at the endpoint, adhering to the equation below:

$$\frac{\partial C_i}{\partial z} = 0, \text{ for } i = 1, \dots, c \quad (4.38)$$

Similarly, at the closed bed end, the axial gradient of the concentration also becomes zero, and the velocity at the end becomes zero:

$$\frac{\partial C_i}{\partial z} = 0, \ v = 0 \text{ for } i = 1, \dots, c \quad (4.39)$$

During the blowdown process, the molar flux rate is calculated using the following valve and velocity equations:

$$F = C_v(P_{in} - P_{out}), for \ P_{in} > P_{out} \quad (4.40)$$

Lastly, the oxygen purity metric is established as [51]:

$$\frac{\int_0^{t_{cycle}} F_{out} y_{out} dt}{\int_0^{t_{cycle}} F_{out} dt} \quad (4.40)$$

Table 12 Fitting Parameters for Extend Langmuir model, modified from [50]

Parameter	Nitrogen	Oxygen	Argon
IP1 (mol kg^{-1} kPa^{-1})	7.107×10^{-7}	6.861×10^{-6}	6.354×10^{-6}
IP2 (K)	2910	1567	1634
IP3 (kPa^{-1})	2.563×10^{-5}	4.625×10^{-5}	4.325×10^{-5}
IP4 (K)	1612	441.3	450.6
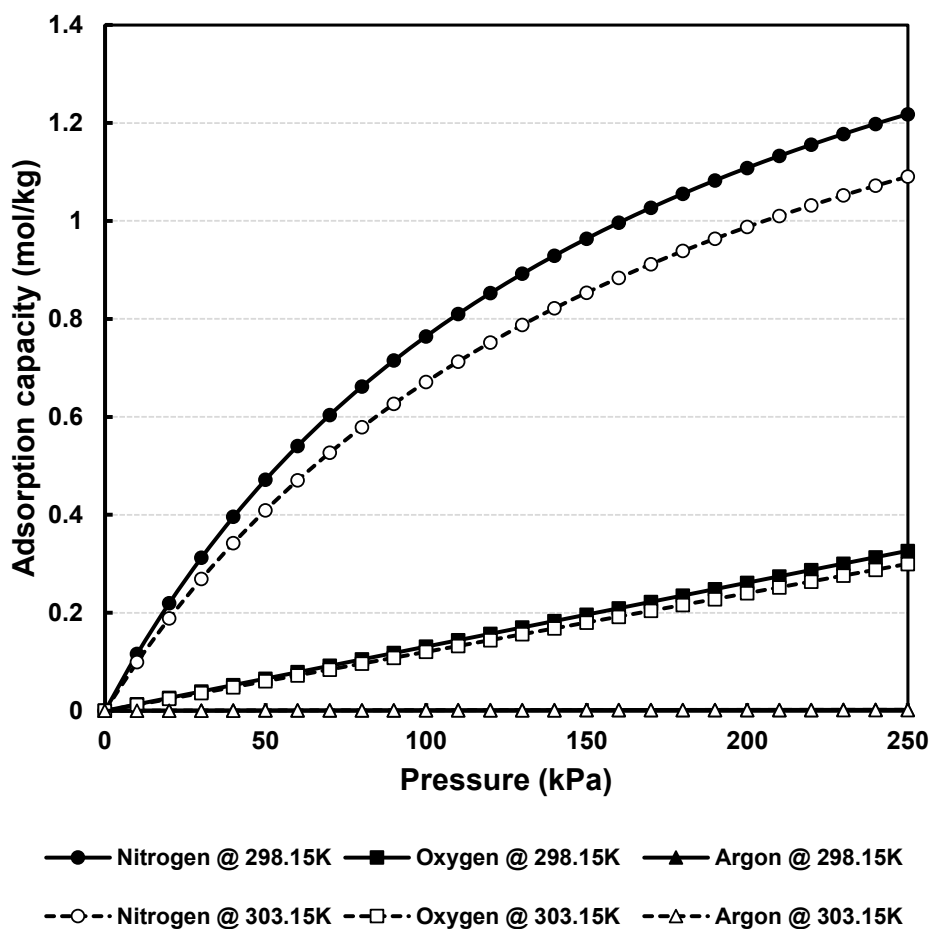
Figure 46 Estimated Adsorption isotherms of N$_2$, O$_2$, and Ar. on LiLSX using extend Langmuir model

4.3. Results and Discussion

4.3.1. PEM fuel cell under various oxygen concentrator

We present the comparison between the results obtained from the developed PEM fuel cell models and the experimental data from Chapter 2 for the model validation, and then we examine the effect of oxygen concentration on peak power density.

Figure 47 showcases the polarization curve obtained through experiments and simulations at different oxygen concentrations. To ensure accuracy, the comparison is limited to oxygen concentrations up to 50%, as higher concentrations required adjustments to the minimum flow rate in the experimental case due to the limitations in the nitrogen mass flow controller's precision. The developed model successfully captures the behavior of the voltage against current density, exhibiting similar slop in the ohmic resistance region and the point at which the slope increases due to concentration loss. Likewise, **Figure 48** compares the power density curve between experimental and simulation results, showing close agreement. However, slight differences are observed in activation loss and voltage deviations at high current density, particularly at an oxygen concentration of 50%. These discrepancies can be attributed to changes occurring in the actual cell at higher concentrations, such as enhanced cross-over effects, which were not fully accounted for in this model. Additionally, the existence of liquid water in the channels or partial blockage of gas passages is challenging to represent accurately in the developed model. Nonetheless, the model demonstrates high similarity with the actual experimental results, and its computational efficiency allows for rapid analysis.

Table 13 summarizes the changes in peak power density and corresponding current density at varying oxygen concentration. It is evident that the maximum

power density increases with current density, although its effects slightly fade with increasing oxygen concentration. Notably, between 21% and 40% oxygen concentrations, which nearly doubles the concentration, the peak current density rises from 0.72 to 1.17 W/cm^2, corresponding to a remarkable 62.5% enhancement in performance. Moreover, the peak current density demonstrates an increasing trend with higher oxygen concentrations, indicating a higher electrochemical reaction rate for a given cell voltage.

The significant increase in peak power resulting from oxygen enrichment offers the advantage of reducing the size of the fuel cell stack and thus saving on costly materials like a platinum catalyst. However, from a system perspective, the increased current range leads to increased heat generation from electrochemical reactions, imposing an additional load on the cooling system. Furthermore, thicker electric wires are necessary to accommodate the augmented current flow.

In conclusion, the developed model exhibits commendable accuracy compared to experimental results and provides rapid calculation. The impact of oxygen concentrations on fuel cell can be easily estimated through this model and can act as a instrument in optimizing the design and operation of the fuel cell with an oxygen concentration.
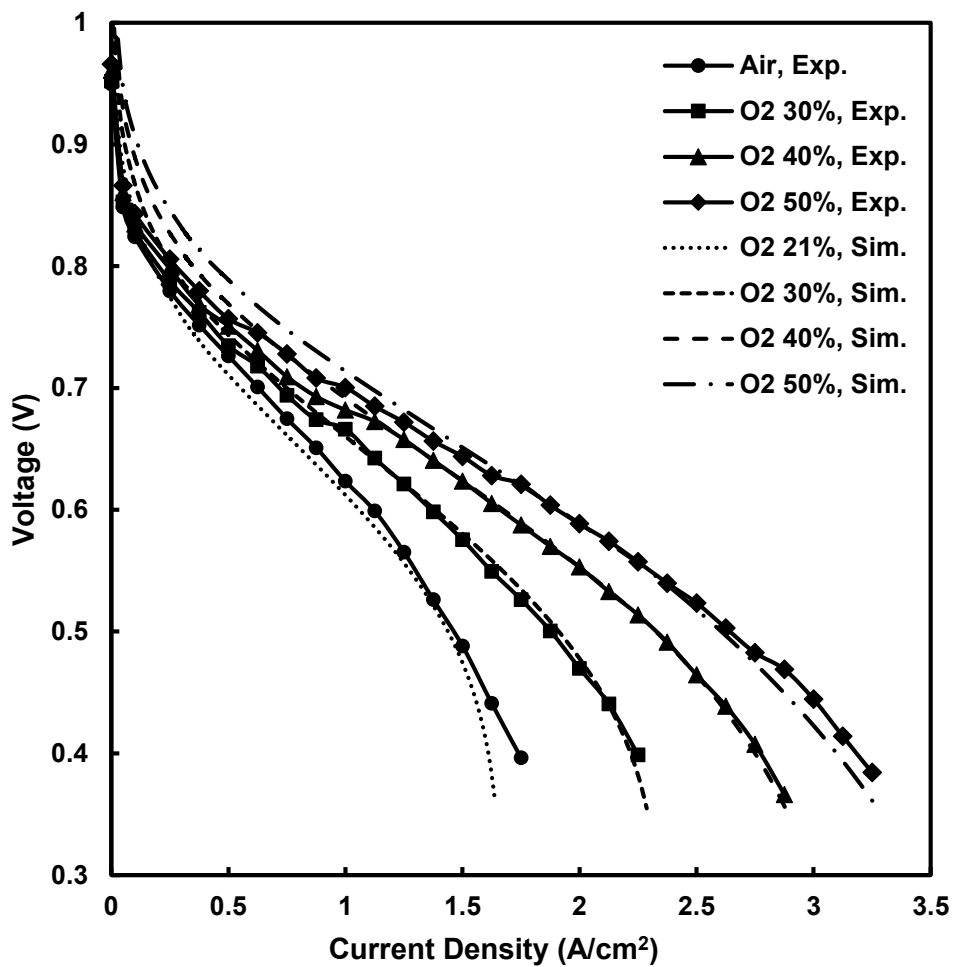
**Figure 47 Comparison of polarization curves: experimental result and simulation
results at varying oxygen concentration (21% to 50%)**
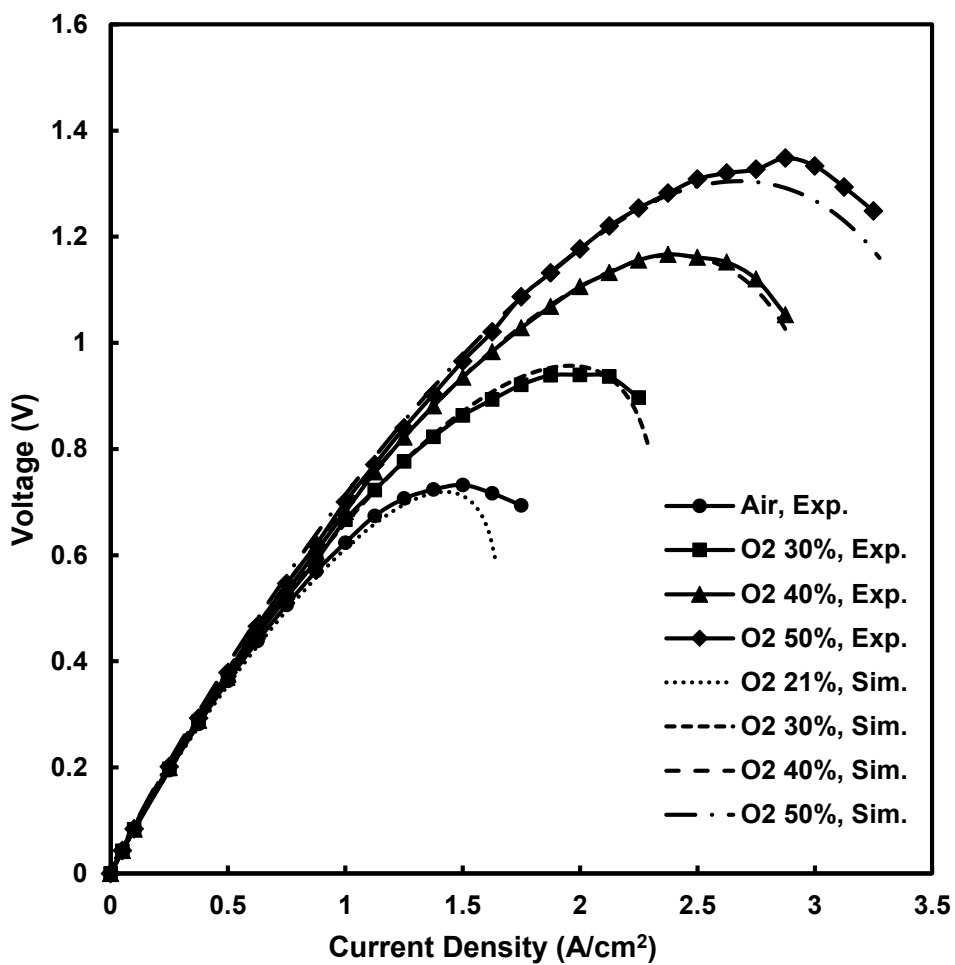
Figure 48 Comparison of power density curves: experimental result and simulation results at varying oxygen concentration (21% to 50%)

Table 13 Impact of oxygen concentration (21% to 50%) on peak power density and its corresponding current density

Oxygen Concentration	21%	22%	23%	24%	25%	26%	27%	28%	29%	30%	31%	32%	33%	34%	35%
Maximum power density (W/cm²)	0.72	0.75	0.78	0.80	0.83	0.86	0.88	0.91	0.93	0.96	0.98	1.00	1.03	1.05	1.07
Corresponding Currnet density (A/cm²)	1.42	1.48	1.55	1.61	1.67	1.73	1.79	1.85	1.91	1.95	2.01	2.06	2.13	2.17	2.23
Oxygen Concentration	36%	37%	38%	39%	40%	41%	42%	43%	44%	45%	46%	47%	48%	49%	50%
Maximum power density (W/cm²)	1.09	1.11	1.13	1.15	1.17	1.18	1.20	1.21	1.23	1.24	1.25	1.27	1.28	1.29	1.30
Corresponding Currnet density (A/cm²)	2.28	2.30	2.31	2.36	2.40	2.43	2.46	2.50	2.54	2.55	2.58	2.60	2.63	2.66	2.68

4.3.2. Estimated Performance of the developed oxygen concentrator

A comparison of the results derived from the oxygen concentrator model and the actual experimental data is depicted in **Figure 49**. As the duration of the adsorption process lengthens, there is a notable decline in purity. This trend is attributed to the saturation of the adsorbent materials, in this particular instance, Li-LSX. In parallel, a longer duration of adsorption amplifies the overall flow rate, consequently enhancing the oxygen recovery values.

Although the simulation shows a slight discrepancy in recovery calculation at adsorption times of 10 and 30 seconds, it generally adheres to the experimental trend. The margin of error could likely be associated with the inconsistencies stemming from the valve orifices. Despite this deviation, the developed model can still serve as a robust reference point for the design parameters of the oxygen concentrator. in can inform critical decisions such as the dimensions of the adsorbent materials for specific flow rates or the optimal settings for operation duration.

Figure 50 provides insight into the relationship between oxygen purity and the product flow rate. As the output flow rate approaches the upper limit of the inlet flow rate, which is fixed at 6 LPM, a discernible decline in the oxygen purity from the concentrator can be observed. This phenomenon can be attributed to the inadequate temporal span for the chamber's pressurization, which hampers the adsorption process.

On the other hand, an escalation in oxygen concentration reduces the output flow rate. This is due to the additional time required to pressurize the adsorbent chamber, resulting in a momentary interruption of the outlet flow. A delicate balance between oxygen concentration and product flow rate is vital to ensure an efficient coupling with the PEM fuel cell. This balance not only assures high-purity oxygen

gas but also prevents an undue decrease in product rate, enhancing overall performance.

Given the constraints that prohibit the modification of the size of the oxygen concentrator, the settings derived form the model serve as a pragmatic starting point. They aid in determining the cycle timing, calibrated to achieve the target purity.
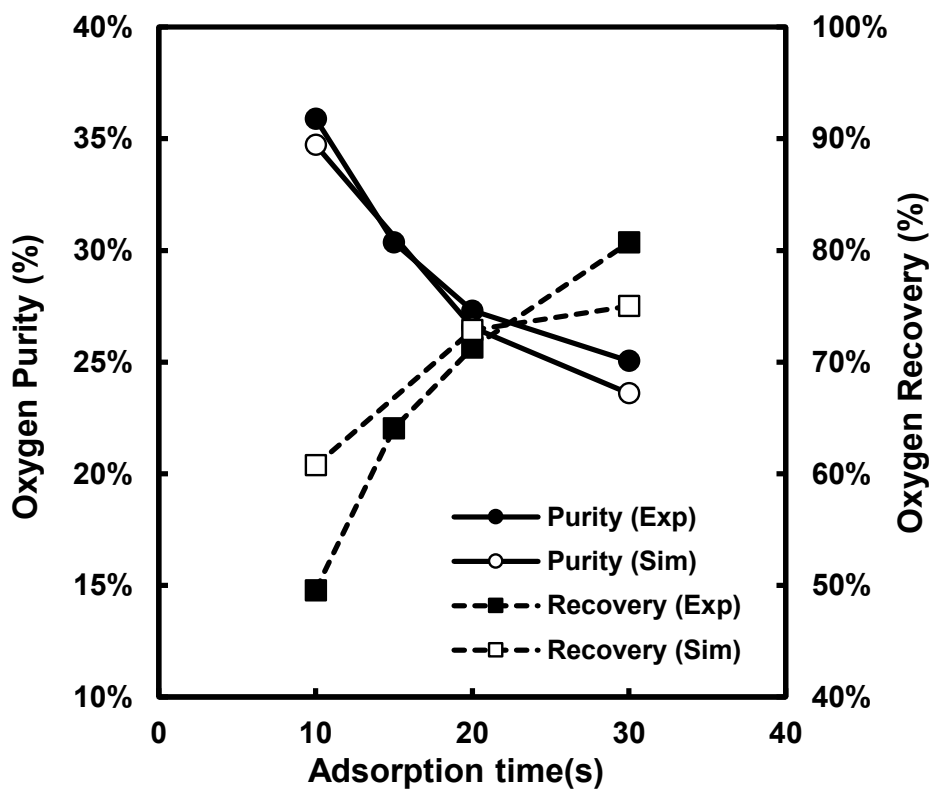
Figure 49 Comparison of simulation and experimental results for adsorption

duration's impact on oxygen purity and recovery
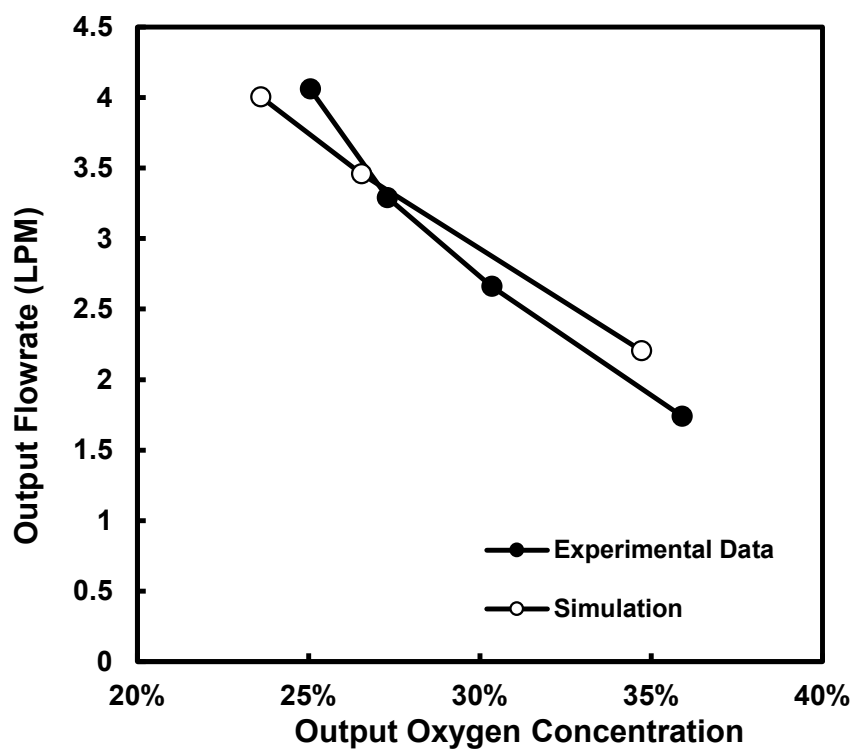
Figure 50 Oxygen concentration vs. product flow rate of the concentrator

4.4. Summary

This chapter has focused on developing and analyzing two models, the PEM fuel cell and the oxygen concentrator. The PEM fuel cell model served as a key tool in establishing the peak power and corresponding current, or in other words, the flow rate. By manipulating the feed gas composition, we were able to calibrate the desired flow rate and optimize performance by incrementally enriching the oxygen content by 1%. The model demonstrated significant performance enhancements in conditions close to air. However, the rate of performance improvement declined with increasing oxygen concentration, with a 1% increase leading to a performance enhancement of 0.3 W/cm^2 at 21% oxygen concentration, but only an improvement of 0.1W/cm^2 at 50% oxygen concentration. It is also important to highlight that a rise in current inevitably increases heat generation, as more electrochemical reactions occur for the same overpotential. This intensifies the demand for the cooling load, a factor that must be carefully considered when designing an integrated system.

The oxygen concentrator model displayed relatively good agreement with the experimental results. However, due to the lack of precision in isotherms and orifice information, some level of error was inevitable in the results. Therefore, the model primarily serves as a reference point for adjusting the cycling timing to achieve the target oxygen concentration. As this research focuses on assessing the feasibility through experimental data, the oxygen concentrator model was not extensively refined. This allows us to concentrate our efforts on verifying the model's accuracy with real-world performance data, thereby enhancing the practical relevance of our research.

Chapter 5. PEM fuel cell with an oxygen concentrator

5.1. Introduction

This chapter focuses on the practical application of our developed small-scale oxygen concentrator in supplying enriched oxygen to a PEM fuel cell, allowing us to observe the interaction between these two systems. We conduct experimental tests to explore and discuss two distinct methods for supplying oxygen-enriched gas to the PEM fuel cell. The first method employs an MFC to regulate and supply gas at a consistent flow rate. The second method involves manipulating the backpressure regulator and orifice size to supply the PEM fuel cell. Drawing on the experimental results from the previous chapters, we have defined the target operating conditions for oxygen concentrations for the concentrator in these experiments. The system is scaled up to gauge the potential power enhancement in a 100kW PEM fuel cell. This chapter thereby bridges theory and application, providing valuable insight into the practical functioning of our proposed system.

5.2. Experimental Setup

The experimental setup employed in this study involved the same PEM fuel cell used in the preceding chapter. We utilized Li-LSX molecular sieve as the adsorbent materials in the oxygen concentrator, and a sizable buffer tank was employed to reduce the flow fluctuation. The air supply to the oxygen concentrator was regulated using FCs, delivering a steady flow at 5 LPM.

The PSA cycle process employed followed the same sequence detailed in the prior chapter. The intervals set for pressurization, adsorption, pressure equalization, and the purge step were 1 second, 14 seconds, 1 second, and 1 second,

respectively. As shown in **Figure 51,** when using the MFCs, positioned downstream of the product stream of the oxygen concentrator, the backpressure regulator was fully opened, and the flow rate was established at 1 LPM.

Mass flow meters, situated between the product buffer tank and the product MFC, were responsible for monitoring the pressure and flow rate of the gas. For the second set of experiments, the downstream MFC was fully opened to avoid impeding the flow to the PEM fuel cell, and the backpressure regulators were meticulously adjusted to yield an average product stream flow rate of 1 LPM.

The hydrogen gas flow rate was set to 0.571 LPM, equivalent to the flow rates at a stoichiometric ratio of 1.5 for a current density of 2.5A/cm^2. Polarization curves were conducted using the same instrumentation and procedures described in the previous chapter.
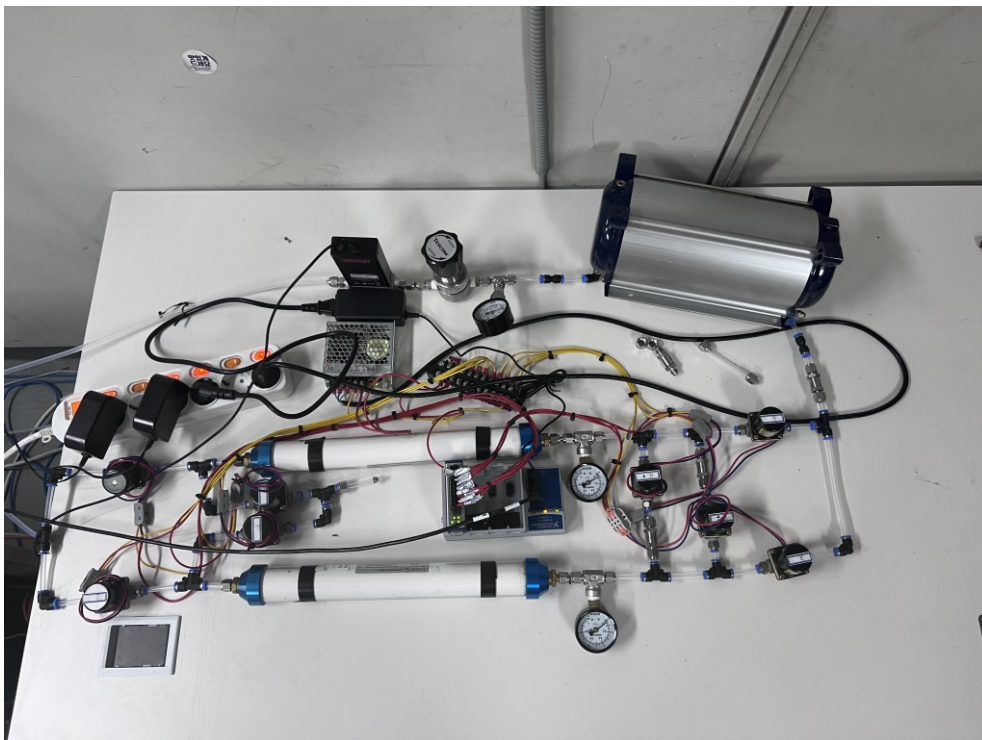
Figure 51 Oxygen concentrator used to operate a PEM fuel cell

5.3 Results and discussion

Considering both our PEM fuel cell and the oxygen concentrator based on previous results, we deduced that optimal performance would occur when the air was fed at a rate of 5 LPM, and the target oxygen concentration was approximately 40%. The oxygen concentrator was set to operate at these conditions regardless of whether an MFC or orifice controlled the outlet.

Figure 52 displays the polarization and power density curves for both, exhibiting almost identical results. Initially, using a valve to adjust the flow rate might appear to be a better choice, as it does not consume energy. However, the inevitable fluctuation in the flow rate consequently causes voltage fluctuation. This fluctuation intensifies as the stoichiometric ratio dips below 2.0, as evidenced by a higher voltage standard deviation depicted in **Figure 53**. Thus, despite wavy-type flow channels that generate pressure and flow swings and are known to improve fuel cell performance [52], [53], the lack of through-plane convection force and the slow frequency of flow rate fluctuation does not elicit such a positive effect.

The significance of our developed oxygen concentrator lies in its ability to maintain an average pressure of 0.75 bar in the product buffer tank, which is significantly lower than the standard operating pressure of conventional oxygen concentrators. Considering a small medical oxygen concentrator unit such as the Weinman, which is known to operate between 0.1 and 0.3 MPa [54], our developed oxygen concentrator still demonstrates a significant advantage due to its lower operating pressure. This lower operating pressure implies reduced energy demand for compression and potentially lower costs and longer equipment lifespans due to decreased stress on system components. This operation condition, coupled with out

concentrator's performance in terms of oxygen output and fuel cell efficiency, positions our design favorably for use in various applications where low-pressure operation is beneficial. The specific work of the isentropic compressor is calculated using the following equation [55]:

$$\omega_{comp} = \frac{kRT_1}{k-1}\left[\left(\frac{P_2}{P_1}\right)^{(k-1)/k} - 1\right] \qquad (5.1)$$

Actual compressor work deviates from this ideal due to factors like friction and heat transfer. The overall compressor efficiency varies depending on compressor type and size, necessitating actual measurement. For instance, centrifugal compressors typically have an efficiency ranging from 0.70 to 0.85, rotary screw compressors range from 0.65 to 0.75, and reciprocating compressors range from 0.72 to 0.90 [56]. For the calculation of compressor work, we assumed an overall efficiency value of 0.7.

Table 14 outlines the performance of our developed oxygen concentrator, the estimated air compressor power, and the resulting net power of the fuel cell. Case 14 shows the highest net power of 4.6 W for each oxygen concentrator, but the operating pressure is 1 bar(g). The isentropic relationship for an ideal gas shows that when a gas at 298K is pressurized to 1 bar, its temperature will rise to about 363K. This temperature is near the boiling point of water, which has negative implications for the operation of an oxygen concentrator. The adsorption capacity of the adsorbent decreases with increasing temperature[57]. Therefore, an aftercooler would be required to lower the gas temperature before it enters the adsorbent bed. The use of an aftercooler, however, would increase the auxiliary power, promoting us to search for configurations with better net power.

Cases 19, 20, and 21 seem promising, with all of them operating at a lower pressure of 0.5 bar(g), which reduces the compressor workload and consequently decreases the temperature rise from compression. The temperature of the gas exiting the compressor is theoretically 335K. Since the gas temperature is near the operating fuel cell temperature, the decline in adsorption capacity resulting from increased temperature is counterbalanced by the fact that a heated feed gas stream can facilitate the humidification process of the reactant gas more efficiently. Thus, these conditions were chosen as candidates for optimal operating points for the oxygen concentrator.

Case 20 was selected as the base operating condition for this specific oxygen concentration, even though Case 21 performed slightly better. This decision was based on the fact that Case 20 has a flowrate of 0.85 LPM, whereas Case 19 has a flow rate of 0.49 LPM. A higher flow rate is expected to enhance the removal of liquid water in the channels of the PEM fuel cell.

This comprehensive table also enables us to observe the effect of air flow rate, adsorption duration, pressure equalization, and purge duration on concentrator performance. as the air flow rate increases, the adsorbent reaches saturation faster, resulting in higher purity for the given time at the slower flow rate, provided the adsorption pressure remains constant. As the adsorption timing increase, the oxygen purity decreases. The pressure equalization step, which alleviates the compressor workload, should be as short as possible to avoid wasted time. Although it was possible to decrease the pressure equalization step to 0.5 seconds, which showed a tenuous improvement in performance, we set the step to 1 second to prevent any potential malfunction and durability of the solenoid valve. Lastly, the purge duration, critical for achieving higher oxygen concentration, should be as short as possible. It

occurs after the adsorption process, which leads to a decrease in the overall flow rate and poses the risk of re-saturating the exhaust stream.

Table 15 demonstrates the potential implications of our oxygen concentrator if scaled up and applied to a 100-kW fuel cell stack. Given a 100-kW fuel cell stack that operates in air, incorporating an oxygen concentrator could yield a 34% increase in nominal power. However, this would require approximately 3250 kg of adsorbent. The utilization of the oxygen concentrator in conjunction with the PEM fuel cell is best suited for stationary applications due to the oxygen concentrator's slower response than the PEM fuel cell, necessitating numerous cycles before reaching a steady cyclic state. The mass of the adsorbent could be reduced through faster cycling time, albeit at the cost of a decrease in power improvement.

In conclusion, integrating a PEM fuel cell and an oxygen concentrator is a feasible strategy for stationary power generation applications. This is attributed to advancements in nitrogen-adsorbing materials and reconsiderations of operating pressure. Additionally, the prospect of employing VSA and VPSA techniques in the PEM fuel cell system should be explored as they can further enhance fuel cell power generation when used with an oxygen concentrator.
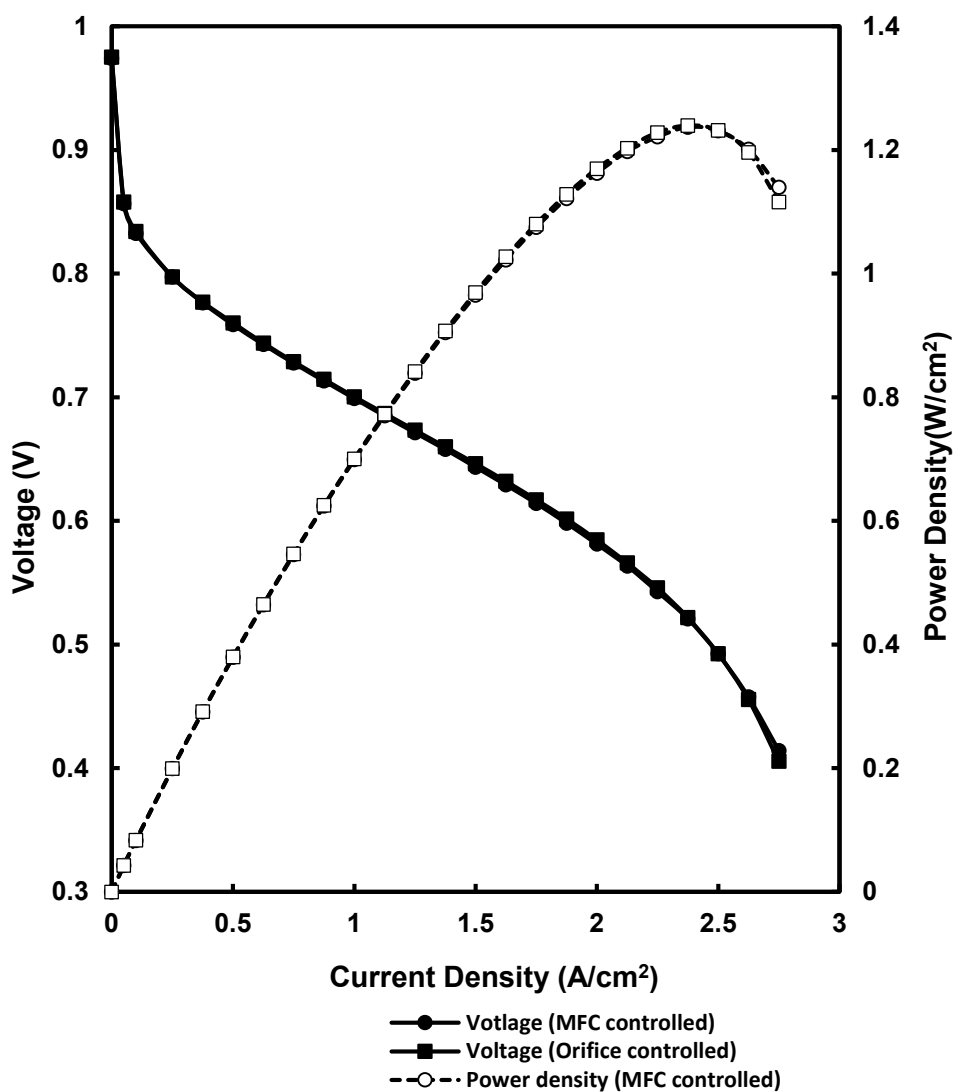
Figure 52 Polarization and power density curves for MFC-controlled and orifice-controlled PEM fuel cell with an oxygen concentrator
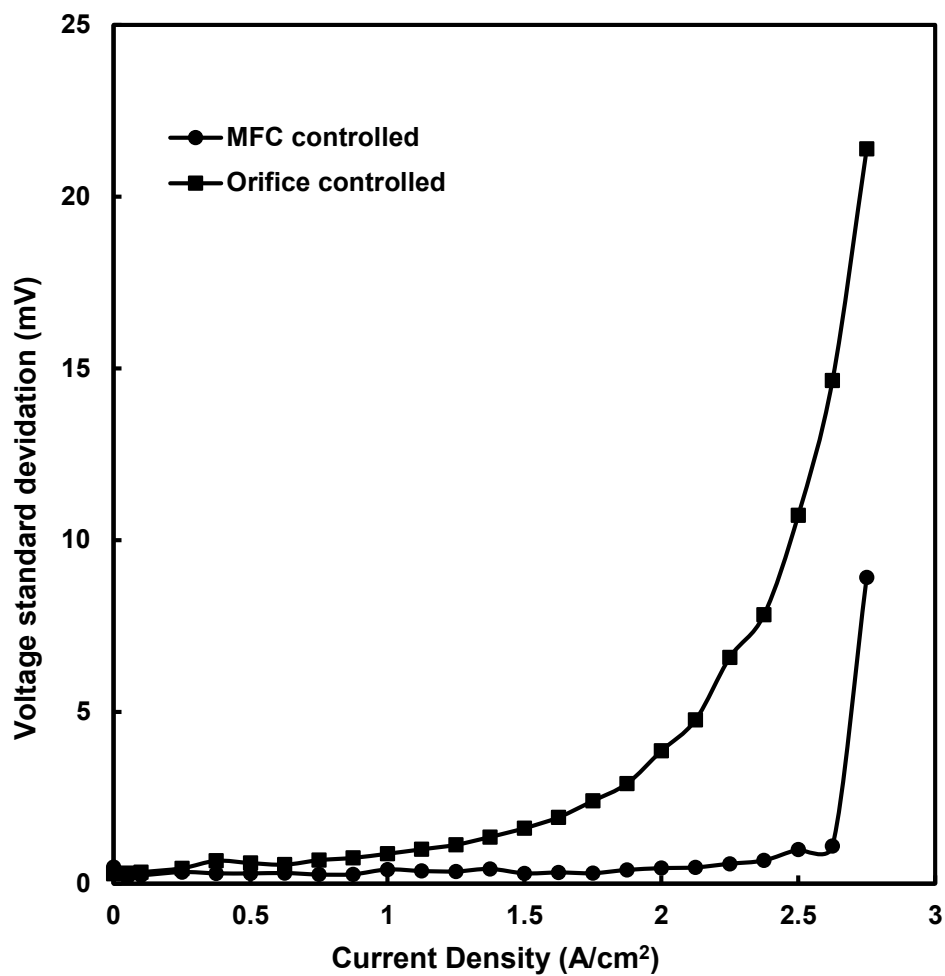
Figure 53 Standard deviation of voltage for MFC-controlled and orifice-controlled PEM fuel cell with an oxygen concentrator

Table 14 Estimated net power of PEM fuel cell with developed oxygen concentrator under different operation parameters for the concentrator

case	Air Flow Rate	Max. Pressure	Comp. (n=70%)	PR. + AD.	PE.	Purge	Product Flow Rate	O2 Purity	Fuel Cell Power	Net Power
	(LPM)	(bar(g))	(W)	(s)	(s)	(s)	(LPM)	(%)	(W)	(W)
1	6	1.5	15.2	60	1	0	0.85	30%	3.6	-11.5
2	6	1.5	15.2	60	1	1	1.12	26%	2.7	-12.5
3	6	1.5	15.2	60	1	2	1.09	25%	2.1	-13.0
4	6	1.5	15.2	45	1	1	0.90	29%	3.6	-11.6
5	6	1.5	15.2	35	1	1	0.55	40%	5.1	-10.1
6	6	1.5	15.2	35	1	2	0.56	39%	4.8	-10.4
7	6	1	11.1	35	1	2	3.40	27%	9.0	-2.1
8	6	1	11.1	35	1	1	3.46	27%	9.3	-1.8
9	6	1	11.1	30	1	1	3.33	28%	11.0	-0.1
10	6	1	11.1	25	1	1	2.86	30%	12.3	1.2
11	6	1	11.1	25	1	2	2.69	31%	12.2	1.1
12	6	1	11.1	25	0.5	1	2.67	31%	12.5	1.4
13	6	1	11.1	20	1	1	2.32	32%	12.2	1.1
14	6	1	11.1	15	1	1	1.38	44%	15.7	4.6
15	3	1	5.5	25	1	1	0.23	72%	5.5	0.0
16	3	1	5.5	30	1	1	0.55	48%	7.3	1.8
17	3	1	5.5	35	1	1	0.85	39%	7.5	1.9
18	3	1	5.5	45	1	1	1.25	32%	6.3	0.7
19	3	0.5	3.1	15	1	1	0.49	47%	6.2	3.0
20	**3**	**0.5**	**3.1**	**20**	**1**	**1**	**0.85**	**36%**	**6.1**	**3.0**
21	3	0.5	3.1	25	1	1	1.09	33%	6.0	2.9
22	3	0.5	3.1	30	1	1	1.46	29%	5.8	2.7
23	3	0.5	3.1	35	1	1	1.52	28%	4.9	1.8
24	3	0.5	3.1	45	1	1	1.75	26%	3.9	0.8

Table 15 Impact of oxygen concentrator on a 100 kW fuel cell stack

Parameters	Air	Enriched O_2	Note
Active area (cm^2)	300	300	
Number of cells	440	440	
Operating pressure (bar)	1	1	
Current density (A/cm^2)	1.5	2.2	
Flow Rate (LPM)	7172	5774	SR2.0
Compressor work (kW)	0	6.0	0.5bar(g)
Stack power (kW)	96.7	135.7	
Net power (kW)	**96.7** **(-)**	**129.7** **(34%)**	3250 kg adsorbent

Chapter 6. Flow channels for PEM fuel cell with oxygen concentrators

6.1. Introduction

The primary focus of improving the performance of PEM fuel cells has been to increase the feed oxygen concentration. However, to further enhance the cell's performance, it is crucial to reduce oxygen transport resistance. This resistance represents the obstruction that oxygen encounters before it reaches the catalyst surface, which impedes the electrochemical reaction. As mentioned in the previous chapter, the inhomogeneous gas composition along the channels can negatively impact cell performance. Various heterogeneous designs, such as gradient-structured flow channels or gas diffusion layers, have been developed and adopted to mitigate this adverse effect. While the effects of gradient flow fields on the cathode have been researched extensively, since the oxygen concentrator reduces the cathode overvoltage from concentration loss, it becomes essential to analyze other resistances, such as the membrane and anodic loss.

Moreover, the higher operating current requires an improved flow field design to mitigate the imbalance between both sides of the membrane. In this chapter, we examine the impact of applying anode gradient flow fields to determine its worthiness in improving the PEM fuel cell system's performance. The anode gradient flow fields focus on reducing the performance deterioration caused by composition variation along the channels and the membrane dehydration from the electro-osmotic drag. The contents of this chapter are published in a journal paper [58].

6.2. Experimental Setup

6.2.1. Flow fields with gradient design

This study examined gradient-designed flow fields in parallel serpentine channels and metal foam configurations, as shown in **Figure 54**. The parallel serpentine channels consisted of five channels, each with a width of 1 mm and a land width of 1.04 mm. The channel depth varied progressively from the inlet to the outlet, ranging from 0.4 mm to 0.8 mm, thereby creating a depth gradient.

Metal foam flow fields were prepared by inserting metal foam into square pockets on the bipolar plate. To create metal foam flow fields with gradients, we adjusted the square pock depth on the bipolar plate, which gradually changed from 0.5 mm at the inlet to 0.9 mm at the outlet in a diagonal direction, as illustrated in **Figure 55**(a). In addition to the depth gradient, we inserted metal foam with a uniform thickness. This variation in depth led to differences in compression ratio across the flow fields, resulting in a gradient of porosities, as shown in **Figure 55**(b). All flow fields were designed to be rotatable by 180 degrees, allowing the gradient slope at the inlet to switch from positive to negative.

Metal foam penetrates into the gas diffusion layer upon assembling metal foam flow fields, reducing interfacial contact resistance [59]. However, it is essential to address an inherent challenge, which is the damage to the carbon fibers in the gas diffusion layer. This concern becomes more pronounced for depth gradient designs, where the shallow sections require higher metal foams compression, resulting in excessive local pressure that could exacerbate the damage to the gas diffusion layers. To counteract this issue, metal foams were initially compressed using slightly thicker Teflon gaskets without the presence of gas diffusion layers or MEA. This approach

ensures that, upon cell assembly, the metal foams apply pressure evenly on the gas diffusion layers. Consequently, the metal foam adequately intrudes the gas diffusion layer to enhance contact area while minimizing potential damage.

For cathode flow fields, the implementation of porosity gradient flow fields can significantly enhance cell performance by promoting improved diffusion, particularly at the corners, as supported by our prior research findings [60]. In this study, we utilized gradient metal foams for the cathode flow fields, featuring a diagonal decrease in both thickness and porosity from the inlet to the outlet. This optimized cathode design minimized the potential overshadowing effect of oxygen mass transport on the cathode side, ensuring a focused investigation of the anode dynamics. This approach enabled a clearer understanding of the specific effects and dynamics occurring on the anode side, leading to a comprehensive optimization of fuel cells.

The specifications of the flow field are presented in **Table 16**. Flow fields for Cell 5 – 7 were designed for compatibility with both unit cell and stack configurations. The inlets and outlets were enlarged and positioned further away from the active area to accommodate this dual-purpose functionality. This design helps reduce pressure buildup that may arise from the increased flow rates in stack cell applications. To address these adjustments, modification to the header was implemented to mitigate potential concerns associated with local compression. Nonetheless, the general trends observed in the experimental outcomes persisted despite these alterations.
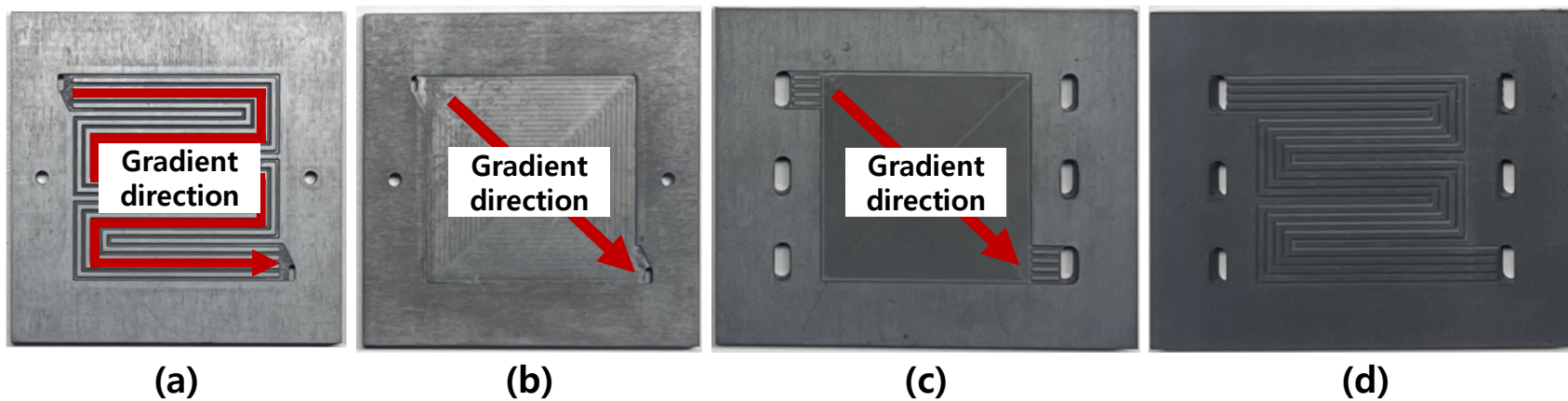
Figure 54 Anode flow field configurations: (a) Cell 1 & 2 – depth-gradient parallel serpentine channel (0.4 mm to 0.8 mm); (b) Cell 3 & 4 – depth-gradient metal foam (0.5 mm to 0.9 mm); (c) Cell 5 & 6 – depth-gradient metal foam (0.5 mm to 0.9 mm); (d) Cell 7 – constant-depth parallel serpentine channel (0.4 mm).
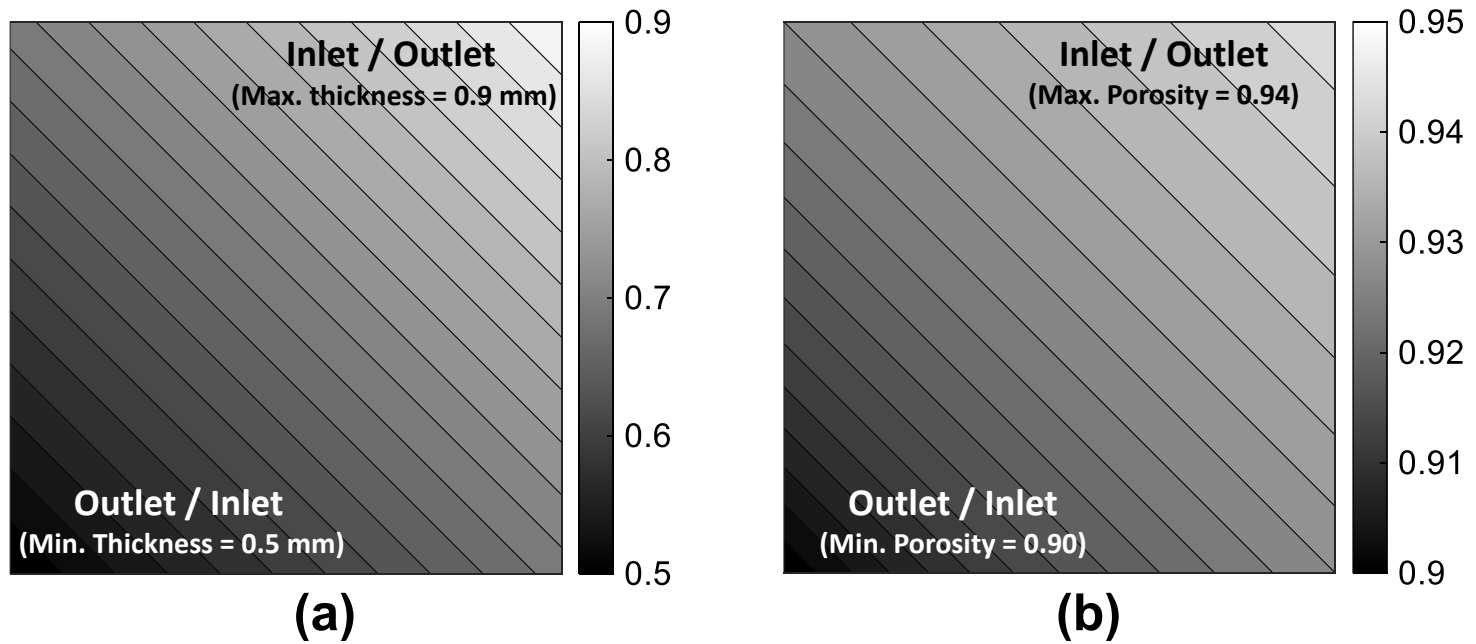
Figure 55 Contour plot of (a) metal foam thickness distribution and (b) metal foam porosity distribution.

Table 16. Specifications of flow fields

Parameter	Cell 1	Cell 2	Cell 3	Cell 4	Cell 5	Cell 6	Cell 7
Anode							
Flow field type	Channel	Channel	Metal foam	Metal foam	Metal foam	Metal foam	Channel
Inlet depth or thickness (mm)	0.8	0.4	0.9	0.5	0.9	0.5	0.4
Outlet depth or thickness (mm)	0.4	0.8	0.5	0.9	0.5	0.9	0.4
Gradient	Descending	Ascending	Descending	Ascending	Descending	Ascending	None
Metal foam plating	N/A	N/A	Gold	Gold	None	None	None
Cathode							
Flow field type				Metal foam			
Inlet thickness (mm)				0.9			
Outlet thickness (mm)				0.5			
Metal foam plating	Gold	Gold	Gold	Gold	None	None	None

6.2.2. Metal foams

This study used commercial nickel metal foams with 2.5 mm thickness, 800-micron cell size, and 98% open porosity (Alantum, Germany). The nickel foam was compressed to a thickness of 1 mm and cut into 50 mm by 50 mm pieces to match the active area of the membrane electrode assembly (MEA). A minimum gap of 0.1 mm between the bipolar plate pocket and the metal foam was maintained to guarantee compression, ensuring film contact between the bipolar plate and the gas diffusion layer (GDL). Both gold-plated and plain nickel metal foams were used. Gold-plating offers enhanced corrosion resistance and minimizes metal dissolution, which can influence the degradation rate of fuel cells. To evaluate the effect of anode flow fields, gold-plated nickel foam was employed to eliminate the degradation factor. In contrast, plain nickel foams were used in accelerated stress tests (AST) to expedite degradation.

6.2.3. Experimental conditions for fuel cell tests

The experimental conditions for the fuel cell tests are summarized in **Table 17**. The cell was operated at a temperature of 60 °C and ambient pressure. The stoichiometric ratios for the anode and cathode were set at 1.5 and 2.0, respectively, maintaining a minimum flow rate corresponding to 10 A. Relative humidity was controlled by humidifying reactant gases with membrane humidifiers.

Table 17 Experimental Conditions and Measurements

Parameter	Value
Operating temperature (°C)	60
Stoichiometric ratio	1.5 for the anode, 2.0 for the cathode
Relative humidity of feed gas (%)	30, 60, 100
Current (A)	0, 1, 2, 5, 10, 15… 60 (2.5)
Voltage measuring frequency (Hz)	100
Measuring period for each step (s)	120
EIS measuring frequency (Hz)	0.5 – 10,000
EIS measuring AC (%)	5.0
EIS moving average	16

6.2.4. Experimental conditions for accelerated stress tests

Accelerated stress tests were conducted using a catalyst support degradation protocol adapted from the 2017 US Fuel Cell Technical Team (FCTT) roadmap [61], with modifications outlined in Table 18. The tests involved potential cycling between 1.0 V to 1.5 V at a sweep rate of 500 mV/s to simulate unmitigated start-up or shutdown scenarios. The operating temperature was maintained at 60°C, and fully humidified hydrogen and nitrogen gas were supplied to the anode and cathode at a 200 cc/min flow rate.

Polarization curve, EIS spectra, and transient response results were obtained after 5k, 10k, and 15k cycles of potential cycling to assess the impact of catalyst support degradation on the fuel cell performance. The transient response was measured by imposing a sudden current from 0.4 A/cm2 to 1.2 A/cm2 and recording the cell voltage for 180 seconds.

Table 18 Degradation protocol

Parameter	Value
Cycle	Triangle sweep between 1.0 to 1.5 V at 500 mV/s
Cycle time (s)	2
Operating temperature (°C)	60
Relative humidity of fuel / oxidant (%)	100
Fuel / oxidant	Hydrogen gas / Nitrogen gas
Flow rate of fuel / oxidant (ccm)	200 / 200
Pressure	Ambient pressure

6.2.4. Experimental apparatus

The fuel cell testing station consisted of mass flow controllers (MC-Series, Alicat Scientific, USA), electronic back pressure regulators (PC-Series, Alicat Scientific, USA), and membrane humidifiers. An electronic load (PLZ664WA, Kikusui Electronics, Japan) was used to obtain the current-voltage response of the fuel cell, while a fuel cell impedance meter (KFM2150, Kikusui Electronics, Japan) was utilized to measure the impedance. A DC Power supply (PWR1201L, Kikusui Electronics, Japan) was used for the degradation test. A 25 cm^2 (5 cm by 5 cm) active area, commonly employed, was selected based on careful consideration of data measurement accuracy, the capacity to capture gradient flow field effects, cost-effectiveness, and comparability with previous research. The MEA used in the experiments is a commercially available product (VFP-01625-GN, Vinatech, South Korea), which features a reinforced membrane with a platinum loading of 0.45 mg/cm2 on both sides. The thickness of the membrane with the catalyst is 45 μm. A 315 μm thick GDL, incorporating a 5% (w/w) PTFE-treated paper-type substrate and a microporous layer (Sigracet 39BB, SGL Carbon, Germany), was utilized. The cell temperature was controlled by cartridge heaters with a fan or a circulating bath (RW3-2025P, Jeio tech, South Korea), depending on the presence of cooling channels.

6.3. Results and Discussion

6.3.1. Effect of anode flow fields with gradient design in cell performance

Polarization curves serve as a fundamental tool in evaluating the performance and efficiency of fuel cells. Polarization curves can be divided into four distinct regions, each characterized by a dominant loss mechanism: activation losses, ohmic losses, concentration losses, and fuel crossover and short circuit losses [62]. These mechanisms manifest at varying intensities throughout the entire range of current loading. Activation losses correspond to the sharp voltage drop at low current densities, resulting from the activation energy barrier for oxidation and reduction processes at the electrodes. Ohmic losses occur at intermediate current densities, causing a linear region in the polarization curve. These losses primarily stem from the electrical resistance within cell components, such as the MEA, GDL, and bipolar plates. At high current densities, concentration losses arise when reactant consumption exceeds the mass transport rate, leading to reactant depletion at the catalyst interface and a downward curve in the polarization curve. Lastly, Crossover and short circuit losses arise from the diffusion of reactants through the electrolyte, where they react without external electron transfer due to the internal current resulting from incomplete electron insulation. These phenomena contribute to the fuel cell inefficiencies, and their impacts can be observed in open circuit voltage, which is lower than the voltage predicted by the Nernst equation.

Error! Reference source not found. shows the polarization and power c urves of Cell 1 – 4, obtained under various RH conditions. Cell 1 and Cell 2 both show depth gradients within their multiple serpentine channels. Cell 2, which features ascending channels, demonstrated superior performance compared to Cell 1

in RH100% and RH60%. At RH30%, Cell 2 maintained a higher voltage up to a current density of 0.7 A/cm2, after which the voltage became similar to Cell 1. Still, Cell 2 achieved a higher maximum power density than Cell 1.

The cross-sectional area doubles as the channel depth changes from 0.4 mm to 0.8 mm, reducing the reactant gas velocity by half, allowing more time for the reactant gas diffuse toward the catalyst. However, the decrease in velocity also results in a reduced pressure drop, which is the driving force for removing liquid water droplets from the channel to the outlet. Consequently, an optimal channel depth exists for each fuel cell, balancing the depth to ensure sufficient contact time for reactants to reach the catalyst surface while preventing flooding or membrane dry-out. Since Cell 1 and Cell 2 have the same depth profile but differ in orientation, the performance difference can be attributed solely to the channel gradient. Our investigation showed that ascending channels outperformed descending channels. The maximum power density of Cell 2 in RH100%, 60%, and 30% was 1.4 %, 3.8%, and 1.6% higher than Cell 1, respectively. However, this result was unexpected as it contrasted with findings from the cathode design, where ascending metal foam flow fields outperformed descending flow fields due to efficient product water removal and enhanced oxygen diffusion towards the catalyst layer. However, in anode channels, the rapid hydrogen diffusion speed and high hydrogen concentration in the feed gas negate the advantages observed in cathode designs. Using ascending channels in the anode slows the membrane drying and promotes improved water management within the membrane.

The voltage of a cell can vary due to changes in operating conditions, inadequate or uneven distribution of reactants, and suboptimal water management within the MEA. Upon visually examining the polarization curves, the mass

transport resistance region does not emerge until reaching 1.6 A/cm^2 for cell 1 and cell 2 (**Figure 56** (a)). Given that operating conditions are controlled, it can be deduced that the voltage fluctuation below reaching 1.6 A/cm^2 is primarily a result of MEA hydration. Error! Reference source not found. represents the standard deviation of voltages of Cell 1 – 4 at selected current densities at three different RH conditions. The voltage standard deviation increases as feed gas humidification levels decrease, further supporting the notion that fluctuations below 1.6 A/cm2 are mainly due to MEA hydration. Cell 2 displays lower voltage standard deviations than cell 1, indicating that ascending channels with decreasing depths provide improved membrane hydration.

Cell 3 and 4 are fitted with metal foam flow fields in the anode. This design eliminates rib and channel structures, promoting faster gas transport to the catalyst, while the porous structure enhances water retention ability. As a result, Cell 3 and 4 achieved significantly higher voltage than Cell 1 and 2, which utilize serpentine channels. Cell 3 is designed with decreasing metal foam thickness toward the outlet, leading to decreased porosity and pore size, while Cell 4 features increasing metal foam thickness towards the outlet. These distinct metal foam designs further influence reactant transport and membrane hydration.

The polarization curves of both cells were almost identical at RH100% conditions, with Cell 4 marginally outperforming Cell 3 by 0.2% in maximum power density. The membranes are sufficiently humidified in RH100%, rendering the effect of gradient structure minimal. However, under RH60% and RH30% conditions, Cell 4 outperformed Cell 3, resulting in a maximum power density increase of 4.3% and 5.7%, respectively. Notably, at RH60% and 1.7 A/cm², the cell voltage between Cell 3 and 4 diverges. At high currents, electro-osmotic drag causes dehydration at the

anode-membrane interface, reducing proton conductivity. In this context, Cell 4 exhibits better membrane hydration, further evidenced by voltage standard deviations of less than 5 mV for all current densities and humidity conditions (**Figure 58Error! Reference source not found.**). Similar to the results for cells with gradient channels, gradient metal foam flow fields with increasing thickness and porosity performed better. Utilizing a porosity gradient metal foam in the anode yields improved cell performance under all RH conditions, outperforming cells with serpentine channels. The maximum power densities of Cell 4 at RH 100%, 60%, and 30% are 18.5%, 15.5%, and 18.5% higher than those of Cell 1, respectively. This result highlights the significant effect of the metal foam flow field on overall cell performance.

Cell 5 and 6 were fitted with cooling channels to enhance thermal management and further investigate the impact of metal foam gradient direction. Despite implementing changes in header design and metal foam coating, similar trends to Cell 3 and 4 were observed under fully humidified conditions, as shown in **Figure 58**. Cell 5 and 6 displayed nearly identical polarization curves, with a maximum power density of 1.012 W/cm2 and 1.013 W/cm2, respectively, displaying less than a 0.2% difference in power density. This suggests that the gradient orientation of the metal foam has no effect when reactant gases are fully humidified. As the gas humidity decreases, the performance of both cells begins to diverge. At RH60%, a minor difference of 0.6% in maximum power density is observed, and at RH30%, significant voltage differences are observed from the low current density region, resulting in a 12% difference in maximum power density. At a voltage of 0.6 V, Cell 5 produced a current density of 0.94 A/cm2, while Cell 6 merely produced 1.06 A/cm2. The maximum power density of 5 and 6 were 0.76 W/cm2 and 0.85

W/cm2. This result emphasizes the significant influence of the gradient direction of metal foam flow fields.
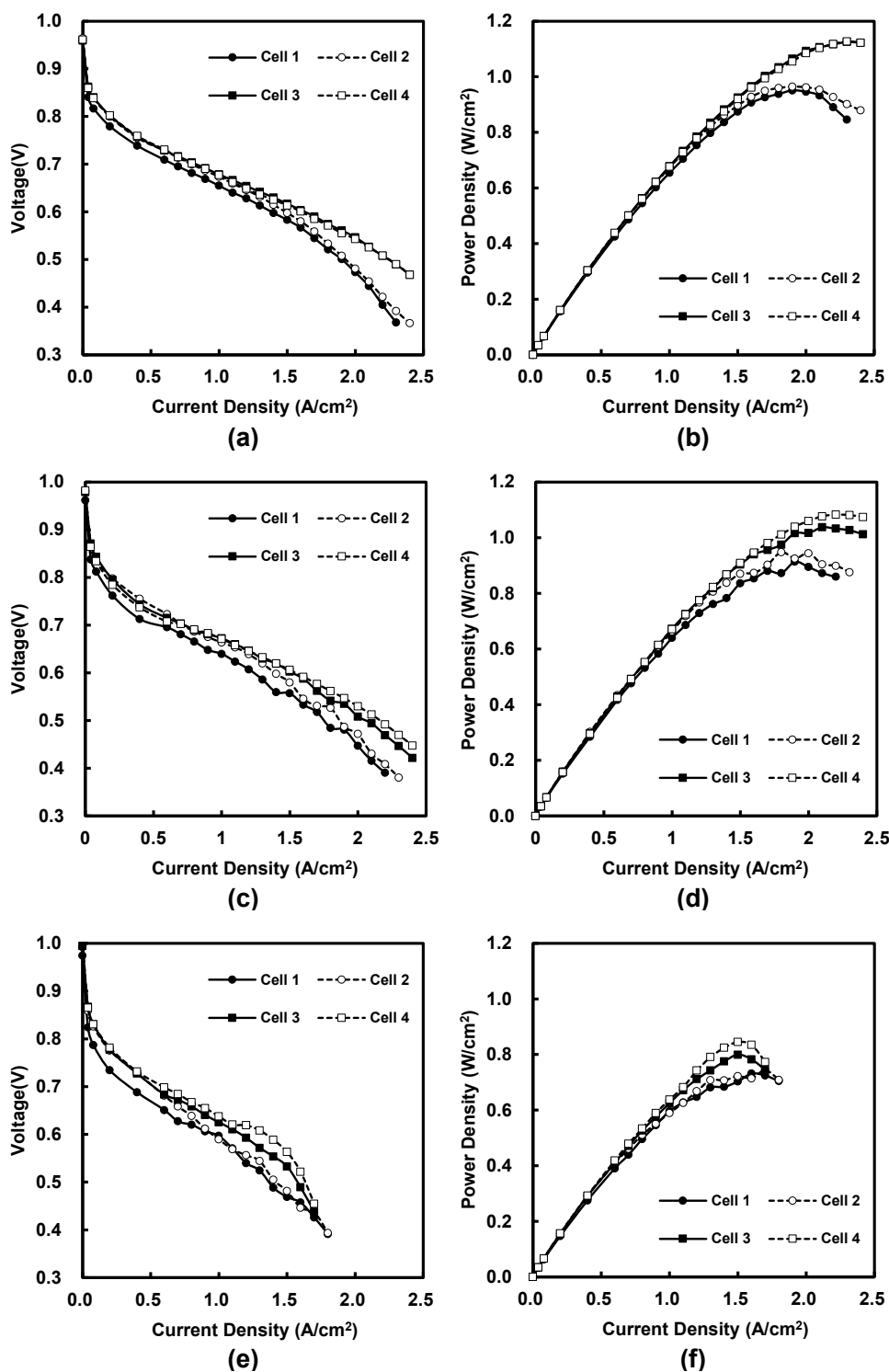
Figure 56 Polarization curves and power curves of four fuel cells for three different RH conditions: 100% (a, b), 60% (b, c), and 30% (e, f.)
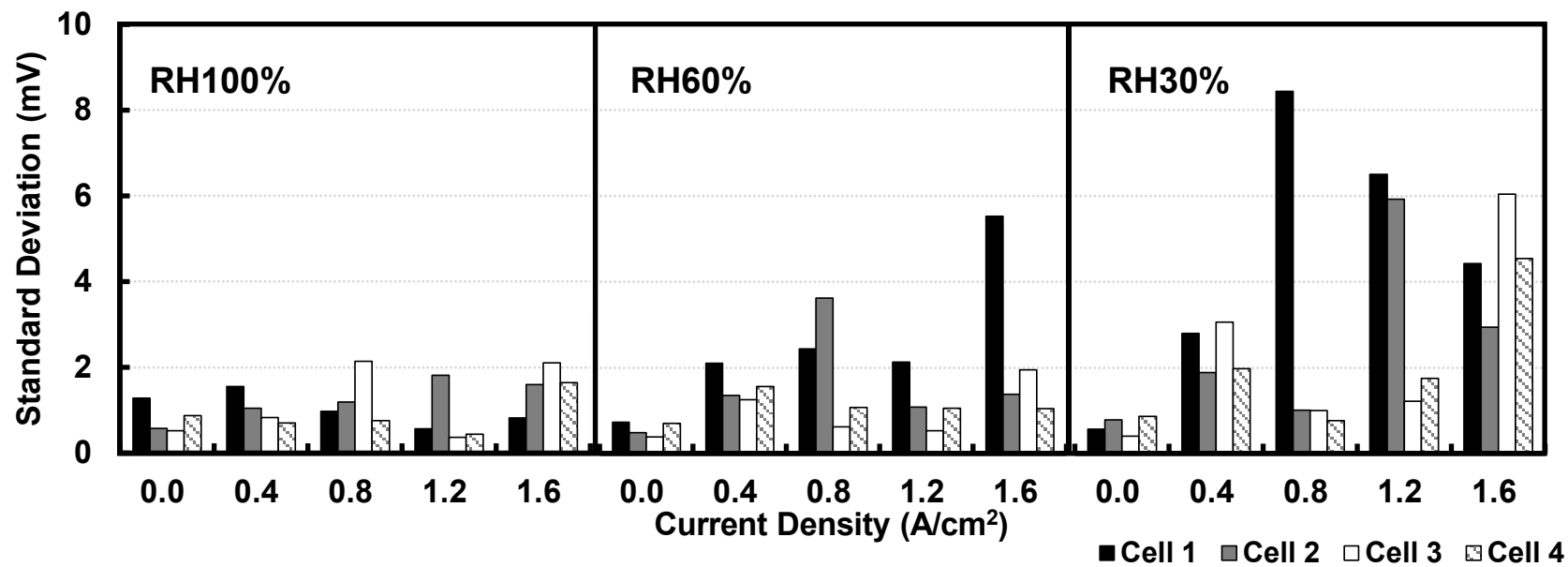
Figure 57 Voltage standard deviation comparison of Cell 1 – 4 under different humidity conditions at selected current densities
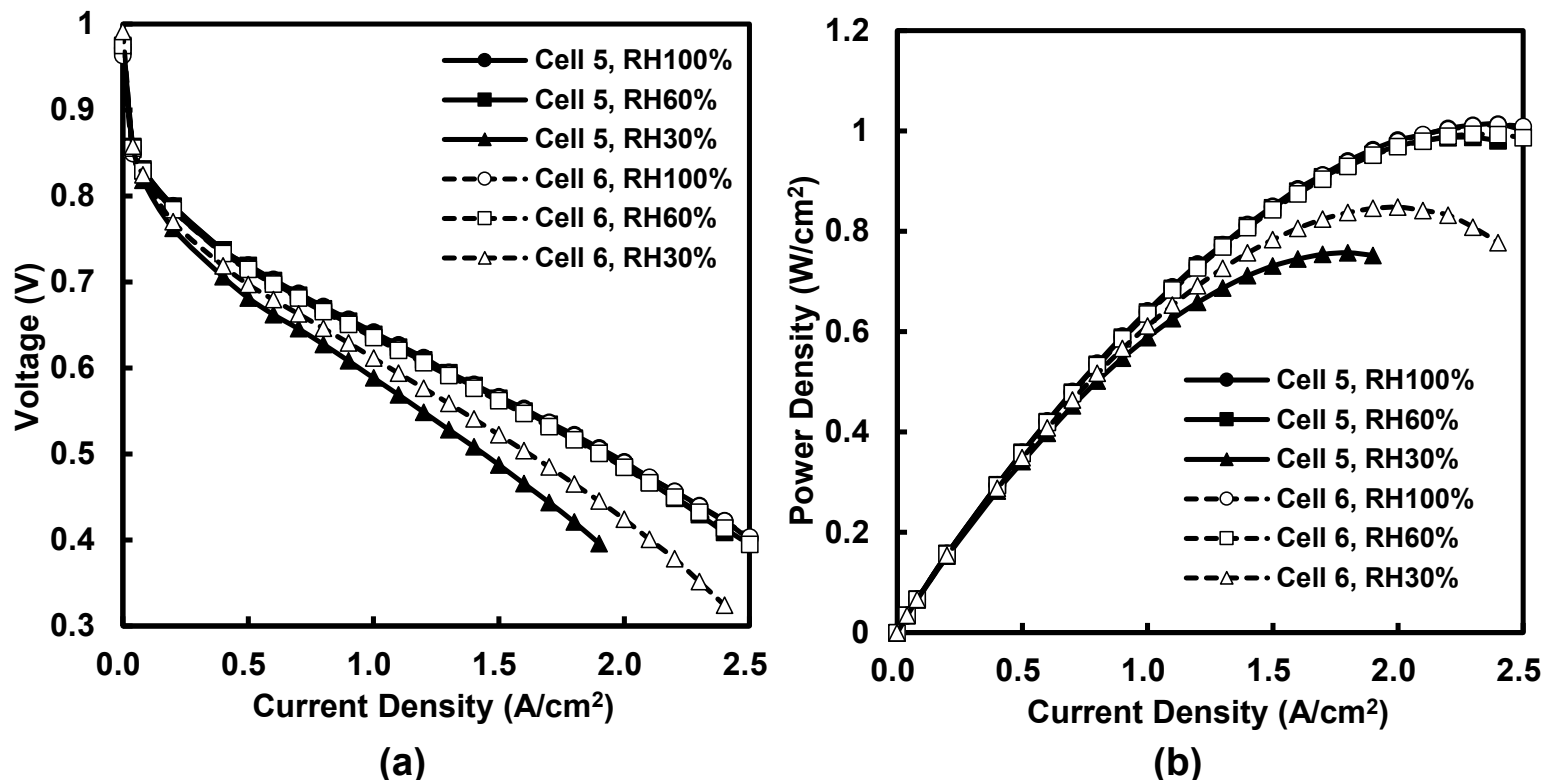
Figure 58 Effect of anode metal foam gradient direction on (a) polarization curves and (b) power curves under various humidity conditions, with Cell 5 representing the descending gradient and Cell 6 representing the ascending gradient

The Nyquist plots of Cell 5 and Cell 6 are shown in Figure 59, where the markers denote the actual experimental data, and the lines represent the fittings derived from the equivalent circuit. The experiment conducted at RH100% revealed that the HFR values for Cell 5 and 6 were 3.14 mΩ and 3.09 mΩ, respectively. These values reduced further to 2.97 mΩ and 2.93 mΩ at RH60% for both cells. A significant divergence between the cells was observed for RH30%. In this case, Cell 6 exhibited a high-frequency resistance(HFR) value of 3.27 mΩ, while Cell 5 displayed a substantially higher value of 3.78 mΩ. This pronounced difference of 0.51 mΩ corresponds to a 16% improvement in the ohmic resistance of Cell 6 compared to Cell 5, underling the superior membrane humidification performance of the gradient metal foam with increasing porosity and thickness design.

Surprisingly, our results indicated that the HFR values of both cells were slightly lower at RH60% compared to RH100%. The ionic conductivity of the membrane is intrinsically linked to its water uptake. Thus, higher humidity conditions are preferred to lower HFR values [63]. However, our observations challenged this common assumption, prompting us to consider two potential contributing factors: membrane swelling or pore blockage. Membrane swelling is proportional to its water content. In the fuel cell assembly, mechanical constraints obstruct the water uptake of the membrane, resulting in a 14% suppression in channel design, according to the findings of Lai et al. [64]. The membrane swelling, with its associated increase in thickness and compressive stress, may interact with the metal foam flow fields, potentially affecting ionic and electrical resistances. On another front, the possibility of pore blockage due to excessive water cannot be overlooked. Such blockages could force the protons to travel a more extended path from the membrane to the reaction site, thus increasing resistance. The specific cause behind

this anomalous behavior remains to be conclusively identified in future investigations.

The influence of relative humidity on the middle and low-frequency arcs, corresponding to the first and second arcs, is apparent in their decrease with increasing humidity. Beyond the impact of humidity on membrane conductivities, higher humidity substantially mitigates both charge transfer and mass transport losses. This improvement is attributed to the expanded reactive area at the three-phase interface, increased proton mobility, and superior oxygen transfer in the ionomer [30], [65], [66]. In the absence of flooding, the diameter of the low-frequency arc decreases, consistent with findings in other studies [65], [67]. Under flooding conditions, we expected a noticeable increase in the sizes of both arcs in the Nyquist plot–more predominantly at the low-frequency arc–and a sharp downward curvature in polarization curves. However, the polarization curves in **Figure 58** showed no downward curvature, suggesting the absence of flooding even at a high current density of 2.0 A/cm2 for both cell configurations.

Furthermore, the Warburg parameter Rzw, one of the equivalent circuit parameters in Table 19 and a key indicator of mass transfer resistance, was significantly lower than the charge transfer resistance Rct. This difference provides further evidence against flooding. As both the flow rate and water generation from the electrochemical reaction remain consistent, and given the constant design of the cathode flow fields, any performance variations among the cells can be attributed exclusively to the differential design of the anode flow field design.

The equivalent circuit fitting values from Table 19 revealed a 14% improvement in both Ro, and Rct, and a 20% enhancement in Rzw for Cell 6 compared to Cell 5. These results underscore the pivotal role of the anode flow field

design and the gradient direction of the flow fields in dictating the overall performance of fuel cells.
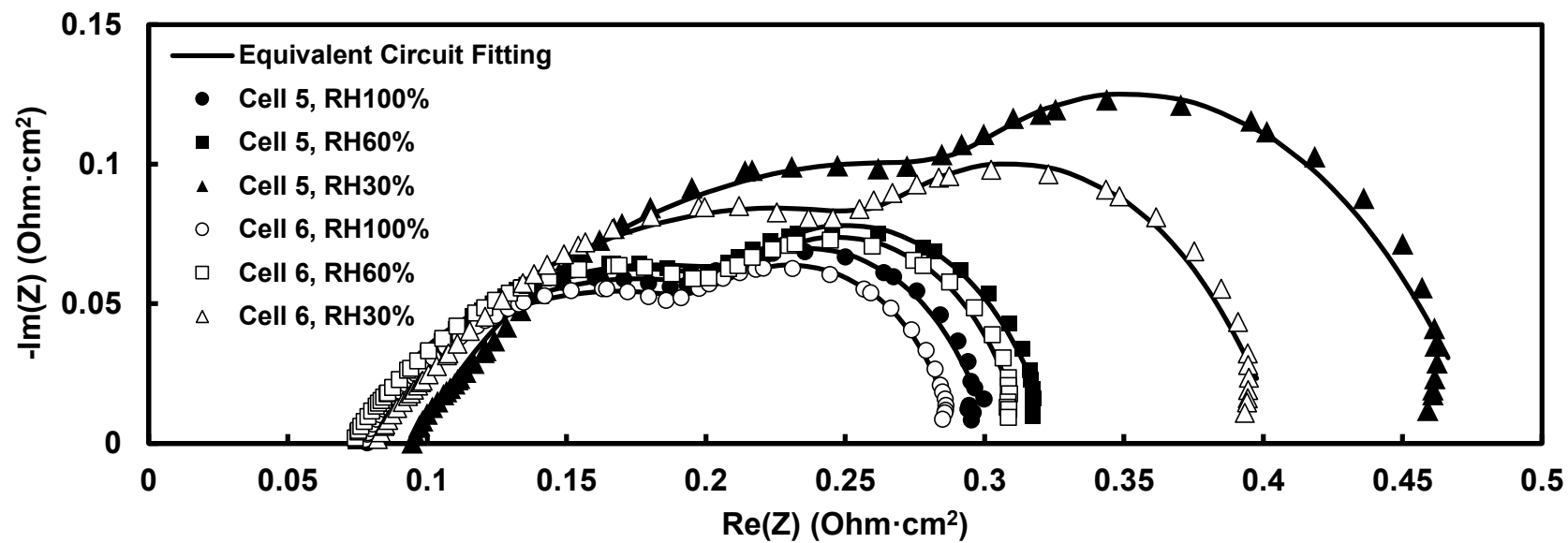
Figure 59 Comparison of gradient metal foam with different orientations under different humidity conditions: Nyquist plot at a current density of 2.0 A/cm^2 with individual equivalent circuit fitting lines.

Table 19 Parameters of fitted equivalent circuit for experimental data

Cell	RH	R_o (mΩ)	R_{ct} (mΩ)	T_{CPE}	P_{CPE}	R_{Zw} (mΩ)	T_{Zw}	P_{Zw}	$\chi2$ (-)
5	100%	3.11	6.80	5.18	0.73	2.28	0.06	0.67	7.44E-04
5	60%	2.98	7.42	4.88	0.72	2.67	0.06	0.67	7.28E-04
5	30%	3.86	11.73	4.01	0.72	3.66	0.06	0.69	2.02E-03
6	100%	3.10	6.22	4.65	0.73	2.33	0.06	0.65	5.08E-04
6	60%	2.97	7.20	4.45	0.73	2.49	0.06	0.67	7.34E-04
6	30%	3.33	10.07	4.21	0.71	2.94	0.06	0.69	1.41E-03

6.3.2. Effect of gradient metal foam flow field on cell durability

Polarization curves serve as a fundamental tool in evaluating the performance and the use of porosity gradient metal foam as anode flow fields has been experimentally proven to improve cell performance, but its effect on durability requires careful analysis. ASTs were carried out to assess the catalyst support corrosion. Polarization curves and EIS measurements at $2.0A/cm^2$ were obtained after 0, 5k, 10k, and 15k degradation cycles. Throughout the testing period, the absence of abrupt voltage drops in the open circuit voltage, typically indicative of membrane perforations or pinholes due to reactant gas crossover, suggests that the membrane integrity was maintained during the experiment. The degradation effects on Cell 5 – 7 were examined using polarization curves, Nyquist plots, and transient voltage response. The orientation of the gradient metal foam flow fields has a meaningful impact on the catalyst support degradation process, as shown in Figure 60(a, b).

Initially, Cell 5 showed a uniform performance deterioration in all current densities up to 10k cycles. However, after 10k cycles, the voltage declined near 0.8 A/cm^2, and 2.5 A/cm^2 was slightly higher than other ranges, and this trend became more severe after 20k cycles, resulting in a more curved voltage and current density line. This change in slope at high current density is consistent with the increased mass transport arc in the EIS results in Figure 61, indicating that carbon corrosion caused a decrease in liquid water removal ability, hence the oxygen transport ability. Similarly, Cell 6 showed a similar trend during the AST, with severe voltage deterioration near $0.8A/cm^2$. After 15k cycles, the voltage deterioration was worst among the three cells, indicating that Cell 6 was most susceptible to catalyst support degradation due to enhance water retention ability.

To determine the cell's ability to handle the load changes, the transient

responses of the voltage were measured after 5k and 15k degradation cycles. In Figure 62, the cell voltages for three cells at 1.2 A/cm2 were similar at 5k cycles. However, the voltage undershoots when the current density suddenly changed from 0.4 A/cm^2 to 1.2 A/cm^2 were around 60 mV for Cell 8, whereas Cell 5 and 7 showed voltage undershoots of 33 mV and 30 mV, respectively. This observation indicates that Cell 6 experiences faster performance degradation, primarily attributed to the carbon support loss within the MEA. Such degradation may not be readily identifiable by examining the polarization curve alone. EIS results indicated that Cell 6 has the most significant low-frequency arc, which supports its reduced ability to remove liquid water from carbon loss.

Meanwhile, Cell 7 showed a uniform performance deterioration across all current densities, and the voltage drop was nearly consistent with the degradation cycles, showing the cell's resilience against catalyst support degradation. The degradation cycle caused both high-frequency and low-frequency arcs in EIS to expand, indicating increased charge transport and mass transport resistance. The evolution of carbon dioxide from the carbon corrosion caused the loss of catalyst support, which in sequence caused the electrochemical surface area to decrease [68]. Impedance data were analyzed through equivalent circuits, and the resultant fitting parameters are presented in Table 20. It was observed that both charge transfer and mass transfer resistance escalated with the progression of degradation cycles, but the degree of this augmentation varied. Specifically, Rct for Cell 6 witnessed a 76% surge after 15k cycles, whereas Cell 7 exhibited a more moderate increase of 31%. A similar trend was observed for Rzw, where a 190% was recorded for Cell 6, contrasted with an 89% rise for Cell 7. Notably, there was a sharp rise in Rzw from the 10k to 15k degradation cycles, deviating from the trends of previous cycles. This

deviation could potentially serve as an early warning sign of impending electrode collapse. In the event of electrode collapse due to carbon corrosion, the thickness of the catalyst layer is reduced, resulting in a decrease in porosity [69], [70].

Contrarily, a marginal decrease in Ro was observed after 15k cycles for Cell 5–7. The underlying mechanisms behind this reduction could be attributed to the enhanced water retention due to decreased hydrophobicity in the catalyst layer and an increase in the porosity catalyst layer caused by the degradation cycles [71], [72].

Cell 6, with its anode flow fields' enhanced water retention abilities, showed a higher tendency to degrade. This observation emphasizes the importance of applying appropriate mitigation strategies during the start-up and shutdown stages to help extend the lifespan of the cell and maintain its efficiency.
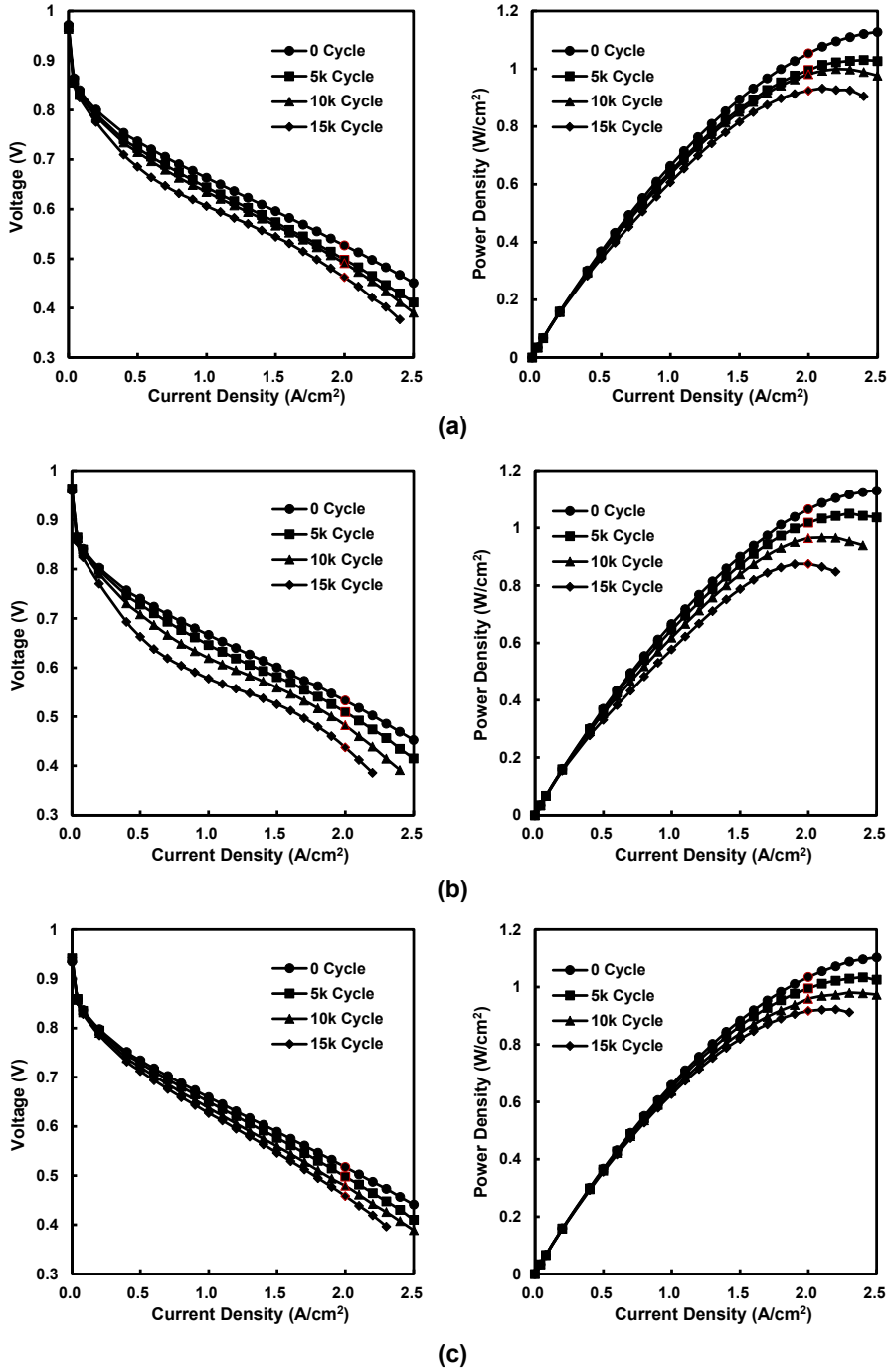
Figure 60 Impact of cyclic degradation on the performance of PEMFCs. The figure presents polarization and power curves for (a) Cell 5, (b) Cell 6, and (c) Cell 7 at 0, 5k, 10k, and 15k cycles. The degradation was induced through repeated triangular voltage sweeps from 1.0V to 1.5V at a rate of 500mV/s.
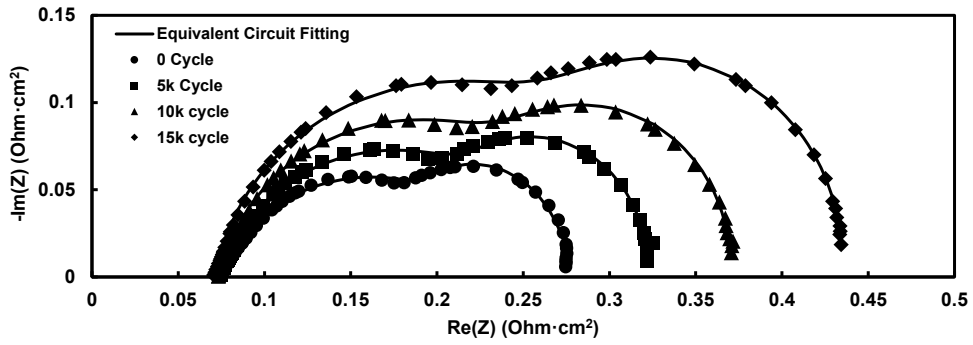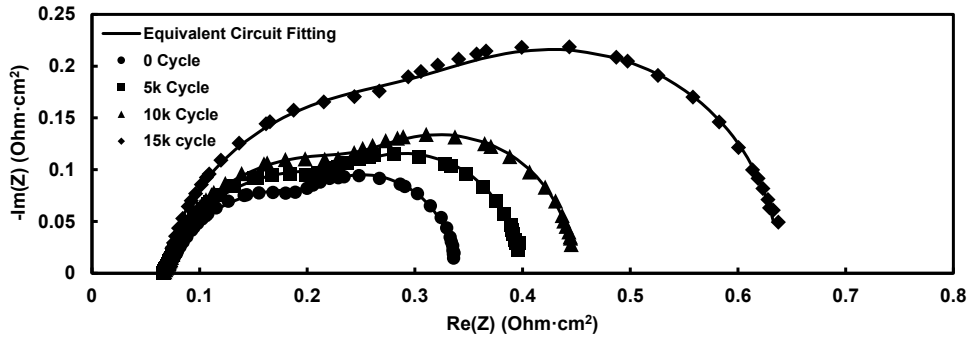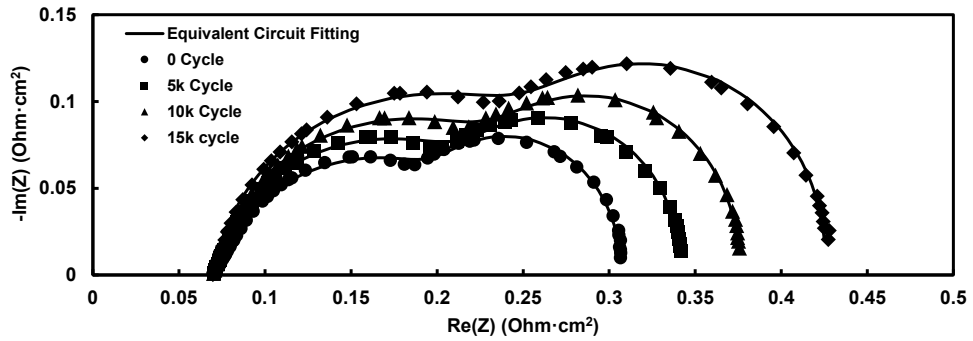
Figure 61 Impact of cyclic degradation on the impedance of the PEMFCs. The figure
presents Nyquist plots for (a) Cell 5, (b) Cell 6, and (c) Cell 7 at 0, 5k, 10k, and
15k cycles. The degradation was induced through repeated triangular voltage
sweeps from 1.0V to 1.5V at a rate of 500 mV/s.

Table 20 Parameters of equivalent circuit for Cell 5 to 7 at different degradation cycles

Cell	No. Cycles	R_o (mΩ)	R_{ct} (mΩ)	T_{CPE}	P_{CPE}	R_{zw} (mΩ)	T_{Zw}	P_{Zw}	χ^2 (-)
5	0	2.99	6.14	4.56	0.77	2.08	2.42	0.66	6.70E-04
5	5k	3.00	6.97	2.78	0.84	3.01	2.66	0.63	8.82E-04
5	10k	2.99	7.78	1.91	0.89	4.08	2.78	0.60	8.89E-04
5	15k	2.88	9.30	1.55	0.91	5.26	2.78	0.59	8.45E-04
6	0	2.76	7.67	3.59	0.83	3.22	2.51	0.64	9.70E-04
6	5k	2.72	8.63	2.51	0.86	4.59	2.85	0.60	9.96E-04
6	10k	2.76	9.35	1.92	0.89	5.80	3.02	0.58	1.05E-03
6	15k	2.73	13.51	1.49	0.92	9.35	3.11	0.56	1.14E-03
7	0	2.88	6.36	3.04	0.84	3.11	2.64	0.63	9.34E-04
7	5k	2.84	6.71	1.97	0.89	4.09	2.88	0.60	8.53E-04
7	10k	2.83	7.51	1.68	0.90	4.68	2.88	0.60	7.58E-04
7	15k	2.84	8.31	1.38	0.92	5.88	3.05	0.58	8.75E-04
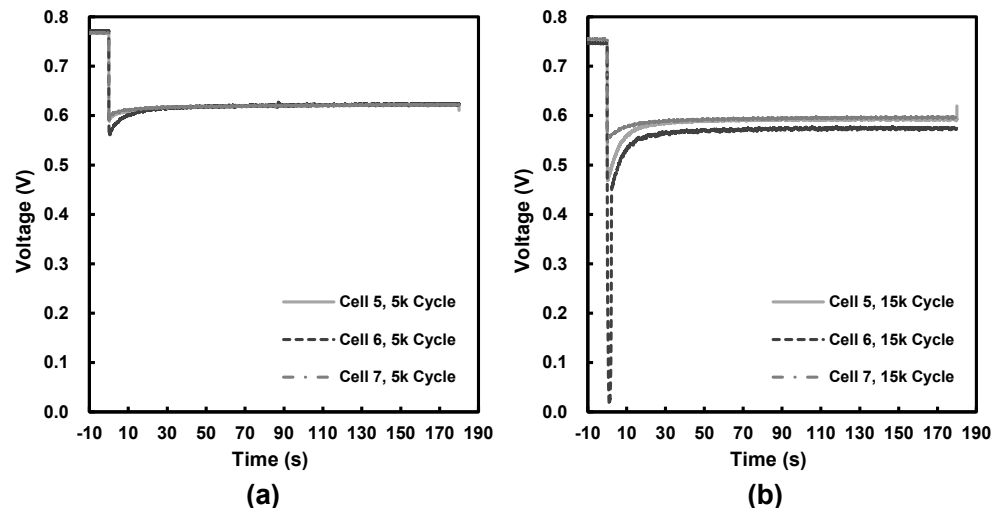
Figure 62 Voltage response of cell when current is changed from 0.4 A/cm^2 to 1.2 A/cm^2 at different degradation cycles: (a) 5k cycles, (b) 15k cycles

6.4. Summary

This study presents a comprehensive analysis of the impact of non-uniform anode flow fields on the performance of PEM fuel cells, addressing a gap in the existing literature, which primarily focuses on cathode flow fields. Our findings demonstrate that flow fields with an ascending gradient, characterized by an increase in depth from inlet to outlet, offer superior performance compared to those with a descending gradient. Moreover, metal foams with gradient designs outperform gradient channels due to the elimination of ribs, enabling faster gas transport, and the inherent porous structure of metal foams enhances water retention ability.

Both channels and metal foams show notable enhancements from gradient design, with maximum power density increasing by up to 3.8% and 5.7%, respectively. This improvement is attributed to the better membrane hydration offered by the ascending gradient design. Importantly, under lower humidity conditions, the benefits of an ascending design become even more pronounced, as ascending gradient metal foams at RH30% show a significant 12.0% increase in maximum power density compared to a descending gradient. However, it is essential to acknowledge that this enhanced water retention ability could increase susceptibility to degradation, as observed through accelerated stress tests.

In conclusion, our study sheds light on the substantial impact of anode flow effects on PEM fuel cell performance. The importance of maintaining optimal membrane hydration increases significantly with the ability of the fuel cell to operate at higher currents, as the electro-osmotic drag leads to the membrane drying at the anode side. Therefore, the implications are substantial when implementing a PEM fuel cell with an oxygen concentrator. The introduction of the ascending gradient

design provides a promising solution to enhance fuel cell performance by improving water retention and membrane hydration.

Chapter 7. Conclusions

This comprehensive study focused on enhancing the performance of a PEM fuel cell and an oxygen concentrator, which hold immense potential in stationary power generation applications.

Chapter 1 laid the foundation, emphasizing the importance of oxygen concentration at the catalyst surface and discussing strategies to increase this concentration. The novel approach was to increase the feed oxygen concentration rather than reduce oxygen transport resistance.

In Chapter 2, the effects of oxygen concentration on PEM fuel cells were extensively studied. Oxygen enrichment led to significant enhancements in the fuel cell's performance.

Chapter 3 expanded on this work by building and evaluating a small-scale oxygen concentrator. The study focused on the importance of adsorption timing, showing that optimal performance is achieved at a specific adsorption duration. Deviations from this period could lead to performance deterioration. The chapter concluded that balancing oxygen concentration and product flow rate is crucial for achieving optimal power output in a PEM fuel cell.

In Chapter 4, mathematical models for the oxygen concentrator and the PEM fuel cell were developed. The models demonstrated the impacts of varying operating parameters on the system's efficiency and effectiveness. The findings indicated the possibility of optimizing the oxygen concentrator, and thus the entire system, by adjusting these parameters.

Chapter 5 combined the oxygen concentrator with the PEM fuel cell, exploring two distinct linking processes. The results indicated a need for a mass flow

controller to provide stable power output. The chapter concluded that the developed oxygen concentrator could yield a 3W increase in PEM fuel cell performance, excluding specific energy consumptions.

Chapter 6 delved into the influence of the anode flow field design on PEM performance and degradation. Results revealed that channels with an increasing depth outperform those with decreasing depth. These findings emphasized the importance of good water management and slow membrane drying.

In conclusion, this research showcases the potential for integrating a PSA system-based oxygen concentrator to enhance the performance of a PEM fuel cell system. The study encourages future research to consider oxygen purity and pressure as variables rather than fixed parameters and explore their impact under transient load conditions. It also suggests investigating the behavior of PEMFCs under fluctuating conditions, which is crucial for designing more effective oxygen concentrators.

References

[1]   UNDP, "Peoples' Climate Vote," *United Nations Dev. Program.*, vol. 1, pp. 1–68, 2021, [Online]. Available: https://www.undp.org/publications/peoples-climate-vote.

[2]   International Energy Agency (IEA), "Global EV Outlook 2022 - Securing supplies for an electric future," 2022.

[3]   "Public-private partnership as a tool for EV infrastructure - American City and County." https://www.americancityandcounty.com/2022/03/04/public-private-partnership-as-a-tool-for-ev-infrastructure/ (accessed Apr. 27, 2023).

[4]   B. G. Pollet, S. S. Kocha, and I. Staffell, "Current status of automotive fuel cells for sustainable transport," *Curr. Opin. Electrochem.*, vol. 16, pp. 90–95, Aug. 2019, doi: 10.1016/J.COELEC.2019.04.021.

[5]   M. K. Debe, "Electrocatalyst approaches and challenges for automotive fuel cells," *Nat. 2012 4867401*, vol. 486, no. 7401, pp. 43–51, Jun. 2012, doi: 10.1038/nature11115.

[6]   L. Chong *et al.*, "Ultralow-loading platinum-cobalt fuel cell catalysts derived from imidazolate frameworks," *Science (80-.).*, vol. 362, no. 6420, pp. 1276–1281, 2018, doi: 10.1126/science.aau0630.

[7]   C. C. Chan, "The state of the art of electric, hybrid, and fuel cell vehicles," *Proc. IEEE*, vol. 95, no. 4, pp. 704–718, 2007, doi: 10.1109/JPROC.2007.892489.

[8]   R. P. O'Hayre, S.-W. Cha, C. W. G., and P. F. B., "Fuel Cell Fundamentals,

2nd Ed.," *John Wiley Sons*, 2009.

[9]   R. Kumar and K. A. Subramanian, "Enhancement of efficiency and power output of hydrogen fuelled proton exchange membrane (PEM) fuel cell using oxygen enriched air," *Int. J. Hydrogen Energy*, vol. 48, no. 15, pp. 6067–6075, Feb. 2023, doi: 10.1016/J.IJHYDENE.2022.11.141.

[10]   C. W. Skarstrom and O.-O. I. Attorney, "Method and apparatus for fractionating gaseous mixtures by adsorption," Feb. 1958.

[11]   D. Ferreira, M. Boaventura, P. Bárcia, R. D. Whitley, and A. Mendes, "Two-Stage Vacuum Pressure Swing Adsorption Using AgLiLSX Zeolite for Producing 99.5+% Oxygen from Air," *Ind. Eng. Chem. Res.*, vol. 55, no. 3, pp. 722–736, Jan. 2016, doi: 10.1021/ACS.IECR.5B03535/ASSET/IMAGES/IE-2015-03535K_M046.GIF.

[12]   J. G. Jee, S. J. Lee, H. M. Moon, and C. H. Lee, "Adsorption dynamics of air on zeolite 13X and CMS beds for separation and purification," *Adsorption*, vol. 11, no. 1 SUPPL., pp. 415–420, Jul. 2005, doi: 10.1007/S10450-005-5960-1/METRICS.

[13]   D. Ferreira, P. Bárcia, R. D. Whitley, and A. Mendes, "Single-Stage Vacuum Pressure Swing Adsorption for Producing High-Purity Oxygen from Air," *Ind. Eng. Chem. Res.*, vol. 54, no. 39, pp. 9591–9604, Oct. 2015, doi: 10.1021/ACS.IECR.5B02151/ASSET/IMAGES/IE-2015-02151W_M034.GIF.

[14]   J. C. Santos, P. Cruz, T. Regala, F. D. Magalhães, and A. Mendes, "High-Purity Oxygen Production by Pressure Swing Adsorption," 2007, doi:

10.1021/ie060400g.

[15]   A. F. Al-Shawabkeh, N. Al-Najdawi, and A. N. Olimat, "High purity
       oxygen production by pressure vacuum swing adsorption using natural
       zeolite," *Results Eng.*, vol. 18, no. January, p. 101119, 2023, doi:
       10.1016/j.rineng.2023.101119.

[16]   J. Sebastian and R. V. Jasra, "Sorption of nitrogen, oxygen, and argon in
       silver-exchanged zeolites," *Ind. Eng. Chem. Res.*, vol. 44, no. 21, pp. 8014–
       8024, Oct. 2005, doi:
       10.1021/IE050442P/ASSET/IMAGES/LARGE/IE050442PF00008.JPEG.

[17]   D. Shen, M. Bülow, S. R. Jale, F. R. Fitch, and A. F. Ojo,
       "Thermodynamics of nitrogen and oxygen sorption on zeolites LiLSX and
       CaA," *Microporous Mesoporous Mater.*, vol. 48, no. 1–3, pp. 211–217,
       2001, doi: 10.1016/S1387-1811(01)00355-9.

[18]   Y. Fu *et al.*, "Thermodynamic analysis of molecular simulations of N 2 and
       O 2 adsorption on zeolites under plateau special conditions," *Appl. Surf.
       Sci.*, vol. 480, no. February, pp. 868–875, 2019, doi:
       10.1016/j.apsusc.2019.03.011.

[19]   S. J. Chen, M. Zhu, Y. Fu, Y. X. Huang, Z. C. Tao, and W. L. Li, "Using
       13X, LiX, and LiPdAgX zeolites for CO 2 capture from post-combustion
       flue gas," 2017, doi: 10.1016/j.apenergy.2017.01.031.

[20]   A. Moran and O. Talu, "Role of Pressure Drop on Rapid Pressure Swing
       Adsorption Performance," 2017, doi: 10.1021/acs.iecr.7b00577.

[21]   K. A. Burke, "Fuel cells for space science applications," 2003, doi:
       10.2514/6.2003-5938.

[22] A. B. LaConti and L. Swette, "Special applications using PEM-technology," *Handb. Fuel Cells*, Dec. 2010, doi: 10.1002/9780470974001.F303062.

[23] B. Nitin, P. Sandilya, and G. Chakraborty, "Revisiting the dewar design for liquid oxygen storage in fuel cell energy systems," *Int. Commun. Heat Mass Transf.*, vol. 134, p. 105975, May 2022, doi: 10.1016/J.ICHEATMASSTRANSFER.2022.105975.

[24] B. Sezgin, Y. Devrim, T. Ozturk, and I. Eroglu, "Hydrogen energy systems for underwater applications," *Int. J. Hydrogen Energy*, vol. 47, no. 45, pp. 19780–19796, May 2022, doi: 10.1016/J.IJHYDENE.2022.01.192.

[25] F. Mueller, J. Brouwer, S. Kang, H. S. Kim, and K. Min, "Quasi-three dimensional dynamic model of a proton exchange membrane fuel cell for system and controls development," *J. Power Sources*, vol. 163, no. 2, pp. 814–829, Jan. 2007, doi: 10.1016/J.JPOWSOUR.2006.09.089.

[26] N. Wagner, "Electrochemical Impedance Spectroscopy," in *PEM Fuel Cell Diagnostic Tools*, CRC Press, 2011, pp. 37–70.

[27] J.-B. Jorcin, M. E. Orazem, N. Pébère, and B. Tribollet, "CPE analysis by local electrochemical impedance spectroscopy," *Electrochim. Acta*, vol. 51, pp. 1473–1479, 2006, doi: 10.1016/j.electacta.2005.02.128.

[28] E. Barsoukov and J. R. Macdonald, *Impedance Spectroscopy: Theory, Experiment, and Applications*. 2005.

[29] I. Pivac and F. Barbir, "Inductive phenomena at low frequencies in impedance spectra of proton exchange membrane fuel cells – A review," *J. Power Sources*, vol. 326, pp. 112–119, Sep. 2016, doi:

10.1016/J.JPOWSOUR.2016.06.119.

[30] L. Zhao, H. Dai, F. Pei, P. Ming, X. Wei, and J. Zhou, "A Comparative Study of Equivalent Circuit Models for Electro-Chemical Impedance Spectroscopy Analysis of Proton Exchange Membrane Fuel Cells," *Energies*, vol. 15, no. 1, 2022, doi: 10.3390/en15010386.

[31] J. Wu, X. Z. Yuan, H. Wang, M. Blanco, J. J. Martin, and J. Zhang, "Diagnostic tools in PEM fuel cell research: Part I Electrochemical techniques," *International Journal of Hydrogen Energy*, vol. 33, no. 6. 2008, doi: 10.1016/j.ijhydene.2008.01.013.

[32] A. R. Smith and J. Klosek, "A review of air separation technologies and their integration with energy conversion processes," *Fuel Process. Technol.*, vol. 70, no. 2, pp. 115–134, May 2001, doi: 10.1016/S0378-3820(01)00131-X.

[33] J. Park, "Study on the effects of structural characteristics of gas diffusion layer on water management and cell performance with PEM fuel cell model," Seoul National University, 2015.

[34] S. Kang, "Quasi-three dimensional dynamic modeling of a proton exchange membrane fuel cell with consideration of two-phase water transport through a gas diffusion layer," *Energy*, vol. 90, pp. 1388–1400, Oct. 2015, doi: 10.1016/J.ENERGY.2015.06.076.

[35] L. Xing, X. Liu, T. Alaje, R. Kumar, M. Mamlouk, and K. Scott, "A two-phase flow and non-isothermal agglomerate model for a proton exchange membrane (PEM) fuel cell," *Energy*, vol. 73, pp. 618–634, Aug. 2014, doi: 10.1016/J.ENERGY.2014.06.065.

[36]   S. Kang, "Quasi-three dimensional dynamic modeling of a proton exchange membrane fuel cell with consideration of two-phase water transport through a gas diffusion layer," *Energy*, vol. 90, 2015, doi: 10.1016/j.energy.2015.06.076.

[37]   E. N. Fuller, P. D. Schettler, and J. C. Giddings, "A new method for prediction of binary gas-phase diffusion coefficients," *Ind. Eng. Chem.*, vol. 58, no. 5, 1966, doi: 10.1021/ie50677a007.

[38]   C. Spiegel, *PEM Fuel Cell Modeling and Simulation Using Matlab*. 2008.

[39]   M. M. Mench, *Fuel Cell Engines*. 2008.

[40]   C. Y. Wang and P. Cheng, "A multiphase mixture model for multiphase, multicomponent transport in capillary porous media - I. Model development," *Int. J. Heat Mass Transf.*, vol. 39, no. 17, pp. 3607–3618, 1996, doi: 10.1016/0017-9310(96)00036-1.

[41]   M. Kaviany, "Principles of Heat Transfer in Porous Media," *Mech. Eng. Ser.*, vol. 53, no. 9, 1995.

[42]   N. Jeong, D. H. Choi, and C.-L. Lin, "Prediction of Darcy–Forchheimer drag for micro-porous structures of complex geometry using the lattice Boltzmann method," *J. Micromechanics Microengineering*, vol. 16, pp. 2240–2250, 2006, doi: 10.1088/0960-1317/16/10/042.

[43]   X. Ye and C.-Y. Wang, "Measurement of Water Transport Properties Through Membrane-Electrode Assemblies," *J. Electrochem. Soc.*, vol. 154, no. 7, 2007, doi: 10.1149/1.2737379.

[44]   D. R. Baker, D. A. Caulk, K. C. Neyerlin, and M. W. Murphy, "Measurement of Oxygen Transport Resistance in PEM Fuel Cells by

Limiting Current Methods," *J. Electrochem. Soc.*, vol. 156, no. 9, p. B991, 2009, doi: 10.1149/1.3152226.

[45]   C. Marr and X. Li, "Composition and performance modelling of catalyst layer in a proton exchange membrane fuel cell," *J. Power Sources*, vol. 77, no. 1, 1999, doi: 10.1016/S0378-7753(98)00161-X.

[46]   J. Zhang, Y. Tang, C. Song, J. Zhang, and H. Wang, "PEM fuel cell open circuit voltage (OCV) in the temperature range of 23 °C to 120 °C," *J. Power Sources*, vol. 163, no. 1 SPEC. ISS., pp. 532–537, 2006, doi: 10.1016/j.jpowsour.2006.09.026.

[47]   S. Um, C.-Y. Wang, and K. S. Chen, "Computational Fluid Dynamics Modeling of Proton Exchange Membrane Fuel Cells," *J. Electrochem. Soc.*, vol. 147, no. 12, 2000, doi: 10.1149/1.1394090.

[48]   A. Laurent, E. Lack, T. Gamse, and R. Marr, "High Pressure Process Technology: Fundamentals and Applications," *Ind. Chem. Libr.*, vol. 9, 2001.

[49]   F. M. White, *Fluid Mechanics (8th ed.)*, vol. 11, no. 3. 2017.

[50]   Z. Ding, Z. Han, Q. Fu, Y. Shen, C. Tian, and D. Zhang, "Optimization and analysis of the VPSA process for industrial-scale oxygen production," *Adsorption*, vol. 1, pp. 499–516, 2018, doi: 10.1007/s10450-018-9956-z.

[51]   C. Yin, W. Sun, H. Yang, and D. Zhang, "Optimization of three-bed VPSA system for biogas upgrading," *Chem. Eng. Sci.*, vol. 135, pp. 100–108, 2015, doi: 10.1016/j.ces.2015.06.022.

[52]   H. R. Ashorynejad, K. Javaherdeh, and H. E. A. Van den Akker, "The effect of pulsating pressure on the performance of a PEM fuel cell with a

wavy cathode surface," *Int. J. Hydrogen Energy*, vol. 41, no. 32, pp. 14239–14251, Aug. 2016, doi: 10.1016/J.IJHYDENE.2016.05.291.

[53] S. H. Han, N. H. Choi, and Y. D. Choi, "Simulation and experimental analysis on the performance of PEM fuel cell by the wave-like surface design at the cathode channel," *Int. J. Hydrogen Energy*, vol. 39, no. 6, pp. 2628–2638, Feb. 2014, doi: 10.1016/J.IJHYDENE.2013.08.063.

[54] J. C. Santos, A. F. Portugal, F. D. Magalhães, and A. Mendes, "Optimization of medical PSA units for oxygen production," *Ind. Eng. Chem. Res.*, vol. 45, no. 3, pp. 1085–1096, 2006, doi: 10.1021/ie0504809.

[55] Y. A. Cengel and M. A. Boles, *Thermodynamics: an Engineering Approach 8th Edition*. 2015.

[56] J. M. Campbell, "Gas Conditioning and Processing. Volume 2: The equipment modules," *Gas Conditioning and Processing Vol. 2*. 1992.

[57] F. E. Epiepang, R. T. Yang, X. Yang, J. Li, and Y. Liu, "Mixed-cation LiCa-LSX zeolite with minimum lithium for air separation," *AIChE J.*, vol. 64, no. 2, pp. 406–415, Feb. 2018, doi: 10.1002/AIC.16032.

[58] Y. Il Lee and M. S. Kim, "Effect of gradient anode flow field designs on polymer electrolyte membrane fuel cells," *Int. J. Hydrogen Energy*, no. xxxx, 2023, doi: 10.1016/j.ijhydene.2023.06.290.

[59] A. Fly *et al.*, "X-ray tomography and modelling study on the mechanical behaviour and performance of metal foam flow-fields for polymer electrolyte fuel cells," *Int. J. Hydrogen Energy*, vol. 44, no. 14, 2019, doi: 10.1016/j.ijhydene.2019.01.206.

[60] D. G. Kang, D. K. Lee, J. M. Choi, D. K. Shin, and M. S. Kim, "Study on

the metal foam flow field with porosity gradient in the polymer electrolyte membrane fuel cell," *Renew. Energy*, vol. 156, pp. 931–941, Aug. 2020, doi: 10.1016/J.RENENE.2020.04.142.

[61]   "Fuel Cell Technical Team Roadmap," Jun. 2013. doi: 10.2172/1220127.

[62]   S. T. Revankar and P. Majumdar, *Fuel cells: Principles, design, and analysis*. 2016.

[63]   J. Zhang *et al.*, "PEM fuel cell relative humidity (RH) and its effect on performance at high temperatures," *Electrochim. Acta*, vol. 53, no. 16, pp. 5315–5321, Jun. 2008, doi: 10.1016/J.ELECTACTA.2008.02.074.

[64]   Y. H. Lai, G. W. Fly, and S. Clapham, "In-situ membrane hydration measurement of proton exchange membrane fuel cells," *J. Power Sources*, vol. 274, 2015, doi: 10.1016/j.jpowsour.2014.09.089.

[65]   H. Yuan, H. Dai, P. Ming, L. Zhao, W. Tang, and X. Wei, "Understanding dynamic behavior of proton exchange membrane fuel cell in the view of internal dynamics based on impedance," *Chem. Eng. J.*, vol. 431, 2022, doi: 10.1016/j.cej.2021.134035.

[66]   D. Malevich, E. Halliop, B. Peppley, J. Pharoah, and K. Karan, "Effect of Relative Humidity on Electrochemical Active Area and Impedance Response of PEM Fuel Cell," *ECS Trans.*, vol. 16, no. 2, 2008, doi: 10.1149/1.2982017.

[67]   T. Ma, W. Lin, Z. Zhang, J. Kang, and Y. Yang, "Research on electrochemical impedance spectroscope behavior of fuel cell stack under different reactant relative humidity," *Int. J. Hydrogen Energy*, vol. 46, no. 33, pp. 17388–17396, May 2021, doi: 10.1016/J.IJHYDENE.2021.02.156.

[68] Y. Li *et al.*, "Carbon corrosion behaviors and the mechanical properties of proton exchange membrane fuel cell cathode catalyst layer," *Int. J. Hydrogen Energy*, vol. 45, no. 43, pp. 23519–23525, 2020, doi: 10.1016/j.ijhydene.2020.06.170.

[69] N. Macauley *et al.*, "Carbon Corrosion in PEM Fuel Cells and the Development of Accelerated Stress Tests," *J. Electrochem. Soc.*, vol. 165, no. 6, 2018, doi: 10.1149/2.0061806jes.

[70] R. T. White, A. Wu, M. Najm, F. P. Orfino, M. Dutta, and E. Kjeang, "4D in situ visualization of electrode morphology changes during accelerated degradation in fuel cells by X-ray computed tomography," *J. Power Sources*, vol. 350, 2017, doi: 10.1016/j.jpowsour.2017.03.058.

[71] L. Castanheira *et al.*, "Carbon corrosion in proton-exchange membrane fuel cells: From model experiments to real-life operation in membrane electrode assemblies," *ACS Catal.*, vol. 4, no. 7, 2014, doi: 10.1021/cs500449q.

[72] Q. Meyer, Y. Zeng, and C. Zhao, "Electrochemical impedance spectroscopy of catalyst and carbon degradations in proton exchange membrane fuel cells," *J. Power Sources*, vol. 437, 2019, doi: 10.1016/j.jpowsour.2019.226922.

Abstract in Korean

본 연구에서는 압력 스윙 흡착(PSA) 기술을 이용한 산소발생기와 구배형 음극 분리판을 통하여 고분자전해질막(PEM) 연료전지의 성능 향상에 대해 조사하였다. 본 연구는 양극 촉매에서의 PEM 연료전지의 낮은 효율과 음극 분리판 최적 설계와 관련된 과제를 해결하고자 한다.

첫 번째로 PSA 산소 분리를 이용한 프로토타입 산소발생기를 개발하고 평가하였다. 또한, 병렬 채널형 분리판을 갖는 기존 PEM 연료전지의 성능을 다양한 산소 농도 하에서 측정하였다.. 결과는 최적화 없이 PSA 시스템이 1.62 SLM의 유량으로 40%의 산소 순도를 제공할 수 있음을 확인하였다. 연료전지의 경우, 공급 산소농도를 기본 공기인 21%에서 2배로 증가시키면 최대 셀 성능이 12와트 증가하고 성능의 큰 손실 없이 양극 유량을 감소시킬 수 있었다. 테스트를 통해 공급 가스의 산소 농도 증가로 인한 연료 전지의 성능 향상이 산소발생기의 공기 펌프가 소비하는 전력을 약간 초과하는 것으로 확인하여 산소발생기를 활용한 연료전지 시스템의 가능성을 확인하였다.

두 번째로는 Matlab® 플랫폼을 활용하여 산소발생기와 PEM 연료 전지에 대한 통합 수학 모델을 개발한다. 산소발생기는 압력 스윙 흡착 사이클을 시뮬레이션하여 다양한 작동 조건에서 산소 순도, 회수 등의 성능을 예측할 수 있었다. PEM 연료전지 모델의 경우 기체 조성에

민감하게 반응하도록 설계되어 향후 최적화 및 작동 목적을 위해 산소 농축기의 출력과 효과적인 결합이 가능하도록 설계되었다.

마지막으로는 음극 구배 유동장이 PEM 연료전지 성능에 미치는 영향을 분석하여 음극 설계에 대한 잠재적 편익을 파악하였다. 채널을 따라 불균일한 가스 구성이 미치는 영향과 이에 따른 분리막의 수화에 초점을 맞추고, 셀 성능을 더욱 향상시키기 위해 경사도 흐름 채널 또는 금속 폼과 같은 경사도 설계 접근법을 활용하였다.

본 연구의 결과를 통해 PSA 산소발생기를 PEM 연료전지와 결합하면 유지보수 및 자본 비용 증가에도 불구하고 순 전력 이득을 얻을 수 있는 잠재력이 있음을 보여준다. 또한, 산소농축으로 인해 양극 과전압이 감소함에 따라 분리막 및 음극의 과전압과 같은 다른 저항 요인을 집중할 수 있어 경사 구조 유동장이 연료전지 성능에 미치는 영향을 발견할 수 있었다.

결론적으로 연구는 산소발생기를 활용한 공급기체의 산소농도증가를 통한 성능향상 및 구배설계가 적용된 음극 유로설계를 통한 성능향상에 기여하였다. 연구 결과는 다양한 응용 분야에서 보다 효율적이고 비용 효율적인 연료 전지 시스템 개발에 중요한 영향을 미칠 것으로 생각된다.

주요어: 고분자전해질막 연료전지, 압력변동흡착, 산소발생기, 농축산소,
**   기울기 설계 유로**
학 번: 2019-37511